

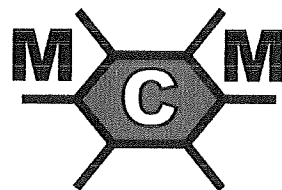
# Reconstruction of Three-Dimensional Microstructures from Non-Destructive 3DXRD Microscopy Measurements

*Development of a computational methodology*

M.Sc. Thesis

A.C.P. van der Zijden

Section of Microstructural Control in Metals  
Department of Materials Science and Engineering  
Faculty of Mechanical, Maritime and Materials Engineering  
Delft University of Technology



## Preface

This thesis reflects the results of my graduate research, performed at the faculty of Mechanical, Maritime and Materials Engineering at Delft University of Technology. The project was carried out as the final module of the Master of Science curriculum of the Materials Science and Engineering program, and took place within the section of Microstructural Control in Metals. It focused on the development of a computational framework for the reconstruction of a three-dimensional polycrystalline microstructure using data obtained by three-dimensional x-ray diffraction microscopy. The examination committee consisted of the following persons:

- Prof.dr.ir. L.A.I. Kestens (chairman)
- Dr.ir. S.E. Offerman (daily supervisor)
- Dr.ir. J. Sietsma
- Dr. A. Böttger (external delegate)
- Dr.ir. N.H. van Dijk (external delegate)

I would like to express my gratitude towards my examination committee, most notably my daily supervisor Erik Offerman. I have experienced our working together as highly enjoyable, and his continuous feedback as vital to the realization of this thesis. Furthermore, I would like to acknowledge Richard Huizenga for his assistance on the translation of the Fortran code. Finally, I would specifically like to mention that the current interest in 3DXRD techniques and synchrotron radiation within Delft University has contributed considerably to creating a working environment in which I felt I was constantly being challenged to get the most out of this project.

I could not have completed this project without the unconditional support of my family, my friends, and my girlfriend.

Teun van der Zijden  
Delft, April 2007



Contents

Preface ..... i

Summary ..... vi

1. Introduction ..... 1

1.1. Problem formulation ..... 1

1.2. Outline ..... 2

2. Phase transformations in carbon steel ..... 4

2.1. Carbon steel phase diagram ..... 4

2.2. Austenite-to-ferrite phase transformation ..... 5

2.2.1. Grain nucleation ..... 6

2.2.2. Grain growth ..... 11

3. Experimental procedure ..... 14

3.1. Three-dimensional x-ray diffraction microscopy ..... 14

3.1.1. 3DXRD setup ..... 15

3.1.2. Experimental approach ..... 20

3.1.2.1. Box scan methodology ..... 22

3.1.3. Theoretical considerations ..... 24

3.2. Computational analysis and project goal ..... 26

4. Results – computational methodology ..... 28

4.1. Global outline ..... 28

4.1.1. General difficulties ..... 31

4.2. Pre-analysis ..... 31

4.2.1. Spatial distortion reconstruction ..... 32

4.2.2. Dark current characterization ..... 34

4.2.3.	Beam center determination	35
4.2.4.	Detector tilt determination	37
4.2.5.	Sample-detector distance determination	39
4.3.	Peak detection.....	40
4.3.1.	Diffraction ring definition	42
4.3.2.	Masking	43
4.3.3.	Criterion – threshold intensity	44
4.3.4.	Criterion – local maximum	45
4.4.	Spot characterization .....	46
4.4.1.	Spot dimension refinement	48
4.4.2.	Spatial distortion correction	52
4.5.	Spot grouping.....	54
4.5.1.	Matching of spots	55
4.5.2.	Intensity profile and center of mass computation	57
4.6.	Reflection coupling.....	59
4.7.	Grain characterization.....	60
<b>5.</b>	<b>Results – microstructure reconstruction .....</b>	<b>62</b>
5.1.	General characteristics .....	62
5.2.	Pre-analysis.....	64
5.2.1.	Spatial distortion reconstruction	64
5.2.2.	Dark current characterization	64
5.2.3.	Beam center determination	67
5.2.4.	Detector tilt determination	68
5.2.5.	Sample-detector distance determination	69
5.3.	Peak detection.....	70
5.3.1.	Output characteristics	70
5.3.2.	Background intensity	71
5.3.3.	Peak count dependence on stripe	73
5.3.4.	Peak count dependence on diffraction ring	75
5.3.5.	Peak count dependence on azimuthal angle	76
5.4.	Spot characterization .....	77
5.4.1.	Output characteristics	77
5.5.	Spot grouping.....	81

5.5.1. Output characteristics 81

5.5.2. Intensity profiles 83

5.6. Reflection matching .....83

**6. Conclusions and recommendations ..... 86**

6.1. Conclusions ..... 86

6.1.1. On the computational methodology 86

6.1.2. On the microstructure reconstruction 87

6.2. Recommendations .....88

**Bibliography..... 90**

## Summary

In polycrystalline materials the microstructure is a key determinant of the material's macroscopic behavior. Properties such as tensile strength, wear resistance and fracture toughness are all determined largely by the material's structure on a microscopic level. Two processes that play a crucial role in the evolution of a polycrystalline microstructure are grain nucleation and grain growth. Therefore, insight into the dynamics of these phenomena is vital for obtaining comprehension of microstructure development and control of the accompanying product properties.

Until recently, no technique was available for the time-resolved, non-destructive characterization of the three-dimensional microstructure of an opaque polycrystalline material. When following the evolution of a microstructure in time, a trade-off between spatial and time-resolved information was always required. The recently developed technique of three-dimensional x-ray diffraction (3DXRD) microscopy, however, does provide the possibility for a high resolution in all four of these dimensions. Measurements at elevated temperatures or in controlled atmospheres are also possibilities. The technique employs high-energy x-rays to generate diffraction patterns of bulk-size samples.

In this project, a computational methodology was developed for the analysis of the data of 3DXRD measurements aimed at creating such a three-dimensional microstructure characterization. The software package was required to be time-efficient and to be easily applicable to a variety of materials. Furthermore, the software should be compatible with already existing programs aimed at different areas of 3DXRD microscopy analysis. The package was tested on a combination of two datasets available from 3DXRD microscopy experiments on a carbon steel undergoing the austenite-to-ferrite phase transformation.

The resulting software package is shown to be reasonably time-efficient, requiring about a month of computational time on a conventional PC for the analysis of the two datasets provided. In principle, the package is easily adaptable for use on different materials, and compatibility with earlier software is ensured. However, the author was unable to obtain any acceptable results when applying the software package to the two available datasets. One of the final stages of the microstructure reconstruction, in which use was made of third-party software, could not be carried out successfully. Nevertheless, it is shown that up to this point the software package produced useful intermediate results.







# 1. Introduction

## 1.1. Problem formulation

With the global production of crude steel equaling over 1.1 billion tonnes in the year 2006 [4], steel remains one of the most important structural materials available to man today. Because of its importance in so many day-to-day applications, an extensive history of research into production methods and subsequent thermal and mechanical treatments exists. This research has led to major improvements in important product properties like tensile strength or fracture toughness. Furthermore, the research process has brought the scientific community a better understanding of the microstructural mechanisms underlying such processes as phase transformations, recrystallization and solid solutioning.

Two of the most important of these microstructural mechanisms are grain nucleation and grain growth. These two occur during the processing of almost all polycrystalline materials, and together they determine to a large degree the final microstructure of the material in question, and hence its final properties. For this reason, grain nucleation and grain growth have received considerable attention in the past, and research is ongoing to keep increasing our understanding and thereby our control of these processes. However, in spite of all these efforts, the nucleation and growth phenomena are still not completely understood. Models that have been developed over the past decades have proven unable to correctly predict local behavior during the nucleation and growth of grains. Due to this ignorance, the relation between the parent microstructure on the one side and the nucleation and growth of a new phase, and hence the microstructure after transformation, on the other side is not understood to a satisfactory level yet.

A main reason for the mismatch between theoretically predicted and experimentally observed behavior has been the trade-off between temporal and

spatial resolution that often needs to be made for the gathering of experimental data. For example, data on grain growth during heat treatments are generally gathered using one of two typical strategies. While performing the heat treatment, one can constantly monitor the size of the grains at the surface of the sample, thus obtaining a high temporal resolution, yet collecting hardly any (three-dimensional) spatial information on the grain growth characteristics. Alternatively, one can first go through the entire heat treating process, and subsequently gather grain size information in three dimensions by serial sectioning of the sample, leading to a high spatial yet very small temporal resolution. Combined, series of multiple samples subjected to treatments of different durations and subsequently to serial sectioning can be used for acquiring average growth characteristics; characteristics of individual grains, however, remain unavailable. It is this inability to obtain high resolutions in four dimensions that is the main cause of grain nucleation and growth models failing in delivering high-quality predictions for local behavior.

Recently, however, a new experimental technique was introduced that is able to deliver this so eagerly strived for combination of temporal and spatial resolution. The technique in question, three-dimensional x-ray diffraction (3DXRD) microscopy, can employ the large penetration depth of high-energy x-rays to generate diffraction patterns of bulk-size samples [5]. This allows in-situ studying of samples undergoing heat treatments and therefore the gathering of four-dimensional nucleation and growth data on the level of individual grains.

However, since 3DXRD microscopy is a relatively novel technique, the methodology for analysis of the data obtained using the 3DXRD microscope has not been fully developed yet. New features and new types of experiments are constantly being designed, and development of the required methodology is often postponed to a later time. The current project aims at designing the required methodology for one specific type of 3DXRD measurements: the non-destructive, three-dimensional mapping of a polycrystalline microstructure – more specifically a fully austenitic grain structure – at an elevated temperature. A software package is designed which transforms the raw data contained in the x-ray diffraction images into a reconstruction of the original three-dimensional microstructure. The package is subsequently tested on two available datasets.

## **1.2. Outline**

This report presents the results of the thesis described in the previous section. Excluding the current chapter, the report has been divided into five parts.

Chapter 2 provides the reader with an introduction into the theory underlying phase transformations in low alloy steels. The iron-carbon phase diagram is discussed,

and some of the main theoretical aspects underlying the phenomena of grain nucleation and grain growth are presented.

Chapter 3 continues by introducing the experimental procedure followed during the experiments under consideration in this project. The technique of three-dimensional x-ray diffraction microscopy is outlined, and the experimental settings related to this specific project are discussed. Chapter 3 also specifies more precisely the aim of this project, and presents some general desired characteristics of the software.

Chapter 4 moves on to the first part of the results. This part focuses specifically on the design of the software package. The overall layout is given, and the individual processes are discussed.

Chapter 5 contains the second part of the results, namely the outcome of the application of the newly developed software package to two datasets available from the experiment described in chapter 3. Details on intermediate results from the various steps are presented.

Chapter 6, finally, draws some conclusions on the basis of the results presented in the previous chapters. Furthermore, some recommendations related to possible future work are given.



## 2. Phase transformations in carbon steel

This chapter presents some of the theory on crystallographic phases and phase transformations on low-alloy carbon steel. It serves to familiarize the reader with the theoretical principles that will be applied and to which will be referred in the chapters to come.

Section 2.1 introduces low-alloy carbon steels and their crystallographic phases on the basis of a schematic phase diagram. Section 2.2 treats the principal phase transformation in carbon steels, the austenite-to-ferrite transformation.

### 2.1. Carbon steel phase diagram

Steels are a group of alloys, the main components of which are iron and carbon; the latter is usually present in concentrations up to 2 weight percent (in this case the steel is termed ‘carbon steel’). Many additional elements can be added to improve the various properties of the material; common alloying elements for steel are for example magnesium, nickel, manganese, and molybdenum. Carbon steels can be present in three distinct crystallographic phases: ferrite, austenite, and cementite. Ferrite consists of a body-centered cubic (bcc) crystal of iron atoms, in which carbon atoms are dissolved interstitially. It is designated as either  $\alpha$ -Fe or  $\delta$ -Fe, depending on the temperature at which the ferrite is present. The maximum concentration of carbon in  $\alpha$ -Fe – the low-temperature ferrite of interest to this project – is about 0.02 wt.%. Austenite (referred to as  $\gamma$ -Fe) is formed by a face-centered cubic crystal of iron atoms in which carbon atoms are interstitially dissolved up to the afore-mentioned concentration of about 2 wt.%. Cementite, finally, is an iron carbide ( $\text{Fe}_3\text{C}$ ) with an orthorhombic structure that is usually designated as the  $\theta$ -phase.

Figure 2.1 shows a typical quasi-binary phase diagram depicting the various (combinations of) phases and their corresponding temperature regimes. This phase diagram applies to a carbon steel with small amounts of alloying elements; this is

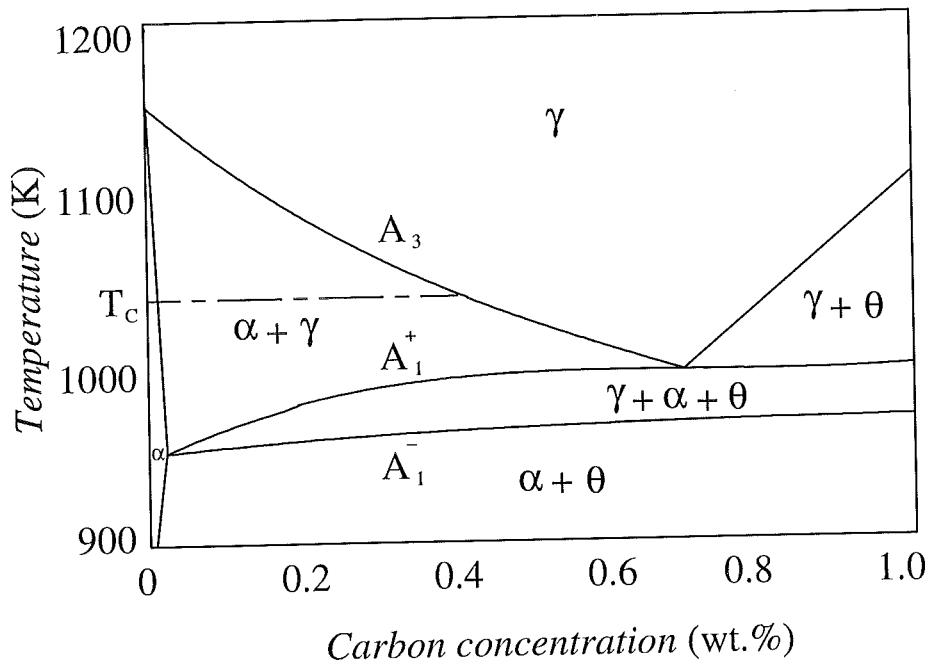


Figure 2.1: Typical Fe-C quasi-binary phase diagram for a low-alloy carbon steel. The presence of alloying elements leads to the formation of a three-phase region in which austenite ( $\gamma$ ), ferrite ( $\alpha$ ) and cementite ( $\theta$ ) coexist. Figure taken from [1].

apparent through the splitting of the  $A_1$ -line, leading to a three-phase region in which austenite, ferrite and cementite mutually coexist. Typically, during the final steps of processing the material will reach temperatures corresponding to the austenite region of the phase diagram – obviously, the upper and lower limit of this range will depend on composition – after which cooling back to room-temperature occurs and hence the single-phase ferrite- or two-phase (ferrite+cementite)-region is entered (again depending on composition). The way in which this phase transformation from austenite to ferrite occurs therefore largely determines the resulting microstructure, and hence the final material properties.

## 2.2. Austenite-to-ferrite phase transformation

As stated above, the austenite-to-ferrite transformation is an important determinant of the final microstructure of a processed steel. The temperature at which this solid-state phase transformation commences strongly depends on composition and, referring to Figure 2.1, is given by the  $A_3$ -line. As the steel is cooled from a temperature within the single-phase austenite region to temperatures below the  $A_3$ -line, so-called pro-eutectoid ferrite is formed and a dual-phase structure develops. As the temperature drops below the  $A_1^+$ -line, the steel briefly enters the three-phase region, leading to the formation of a small amount of cementite, until the  $A_1^-$ -line is

crossed. At this point, the remaining austenite is transformed into a combination of ferrite and cementite. Barring rapid cooling rates (which can lead to the formation of different phases), the ferrite and austenite forms colonies of pearlite, a lamellar structure of interpenetrating crystals of the two phases.

The final properties of the steel are largely determined by the characteristics of these ferritic and pearlitic phases. Features such as the shape of the grain size distribution and the amount of residual stress within the grains are known to have a large influence on the resulting material properties. A prime example of this is the Hall-Petch equation, dictating a linear relationship between the strength of the material and the inverse square root of the average grain size [6, 7]. From this it follows that control of the formation of the ferrite and pearlite is crucial to controlling the final material properties.

The formation of the ferritic phase in the  $(\alpha+\gamma)$ -region can be divided into two mechanisms known as grain nucleation and grain growth. Both mechanisms have been modeled separately, and have their own specific time- and temperature-dependence. The following presents the main features of the models on both of these processes. Firstly, the basics of grain nucleation are explained on the basis of the classical nucleation theory [8-11]. Secondly, grain growth theory is introduced based on the model developed by Zener [12].

### 2.2.1. Grain nucleation

The positions of the lines that mark the various regions in a typical phase diagram like Figure 2.1 follow from equations for the Gibbs free energies of the various phases (for a discussion on the construction of phase diagrams from free energy relations, see for instance [13] or [14]). In fact, a phase diagram is nothing more than a graphical representation of which (combination of) phase(s) results in the lowest Gibbs free energy for each combination of composition and temperature. It follows that when one changes the temperature of a material in such a way that one crosses from one region in the phase diagram into the next, a driving force for the corresponding phase transformation will develop. However, the presence of this driving force does not directly lead to formation of the new phase: first, nucleation needs to occur.

At all temperatures but absolute zero, thermal motion will introduce local variations in composition and structure of the material. Clusters of atoms constantly form and subsequently decompose again. The formation of such a cluster of  $j$  atoms can be represented using a reaction equation:



The equilibrium constant  $K_j$  for this chemical reaction is then given by

$$K_j = \frac{a_{A_j}}{(a_A)^j} \approx \frac{x_{A_j}}{(x_A)^j} \quad (2.2)$$

in which  $a_{A_j}$  and  $a_A$  represent the activities of the cluster and of the individual atom, respectively. In the case of an ideal-dilute solution, Henry's law and Raoult's law dictate that the activities of the cluster and of the individual atom can be approximated by their respective molar fractions  $x_{A_j}$  and  $x_A$ .

The change in Gibbs free energy that is associated with the formation of such a cluster of atoms,  $\Delta G_j$ , can now be linked to the equilibrium constant of equation (2.2) in the following manner:

$$\Delta G_j = -k_B T \ln(K_j) \quad (2.3)$$

*Waarom?*

where  $k_B = 1.38 \times 10^{-23}$  J/K represents the Boltzmann constant and  $T$  represents the temperature in Kelvin. When looking at  $\Delta G_j$  as the change in Gibbs free energy on the formation of a cluster of ferrite from the austenite matrix at the start of the phase transformation,  $\Delta G_j$  can be related to the Gibbs free energies per unit volume of the austenite and ferrite,  $G^\gamma$  and  $G^\alpha$ , in the following way:

$$\Delta G_j = -V(G^\gamma - G^\alpha) = -V\Delta G_v \quad (2.4)$$

in which  $V$  represents the volume of ferrite formed by the cluster of  $j$  atoms, and  $\Delta G_v$  the difference between the free energies per unit volume of the two phases. Equation (2.4) shows that when the Gibbs free energy of the ferrite is lower than that of the austenite,  $\Delta G_j$  is negative, thus lowering the energy of the system.

However, whether or not the cluster will be stable and continue to grow as a ferrite grain, or whether it will be unstable and dissolve back into the matrix, does not only depend on the driving force for nucleation  $\Delta G_v$ . There are three other changes in the total energy of the system that play a role during nucleation of a new ferrite grain on an austenite grain boundary, edge or corner (the preferred nucleation sites) [13]:

1. The removal of an area  $A^\gamma$  of austenite-austenite grain boundary with grain boundary energy  $\gamma^\gamma$  leads to a reduction in Gibbs free energy of  $A^\gamma \gamma^\gamma$ ;

2. The creation of an area  $A^{\alpha\gamma}$  of austenite-ferrite grain boundary with grain boundary energy  $\gamma^{\alpha\gamma}$  leads to an increase in Gibbs free energy of  $A^{\alpha\gamma}\gamma^{\alpha\gamma}$ ;
3. The fact that the newly created ferrite does not fit perfectly into the space previously occupied by the austenite results in a misfit strain that generates an increase in Gibbs free energy of  $V\Delta G_s$ .

Combined with the contribution from the driving force for nucleation as described by equation (2.4), this results in an overall change in energy of the system  $\Delta G$  of:

$$\Delta G = -V(\Delta G_v - \Delta G_s) + \sum_i A^i \gamma^i \quad (2.5)$$

in which the summation runs over all interfaces that play a role during the creation of the ferrite nucleus.

The misfit strain  $\Delta G_s$  effectively reduces  $\Delta G_v$ , but is usually assumed to be zero because there are no accurate data available on its value [15, 16]. Furthermore, we know that the ferrite volume increases with  $z_v R^3$ , in which  $z_v$  is a geometrical parameter related to the shape of the nucleus and  $R$  is the nucleus size. The various interfacial areas appearing in equation (2.5) can be written as  $z_A^i R^2$ , where  $z_A^i$  is a geometrical parameter depending on the  $i^{\text{th}}$  surface. Using these three relations, the total change in Gibbs free energy of the system can be expressed as a function of nucleus size  $R$ :

$$\Delta G = -z_v R^3 \Delta G_v + R^2 \sum_i z_A^i \gamma^i \quad (2.6)$$

Figure 2.2 depicts the relation of equation (2.6), displaying the two separate terms on the right-hand side as well as the combined effect of the two. Together, the two energy terms produce a maximum in  $\Delta G$  of  $\Delta G^*$  at a cluster radius of  $R^*$ . This maximum is called the activation energy for nucleation, and the radius at which this occurs is known as the critical nucleus size. The critical size and the activation energy follow from equation (2.6) by setting the derivative with respect to  $R$  to zero:

$$R^* = \frac{2 \sum_i z_A^i \gamma^i}{3 z_v (\Delta G_v - \Delta G_s)} \quad (2.7)$$

$$\Delta G^* = \frac{4}{27} \frac{\left( \sum_i z_A^i \gamma^i \right)^3}{z_v^2 (\Delta G_v - \Delta G_s)^2} \quad (2.8)$$



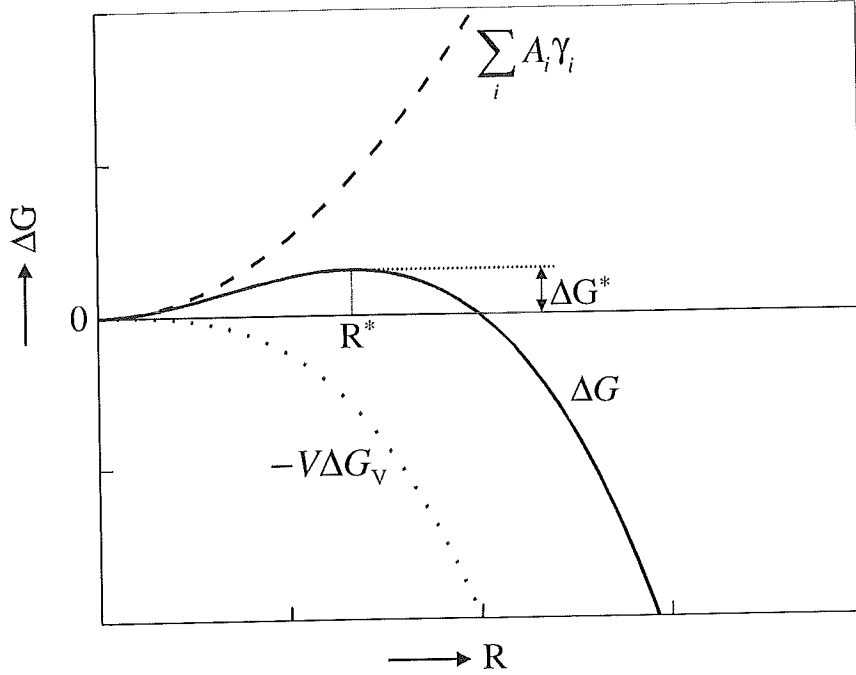


Figure 2.2: The change in total Gibbs free energy  $\Delta G$  as a function of cluster size  $R$ . The combined function (solid line) is the sum of the contributions of the difference in free energy per volume of the two phases (dotted line) and of the annihilation and creation of the various surfaces (dashed line). This leads to a maximum in  $\Delta G$  of  $\Delta G^*$  at radius  $R=R^*$ , the critical nucleus size.  $\Delta G^*$  is called the activation energy for nucleation. Figure taken from [1].

When a cluster with size  $R < R^*$  is formed, the energy of the system will be lowered when this cluster dissolved back into the matrix. However, when  $R > R^*$  for a specific cluster, the system's energy will be lowered by actually increasing the cluster's size. Hence,  $\Delta G^*$  should be interpreted as the amount of energy that needs to be added to the system (by the afore-mentioned thermal motion) in order for a cluster to be able to continue to grow and develop into a grain.

The values of many of the parameters included in equation (2.8) are unknown, or known only with a large uncertainty. The exact shape of the critical nucleus, included in (2.8) through the geometrical parameters  $z_A^i$ , has not yet been determined experimentally, and values for the interfacial energies  $\gamma^i$  are also notoriously difficult to obtain. Therefore equation (2.8) is sometimes written as [1]

$$\Delta G^* = \frac{\Psi}{\Delta G_v^2} \quad (2.9)$$

in which

$$\Psi = \frac{4 \left( \sum_i z_A^i \gamma^i \right)^3}{27 z_v^2} \quad (2.10)$$

The parameter  $\Psi$  now contains all information on the nucleus shape and on the interfaces involved in the nucleation process.

The key to determining an adequate value for  $\Psi$  lies in obtaining knowledge of the interfacial energy terms. The interfacial energy depends on the exact characteristics of the interface at hand. Figure 2.3 show a schematic representation of a general interface. The definitions of the misorientation  $\theta$  and of the boundary inclination  $\varphi$  are also presented in this figure. The energy of the interface depends on the values of these two parameters. For instance, Read and Shockley derived the following general equation for the interfacial energy of a low-angle grain boundary (misorientation no larger than  $15^\circ$ ) [17, 18]:

$$\gamma = \gamma_0 \theta (A - \ln \theta) \quad (2.11)$$

in which  $\gamma_0$  and  $A$  are parameters depending on the boundary inclination  $\varphi$  but independent of the misorientation  $\theta$ .

However, a simple two-dimensional representation of the interface like in Figure 2.3 can be deceptive. It should be understood that in the general three-dimensional case of a real grain structure, any interface present requires a total of five parameters for a full description: a unit vector describing the direction in which one of the grains has been rotated with respect to the other grain (two parameters), the exact angle of rotation about this axis (one parameter), and another unit vector describing the plane of the interface (two parameters). So, theoretically, by deriving a description of the interfaces present in a microstructure in terms of these five parameters, and subsequently relating this description to the observed locations where the nuclei form, the parameter  $\Psi$  from equation (2.10) can be evaluated.

*Is it de  
enige  
moelijkheid?*

The nucleation behavior predicted by the classical nucleation theory (applied

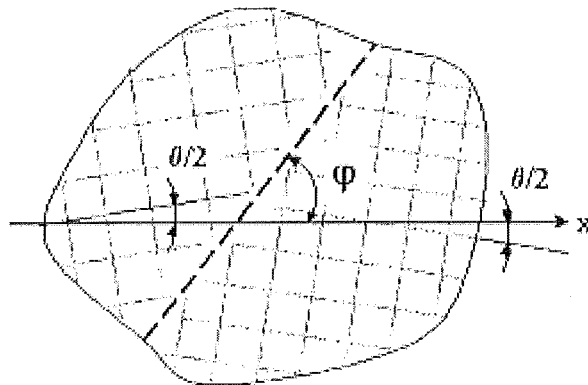


Figure 2.3: Schematic representation of an interface. The definitions of the misorientation  $\theta$  and boundary inclination  $\varphi$  are shown. Image taken from [2].

to the case of the austenite-to-ferrite transformation in low-alloy carbon steel) can be summarized in the following manner. When the two-phase region of the phase diagram is entered, a driving force for nucleation will develop; the larger the undercooling (the difference between the  $A_3$ -temperature and the actual temperature), the larger the driving force. However, on the formation of a cluster of atoms with the ferritic structure, other energy terms come into play that actually raise the total energy of the system, ~~leading to an activation energy~~. Therefore, an amount of energy needs to be added to the system (through thermal motion) to overcome this activation energy. If enough energy is added, the cluster will be able to continue to grow and develop into a ferrite grain. If the amount of energy does not suffice, the cluster will dissolve back into the matrix. The energies of the interfaces involved in this process are a major determinant of whether the cluster will continue to grow or will dissolve again.

7

### 2.2.2. Grain growth

When the activation energy for nucleation is overcome, a stable cluster of atoms has formed which will subsequently form the nucleus of a new ferrite grain. This nucleus will now increase its size by the process of grain growth.

The most prominent model for the grain growth of a pro-eutectoid phase like the ferrite under consideration is the model by Zener [12]. This model was first presented by Zener in his 1949 article, and predicts parabolic growth kinetics for a spherical grain growing in an infinitely large matrix in case the growth is diffusion-limited. As mentioned in section 2.1, the solubility of carbon in ferrite is two orders of magnitude lower than in austenite. Hence, when pro-eutectoid ferrite is formed, the residual carbon piles up at the ferrite-austenite interface, eventually diffusing away into the austenite. This diffusion forms the rate-limiting step during the transformation, and therefore Zener's theory can be applied to this situation.

During the early stages of the transformation, when growth is not yet influenced by the diffusion fields or grain boundaries of neighboring grains (called soft and hard impingement, respectively), Zener predicts the radius of a ferrite grain  $R^\alpha$  to develop with time  $t$  in the following manner:

$$R^\alpha(t) = \chi \sqrt{D_{C,V}^\gamma (t - t_s)} \quad (2.12)$$

where  $t_s$  is the time of nucleation of the grain.  $\chi$  is a proportionality constant, known as the three-dimensional parabolic thickening constant, that is dependent on the carbon solubilities of the ferrite and austenite and can be approximated by [12, 19]:

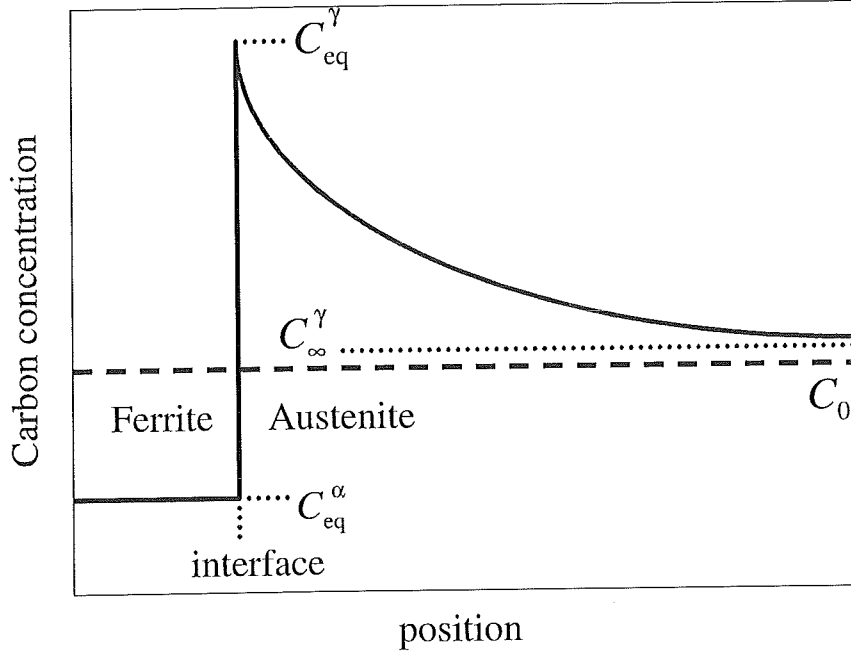


Figure 2.4: Schematic representation of the carbon concentration profile at the ferrite-austenite interface during diffusion-controlled growth. Carbon piles up at the interface within the austenite because the carbon solubility in ferrite is considerably smaller than in austenite. Figure taken from [1].

$$\chi = 2.102 \left( \frac{C_{\infty}^{\gamma} - C_{eq}^{\gamma}}{C_{eq}^{\alpha} - C_{\infty}^{\gamma}} \right)^{0.5871} \quad (2.13)$$

in which the various concentrations refer to the situation of Figure 2.4. This figure schematically depicts the carbon concentration profile around the ferrite-austenite interface during diffusion-controlled growth of ferrite into the austenite.  $C_{eq}^{\alpha}$  and  $C_{eq}^{\gamma}$  represent the equilibrium carbon concentrations in the ferrite and austenite, respectively, which follow from the phase diagram.  $C_{\infty}^{\gamma}$  represents the carbon concentration in the austenite far away from the interface, and  $C_0$  for the overall average carbon concentration in the material. In a first approximation,  $C_{\infty}^{\gamma}$  and  $C_0$  can be assumed to be equal.

The volume diffusion coefficient of carbon in austenite, indicated as  $D_{C,V}^{\gamma}$  in equation (2.12), was found by Ågren to depend on temperature and composition in the following manner [20-22]:

$$D_{C,V}^{\gamma} = 4.53 \times 10^{-7} \left( 1 + Y_c (1 - Y_c) \frac{8339.9}{T} \right) \exp \left\{ - \left( \frac{1}{T} - 2.221 \times 10^{-4} \right) (17767 - 26436 Y_c) \right\} \quad (2.14)$$

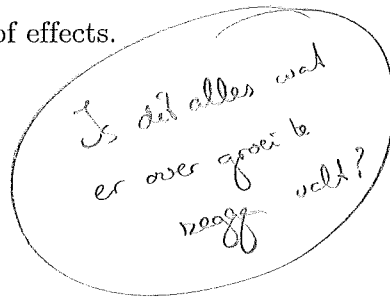
with  $D_{C,V}^{\gamma}$  in units of  $\text{m}^2/\text{s}$ , and temperature  $T$  in K. The composition dependence of  $D_{C,V}^{\gamma}$  is reflected through the variable  $Y_c$ , the so-called carbon site fraction of the

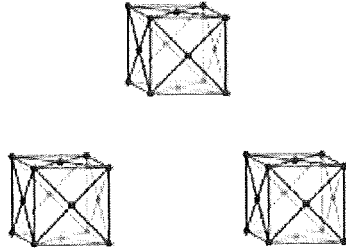
*is the C-dependence  
neglected in Å's model?*

interstitial sub-lattice, which is related to the nominal atomic fraction of carbon in the alloy in the following way:

$$Y_C = \frac{x_C}{1 - x_C} \quad (2.15)$$

As mentioned above, the Zener model applies only to diffusion-limited growth without any soft or hard impingement, and assumes an infinitely large parent matrix. Furthermore, the effects of for instance non-spherical grain shapes are not taken into account. Various modifications have been applied to the Zener model over the past years (for instance [23, 24]) to include these types of effects.





### 3. Experimental procedure

Chapter 2 has introduced the reader to the basic theoretical concepts of phases and phase transformations in low-alloy carbon steel. The chapter mainly focused on the two important microstructural processes of grain nucleation and grain growth in relation to the austenite-to-ferrite transformation. References to more thorough treatments of the various topics were included.

The current chapter will go into more detail on the experimental procedure. The chapter is divided into two parts. Section 3.1 will discuss the experimental technique that was used for obtaining the data analyzed in this project. Subsection 3.1.1 first treats the setup of the 3DXRD microscope. Subsection 3.1.2 then moves on to present the specific settings that were used during the gathering of the data under investigation in the current project. Subsection 3.1.3 introduces the basic theoretical considerations related to 3DXRD. After section 3.1 has presented this introduction into the experimental technique, section 3.2 will elaborate on the goal of this project. This goal is based on the computational analysis required after 3DXRD microscopy data collection. The section elaborates on the required computational infrastructure for the data analysis, and formulates the exact aim of the current project.

#### 3.1. Three-dimensional x-ray diffraction microscopy

Three-dimensional x-ray diffraction (3DXRD) microscopy is a relatively new technique, which employs the large penetration depth and high intensity of a focused beam of x-rays to generate diffraction patterns from the grains in polycrystalline samples [5]. In this manner, information about the behavior of individual grain inside the bulk of these materials can be obtained. Over the past years, various researchers have presented results which indicate the promising possibilities opened up by this experimental technique [25-28].

This section gives a thorough description of three-dimensional x-ray diffraction microscopy. The section is divided into three subsections. Subsection 3.1.1 presents the setup of the 3DXRD apparatus. The various components of the system are discussed, and numerous variables used in later stages are introduced. Subsection 3.1.2 then goes on to present the exact approach adopted during this specific experiment. Special attention is paid to a novel type of data collection, the so-called box scan methodology. Subsection 3.1.3, finally, presents the prime theoretical considerations behind this technique. The most important equations from diffraction theory are presented, in combination with their application to the situation at hand.

### 3.1.1. 3DXRD setup

The three-dimensional x-ray diffraction (3DXRD) microscope used for gathering the data analyzed in this study is located at beamline ID11 of the European Synchrotron Radiation Facility (ESRF). Figure 3.1 shows a schematic representation of the setup of the 3DXRD microscope as it was used for the collection of the data analyzed during this project. The white beam of x-rays (entering from the left in Figure 3.1) was first diffracted from the bent silicon Laue crystal, which monochromated the beam at 80 keV (providing a penetration depth in steel of about 5 mm. [29]) and

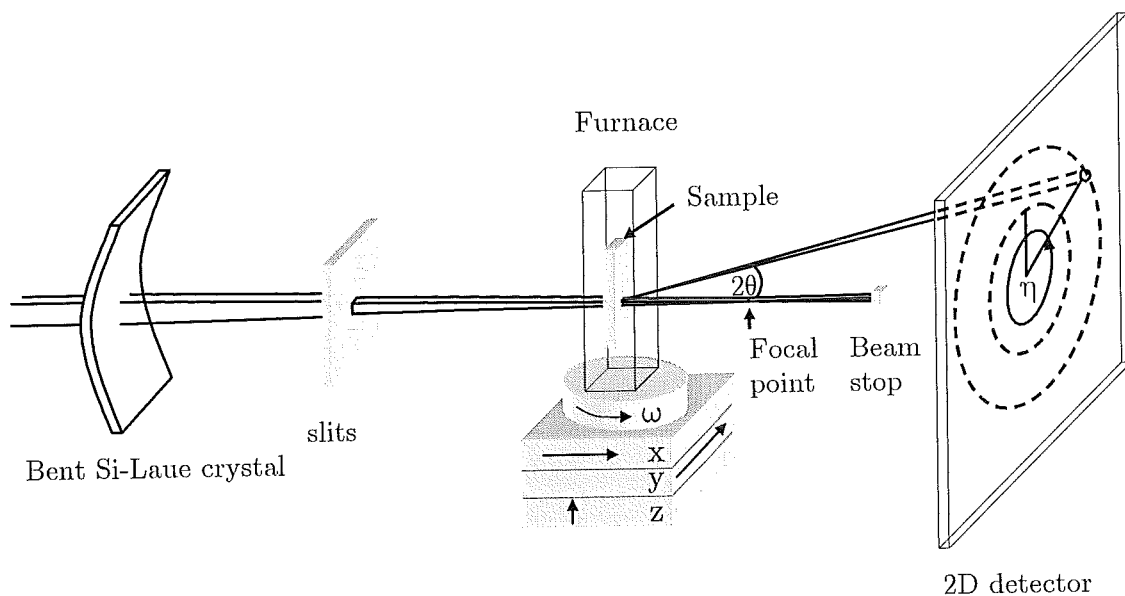


Figure 3.1: Schematic representation of the setup of the three-dimensional x-ray diffraction microscope at beamline ID11 of the ESRF used for the experiments under consideration. The setup consists of a bent Si-Laue crystal, slits, and a two-dimensional detector. The sample is positioned in a furnace which is mounted on a table, allowing the sample to be translated and rotated. Figure taken from [1].

focused it vertically. Subsequently, two sets of slits defined the size of the beam that would strike the sample. Positioning the sample out of focus allowed the beam size to be altered during the experiment using the slits. The sample itself was placed in a furnace specifically designed for these types of measurements. This furnace enabled the in-situ studying of the austenite-to-ferrite transformation. It was mounted on a table, allowing translations in three directions ( $x$ ,  $y$ ,  $z$ ) as well as rotations about the vertical ( $\omega$ ). Rays diffracted from the sample were recorded using a two-dimensional detector (a Frelon2K CCD camera; for specifications, the reader is referred to the corresponding section of the website of the ESRF [30]). Rays passing through the sample undiffracted were prevented from reaching the detector by means of a beam stop placed in their path.

Figure 3.2 shows a typical diffraction pattern recorded during a 3DXRD measurement. Various rings can be identified, each corresponding to a specific group of reflections from a specific phase. Each diffraction ring visible in the figure is in fact an ensemble of many individual reflections. This implies that by using a small beam size compared to the average grain dimension, each grain in reflection can be identified individually, since there will only be a limited number of grains in reflection

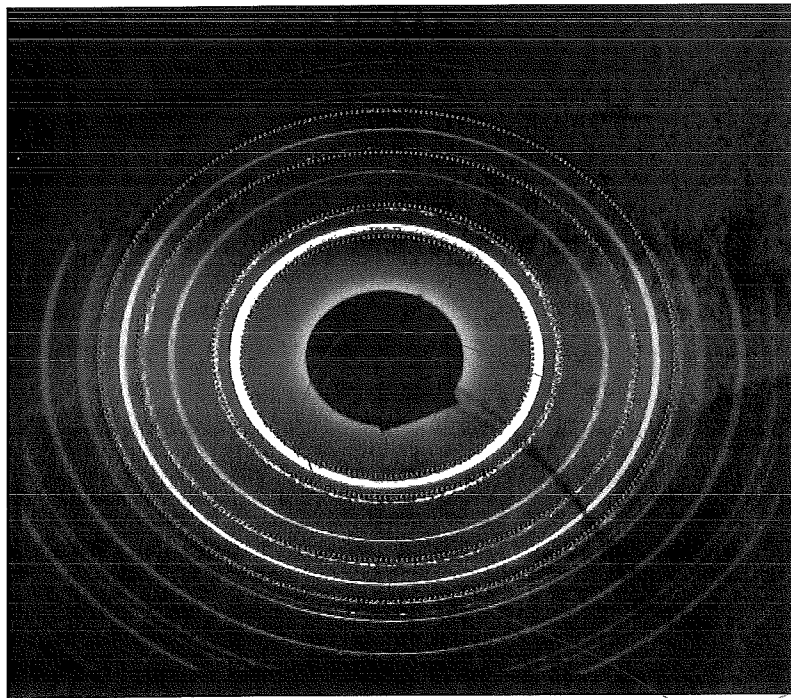


Figure 3.2: Diffraction image from the 3DXRD microscope of a steel sample at 823 K, showing the reflections from the austenite and ferrite phases. The solid circles represent the expected locations of the reflections from the austenite grains. From the inside outwards till the outermost solid circle, the following diffraction rings can be discerned:  $\gamma_{111}$ ,  $\alpha_{110}$  (close to  $\gamma_{111}$ ),  $\gamma_{200}$ ,  $\alpha_{200}$ ,  $\gamma_{220}$ ,  $\alpha_{211}$ ,  $\gamma_{311}$ . Figure taken from [3].



at each time and therefore overlap between diffraction spots will be minimized. As it is in Figure 3.2, the individual spots overlap and create a single blurred ring. *so slow a better example!*

A grain is in reflection when it obeys Bragg's law, which relates the wavelength of the incident photons  $\lambda$  and the spacing of the planes of the  $\{hkl\}$ -reflection  $d_{hkl}$  to the angle  $\theta$  between the incident photons and the diffraction plane (defined as in Figure 3.1) [31]:

$$n\lambda = 2d_{hkl} \sin(\theta) \quad (3.1)$$

in which  $n$ , the order of the reflection, is usually taken as 1 (first-order reflection). The planar spacing  $d_{hkl}$  is related to the lattice-spacing  $a$  according to

$$d_{hkl} = \frac{a}{\sqrt{h^2 + k^2 + l^2}} \quad (3.2)$$

Typical recording times for a diffraction pattern like the one shown above are in the order of 1 second.

The pattern visible in Figure 3.2 is typical of a microstructure from the two-phase region of the phase diagram, with both austenite and ferrite grains producing reflections. Since austenite and ferrite each have their own specific lattice parameter  $a_\gamma$  and  $a_\alpha$ , generally the rings of their reflection spots will fall on different locations on the detector. In fact, using the Bragg criterion of equation (3.1) one can predict for each combination of crystal phase and  $\{hkl\}$ -reflection where the corresponding diffraction ring will end up. In Figure 3.2 the solid circles indicate the expected locations of the austenite reflections. As can be seen, some of the austenite rings are clearly separated from the neighboring rings, whereas others fall on nearly the same location as one of the ferrite rings. *why  $\rightarrow \{100\}$ ?*

When recording a diffraction pattern, the sample is rotated by a small amount  $\Delta\omega$  about the  $z$ -axis to ensure that all of the intensity originating from a grain in reflection is recorded. This small rotation is meant to compensate for the mosaicity of the grain, which results in small distortions of the planar spacing. However,  $\Delta\omega$  cannot be chosen too large, since this would result in overlap from other grains that have an orientation within  $\Delta\omega$  from that of the grain under consideration.

The various types of spot overlap that might play a role during data analysis are illustrated in Figure 3.3. For each scenario, a schematic plot of intensity  $I$  versus azimuthal angle  $\eta$  is given, as well as a sketch of the reflecting grains' "positions" in  $(\omega, \eta)$ -space. Scenario A depicts the desired situation. The orientation of the grain is located entirely within the range  $[\omega_0 - \Delta\omega ; \omega_0 + \Delta\omega]$ , implying that the grain's entire reflected intensity will show up in a single diffraction image. Additionally, there are

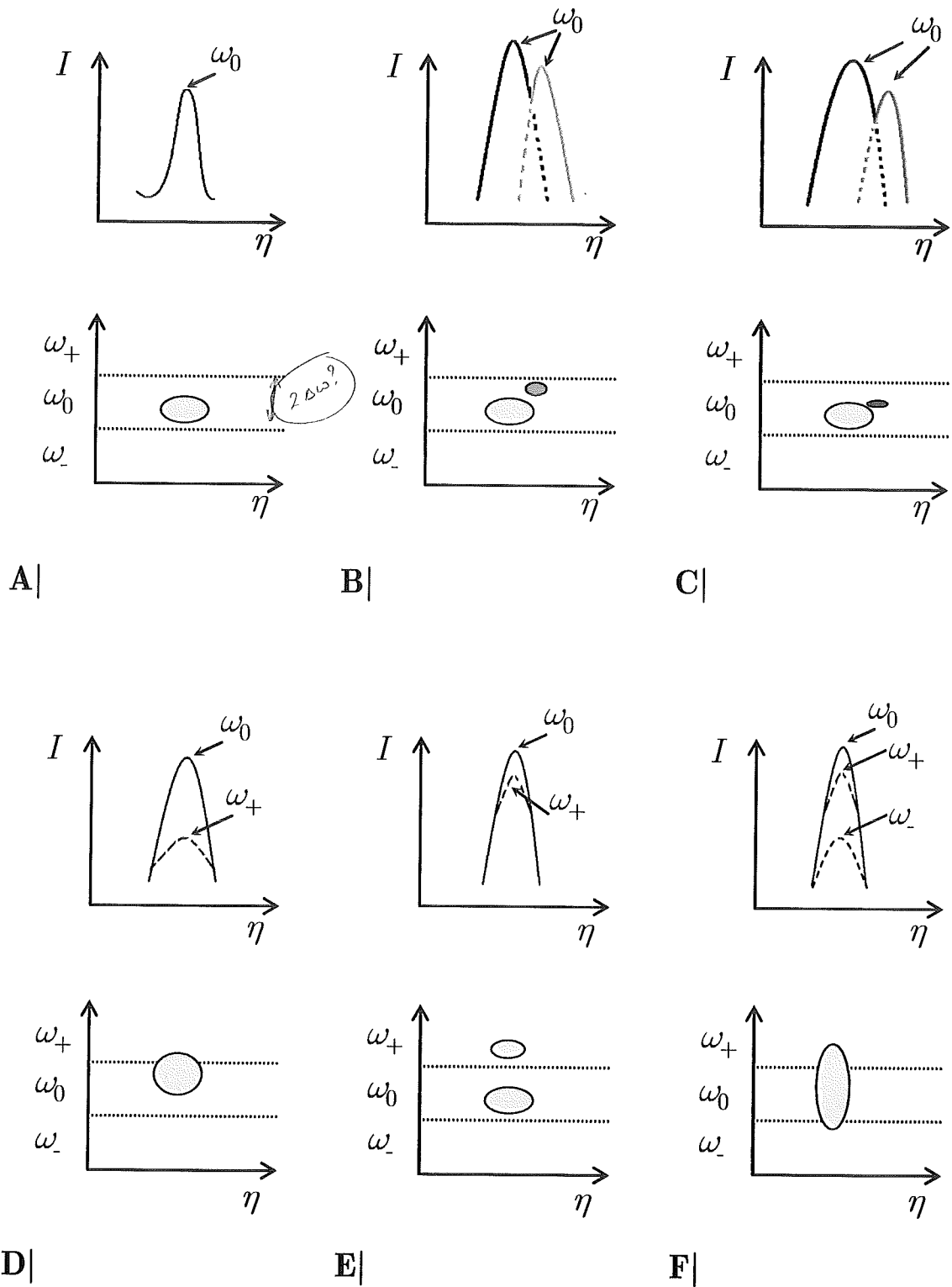


Figure 3.3: Various types of spot overlap which might play a role during 3DXRD data analysis. A| shows the simplest situation: a specific reflection has no overlap with other reflections in either the  $\eta$  or  $\omega$  direction. B| shows spots overlapping in the  $\eta$  direction which can be solved by reducing the value of  $\Delta\omega$ ; for C| this is not possible. D| and F| depict reflections with intensity in two or three separate images. E| shows two separate spots resembling a single reflection. Image adopted from [3].

no grains within the illuminated volume which diffract at both the same value for  $\eta$  and the same value for  $\omega$ . The absence of any type of overlap facilitates a straightforward analysis of the spot. Scenario B|, however, is slightly more complicated. Due to the presence of two grains producing reflections that overlap in the  $\eta$  dimension and lie within the same  $\omega$ -region, the corresponding diffraction image (the plot of  $I$  versus  $\eta$ ) will show two overlapping spots. However, this can be solved by choosing a smaller value for  $\Delta\omega$ . C| depicts a similar situation; here, however, the two grains overlap not only in the  $\eta$ - but also in the  $\omega$ -direction, meaning that reduction of  $\Delta\omega$  will not be a solution to the overlap problem. These two peaks are not fit for analysis (unless some peak fitting procedure is incorporated to divide the total intensity in two, but this would complicate the analysis significantly).

afterwards?

Whereas the first three scenarios depict situations in which all of the grains' intensity was located within a single diffraction image, D| through F| illustrate the possibility of a spot being divided over multiple, subsequent images. D| shows how the range in orientation of a single diffracting grain (due to such effects as crystal mosaicity or lattice strains) might actually end up in two different  $\omega$ -bins, resulting in two spots belonging to one and the same reflection. To calculate the intensity of a specific reflection, this possible width in the  $\omega$ -direction should also be taken into account. Therefore, for any detected spot a check is made of the neighboring images in  $\omega$ -space to determine whether or not any intensity belonging to the same reflection is located in those images. If so, then the intensities are summed. This problem could be circumvented by increasing the value of  $\Delta\omega$ ; however, this also increases the chance of two individual grains incorrectly being regarded as one. This can be understood by referring to E|. In case the value of  $\Delta\omega$  is increased to try and prevent the splitting up of diffraction spots as illustrated in D|, the chance of incorrectly summing two separate spots like in E| simultaneously increases. This indicates the presence of an optimal value for  $\Delta\omega$ . Scenario F|, finally, shows how the splitting of spots might spread out over even more images, again depending on  $\Delta\omega$ .

Does that resolve D from E?

Figure 3.3 only illustrates the types of overlap that might be found within a dataset. The degree to which any of these types of overlap plays a role for a specific set depends on the characteristics of the corresponding measurement. For instance, the presence of significant lattice strains within the material increases the chance of scenarios D| or F|. Small beam sizes, on the other hand, decrease the likelihood of spots overlapping like in B| or C|.

### 3.1.2. Experimental approach

The data that were analyzed in this research project were recorded during an experiment at the ESRF conducted in the beginning of March 2005. The goal of this experiment was to record, in a single measurement, the following characteristics of the phase transformations in a low-alloy steel:

1. The three-dimensional austenitic microstructure at the onset of the transformation;
2. The nucleation and growth of the ferrite grains as the pro-eutectoid transformation progressed;
3. The three-dimensional ferritic/austenitic microstructure after completion of the transformation;
4. The nucleation and growth of the pearlite colonies as the eutectoid transformation progressed.

The steel used in this experiment was a high-purity iron-carbon-manganese alloy. Its exact chemical composition is given in Table 3.1. The sample was cylindrically shaped with a diameter of 1 mm. and a height of 4 mm.

Table 3.1: Chemical composition of the steel studied in the current research, in weight percentages.

Element	C	Mn	Fe
Amount (wt.%)	0.077	2.89	rem.

$A_1, A_3?$

Nucleation and growth kinetics of the austenite-to-ferrite transformation in low-alloy carbon steel have been analyzed using synchrotron radiation before [27]. That study, however, was limited in the sense that the kinetics could not be linked to the parent microstructure. Therefore, in this experiment the microstructures before and after complete transformation have also been scanned. The objective now is to be able to deduce the correlation between parent microstructure, evolution of the new phase, and resultant microstructure. This could be achieved by describing the microstructures in terms of the grain boundaries present, and linking these descriptions to the observed locations where the ferrite nuclei form (see subsection 2.2.1).

Figure 3.4 shows the time-temperature plot for the entire experiment. Different stages during the experiment correspond to different moments during the transformation as listed above. Before the start of the experiment ( $t < 0$ ), the sample was heated to a temperature of 950 °C (1223 K). At  $t = 0$ , the experiment started

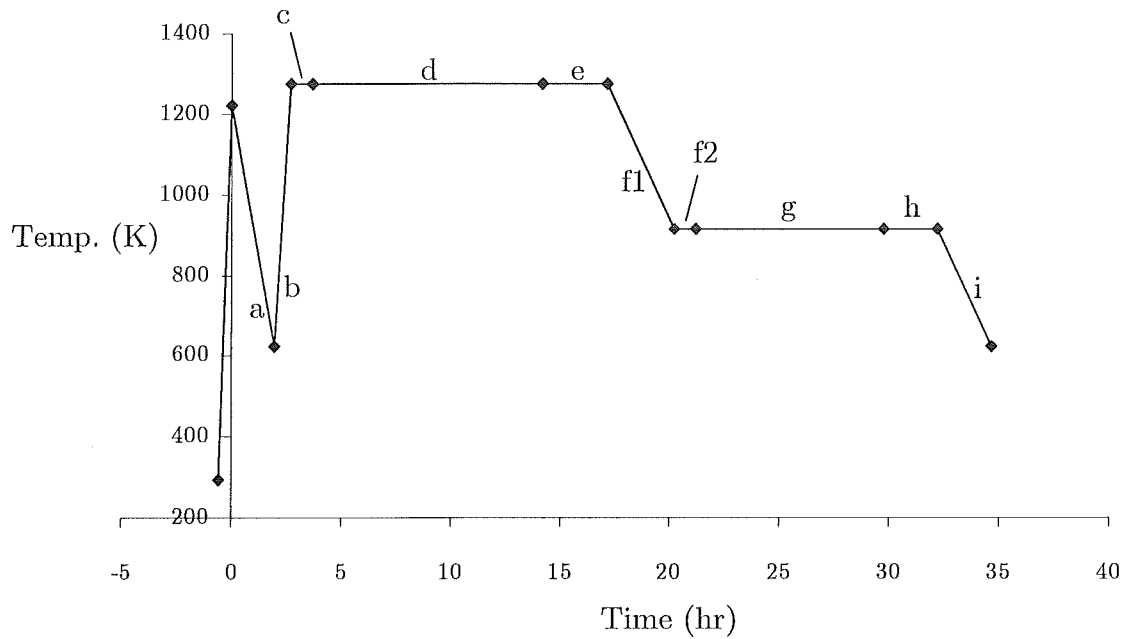


Figure 3.4: Time-temperature profile of the experiment that was conducted in March 2005 at the ESRF. Various stages, corresponding to different moments during the transformation, can be recognized. The project at hand focuses on datasets *d* and *e*.

with cooling the sample to 350 °C at a rate of 5 °C/min. This part of the experiment was termed part *a*, and was carried out to determine the final ferrite fraction after transformation as well as the  $A_3$ -temperature (see Figure 2.1). During part *b*, the sample was reheated again to 1000 °C at 15 °C/min to induce austenitizing. The sample was then held at this temperature for an hour (part *c*) to allow the austenite structure to stabilize. During parts *d* and *e*, part of the sample was scanned to obtain three-dimensional data on the austenite structure. A more thorough treatment of the experimental procedures of parts *d* and *e* will follow below. Temperature was then lowered to 640 °C at 2 °C/min (part *f1*) to obtain data on the transformation kinetics. After temperature was held constant at 640 °C for an hour (*f2*), two new scans were performed to obtain data on the ferrite/austenite microstructure that had evolved during the transformation (parts *g* and *h*). Finally, during part *i* temperature was lowered again to 350 °C to be able to compare the resultant ferrite fraction to that obtained in part *a*.

The current project focused on datasets *d* and *e*. Together, these two series of measurements provide the necessary information to be able to reconstruct the austenite microstructure at the time of the measurements. The experimental methodology employed during the recording of these datasets is a derivation of procedures from earlier work [32-34], and is termed the box scan methodology. An in-depth explanation of this box scan will now follow.

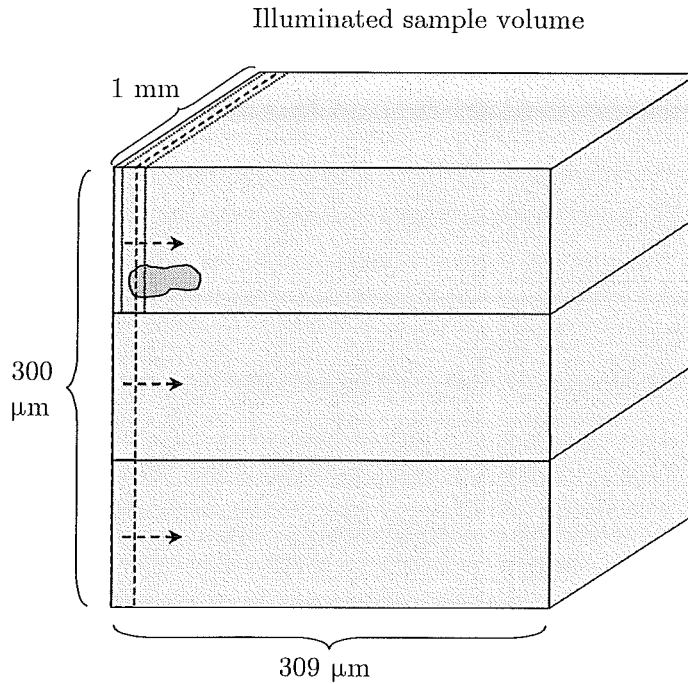


Figure 3.5: Schematic representation of the box scan methodology applied to the  $d$  series of measurements. The sample volume of  $309 \times 300 \times 1000 \mu\text{m}^3$  is illuminated by a beam with a line profile of  $15 \times 100 \mu\text{m}^2$ . The scan is performed in three sets (stripes). For each stripe, the width of  $309 \mu\text{m}$  is scanned using 50 slit positions (layers). Each layer is translated by only  $5$  or  $7.5 \mu\text{m}$  compared to its precursor. The depicted grain will produce intensity under multiple subsequent slit positions.

#### 3.1.2.1. Box scan methodology

The box scan methodology is based on using a combination of horizontal and vertical scans (in this case the  $d$  and  $e$  series, respectively) to obtain a good resolution in both these directions. Figure 3.5 shows a schematic representation of the principle of the box scan, applied to the  $d$  series of measurements (the horizontal scans).

The slits that define the beam size at the sample (see Figure 3.1) set the beam dimensions to  $15 \times 100 \mu\text{m}^2$ . In this way only a small layer of the sample volume is illuminated at all times. This line beam is now scanned over the area of the material for which one wants to determine the microstructure. One of the advantages of using a line beam and subsequently running this line over the surface, instead of simply illuminating the entire volume of interest at once, was mentioned in subsection 3.1.1; the number of grains in reflection is low at all times, which prevents (to a large degree) the overlap of spots on the detector. However, for the objective of these measurements (creating a three-dimensional reconstruction of the austenite structure of the material before the start of the transformation), the line beam provides two other important advantages. Since the illuminated volume is much smaller, when a

reflection is recorded the possible center of mass location of the corresponding grain is also known with less uncertainty. The uncertainty in grain position is lowered even further by employing the extra information available due to the overlap between subsequent slit positions of 10 or 7.5  $\mu\text{m}$ <sup>1</sup>. Additionally, the significant reduction in uncertainty offers the possibility of retrieving information on the grains' shapes from the line beam data.

The scan is performed in three parts, so-called stripes (numbered 0 through 2 from the top downwards). Each stripe contains 50 layers, numbered 0 through 49. For each layer setting, the sample is rotated about the  $\omega$ -axis over a range of 92° (from -29.5° to +61.5°) to ensure that all grains within the illuminated volume have been in reflection at least once. This rotation is performed in 92 steps of 1°; for each  $\omega$ -value, a separate diffraction pattern is recorded. During the recording of such a diffraction pattern, the sample is rotated a small amount  $\Delta\omega/2$  about the  $\omega$ -axis in either direction. This rotation compensates for the mosaicity of the grains, as explained in subsection 3.1.1. Typical mosaic angular ranges for undeformed samples are in the order of 0.01° to 0.1° [35]; for the datasets used in this research, a value of  $\Delta\omega = 1^\circ$  is taken. For this value, given the small beam sizes used, overlap of spots in the  $\omega$ -dimension is not expected to occur.

The  $e$ -series was recorded in comparable fashion. Instead of a vertical beam profile performing a horizontal scan, the line beam was oriented horizontally and the scanning was done vertically. However, the dimensions of the beam were 300×15  $\mu\text{m}^2$ , and the scan could therefore be performed in one single stripe instead of three. The use of three stripes during experiment  $d$  was necessary due to the characteristics of the x-ray beam coming from the synchrotron. Because this beam was already focused somewhat in the vertical direction (the point of origin of the x-rays was ellipse-shaped with its major axis along the horizontal), it proved impossible to obtain a beam with a height of 300  $\mu\text{m}$  that also had a high enough intensity required for these experiments. Therefore, the horizontal scanning had to be performed by means of three 100  $\mu\text{m}$  high stripes. This problem did not occur for the horizontal beam profile, and the vertical scan could be performed in a single go. Note that scanning with a smaller beam height does not increase the final spatial resolution in that direction. After all, after both scans have been performed, the results from both sessions can be combined: for each peak found during the  $d$  measurements, the results from  $e$  can be reviewed to retrieve the same peak from that dataset (and vice versa).

beam profile?

<sup>1</sup> Originally, the intention was to apply translations of 6  $\mu\text{m}$  between all subsequent layers. However, the motor driving the slit positions proved to be able to increment the slit positions only with steps of 2.5  $\mu\text{m}$ . Therefore, the periodicity in the translations was set to 5-7.5-5-7.5-5  $\mu\text{m}$ , leading to a 30  $\mu\text{m}$  increment per 5 layers, or an *average* of 6  $\mu\text{m}$  per layer.

why?  $\Rightarrow$  so why not simply 5 or 7.5  $\mu\text{m}$ ?

In this way, the final resolution in both the horizontal and vertical dimension will reach an equal value of about 5  $\mu\text{m}$ .

### 3.1.3. Theoretical considerations

The diffracted intensity of a single grain  $I_g$  per unit time (assuming the rotation of  $\Delta\omega$  is enough to have the entire grain in reflection) is given by the kinematical approximation as [35, 36]:

$$I_g = \Phi_0 r_0^2 \frac{\lambda^3 |F_{hkl}|^2 V_g}{\Delta\omega v^2} L_g P \exp(-2M) \quad (3.3)$$

in which  $\Phi_0$  represents the incident flux of photons,  $V_g$  stands for the volume of the grain,  $v$  for the volume of the unit cell,  $P$  for the polarization factor, and  $\lambda$  and  $\Delta\omega$  are defined as before. The Lorentz factor  $L_g$  of the grain is given by  $L_g = 1/\sin(2\theta)$ , in which  $2\theta$  is the scattering angle.  $F_{hkl}$  represents the structure factor of the  $\{hkl\}$ -reflection. The general formula for the structure factor is as follows [35]:

$$F_{hkl} = \sum_1^N f_n \exp[2\pi i(hu_n + kv_n + lw_n)] \quad (3.4)$$

The summation runs over all  $N$  atoms within the unit cell. The  $(u, v, w)$ -trebles represent the locations of the atoms (fractional coordinates with respect to the lattice parameter), and  $f_n$ , known as the atomic form factor, represents the scattering power of the  $n^{\text{th}}$  atom. For austenite for instance (ignoring the interstitial carbon), equation (3.4) gives as structure factor  $F_{\gamma hkl}$ :

$$F_{\gamma hkl} = f_{Fe} [1 + (-1)^{h+k} + (-1)^{k+l} + (-1)^{h+l}] \quad (3.5)$$

in which  $f_{Fe}$  is the form factor of an iron atom. Equation (3.5) is equivalent to:

$$F_{\gamma hkl} = \begin{cases} 4f_{Fe} & h, k, l \text{ all even or all odd} \\ 0 & h, k, l \text{ of mixed parity} \end{cases} \quad (3.6)$$

indicating that for reflections for which  $h, k, l$  are not all either even or odd, there will be zero resultant intensity. These are known as forbidden reflections.

The constant  $r_0$  in equation (3.3) is known as the Thomson scattering length, and is given by

$$r_0 = \frac{e^2}{4\pi\epsilon_0 m_e c^2} = 2.82 \times 10^{-15} \text{ m} \quad (3.7)$$



with  $e = 1.602 \times 10^{-19}$  C being the electron charge,  $m_e = 9.1094 \times 10^{-31}$  kg the electron mass,  $c = 2.9979 \times 10^8$  m/s the velocity of light, and  $\epsilon_0 = 8.85419 \times 10^{-12}$  F/m the permittivity of vacuum. The Debye-Waller factor  $\exp(-2M)$  accounts for thermal vibrations of the atoms.  $M$  is given by [36, 37]:

$$M = \frac{6h^2T}{mk_B\Theta^2} \left[ \phi(x) + \frac{x}{4} \right] \left( \frac{\sin(\theta)}{\lambda} \right)^2 \quad (3.8)$$

Here,  $h = 6.62608 \times 10^{-34}$  Js is Planck's constant,  $m$  is the mass of the atom (for iron,  $m_{Fe} = 9.27 \times 10^{-26}$  kg),  $k_B = 1.381 \times 10^{-23}$  J/K is the Boltzmann constant,  $\Theta$  is the Debye temperature (for iron,  $\Theta_{Fe} = 430$  K),  $x = \Theta/T$  is the relative temperature, and  $\phi(x)$  is the first-order Debye function:

$$\phi(x) = \frac{1}{x} \int_0^x \frac{\xi}{\exp(\xi) - 1} d\xi \quad (3.9)$$

In deriving equation (3.3), it is assumed that the crystal rotates about an axis perpendicular to both the primary beam and the scattering vector. If that is the case, an angular rotation of  $\Delta\omega$  corresponds to a change in scattering angle of  $\Delta 2\theta$ . In general, however, the scattering vector will make an angle  $\eta$  with the  $z$ -axis unequal to  $90^\circ$  (see Figure 3.1). In that case, rotating over  $\Delta\omega$  will only produce a change in scattering angle of  $\Delta\omega \sin \eta$ . This extra  $|\sin \eta|$ -term needs to be included in equation (3.3). Furthermore, the time-dependence of the grain volume  $V_g$  can also be included in the expression for  $I_g$ . When these two factors are taken into account, equation (3.3) is extended to:

$$I_g = \Phi_0 r_0^2 \frac{\lambda^3 |F_{hkl}|^2 V_g(t)}{\Delta\omega |\sin \eta| v^2} L_g P \exp(-2M) \quad (3.10)$$

Clearly, for the determination of  $v$  (the volume of the unit cell) as well as for evaluation of the lattice spacing of the Bragg criterion, equation (3.2), the lattice parameter of the phase under consideration is required. For austenite, this lattice parameter  $a_\gamma$  can be evaluated as a function of carbon concentration and temperature using the following equation [38]:

$$a_\gamma = (3.6306 + 0.78x_C) \left( 1 + (24.9 - 50x_C)(T - 1000) \times 10^{-6} \right) \quad (3.11)$$

in which  $T$  is again the temperature in Kelvin, and  $x_C$  represents the atomic fraction of carbon in the material. The resultant lattice parameter is given in Ångström.

## 3.2. Computational analysis and project goal

Section 3.1 has introduced the reader to the experimental technique of three-dimensional x-ray diffraction microscopy. It was shown how a two-dimensional detector was used to collect diffraction patterns on the various stages of the austenite-to-ferrite transformation in a mm-size low-alloy steel sample. The measurements considered in the project at hand, series *d* and *e* (see subsection 3.1.2), were treated in more detail, after which the principal equations related to 3DXRD were presented.

However, although the theory of 3DXRD is well established (see for instance the afore-mentioned [35] or [36]), this does not yet hold for the computational analysis connected to this technique. Since 3DXRD microscopy is a relatively new experimental technique, the computational methodology and accompanying software are not yet developed to a degree sufficient to provide off-the-shelf solutions for the various types of problems encountered during the data analysis. Efforts are ongoing to add to the pool of 3DXRD analysis software [32, 39, 40]. Referring to the numbering used in subsection 3.1.2, for instance, software for the analysis of datasets *a* and *f1* is available. In fact, some interesting earlier publications using 3DXRD data have reported the analysis of these types of cooling curves [27, 28]. However, the analysis of datasets like *d* and *e*, or *g* and *h*, has not, to the author's knowledge, been carried out before. Therefore, a large portion of the software required for the analysis of these datasets still needed to be written after the data had been collected.

As described earlier, this specific project focused at the analysis of datasets *d* and *e*. The goal of this project was to write the software required for the analysis of these datasets, involving read-in of the data, intermediate processing, and final reconstruction and visualization of the austenite structure. In fact, the goal of this project was formulated in the following manner:

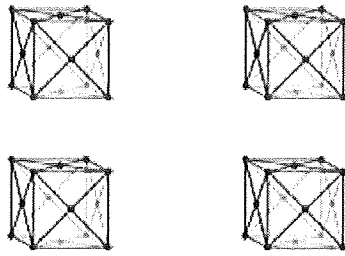
*Develop a software package for the three-dimensional reconstruction of a polycrystalline microstructure from three-dimensional x-ray diffraction microscopy data, and apply this package to an available dataset.*

This reconstruction comprises the position (in terms of center of mass), crystallographic orientation, and volume of the individual grains. Additionally, visualization of the grains' shapes might be achieved by employing each grain's fractional intensities coming from the line beam measurements.

The main desired characteristics for the software package were the following:

1. Efficiency: Being a clear plus for any software package, efficiency is especially desired in this case given the large amount of data;
2. Generality: Although the package is tested on the reconstruction of an austenitic microstructure, it should be easily adaptable to fit other steel phases (ferrite) or other materials;
3. Compatibility: The package should, as much as possible, be compatible with software already written, most notably the software available for analysis of the austenite-to-ferrite transformation as used in earlier work [27, 28];
4. User-friendliness: The various programs should be well documented and easily readable.

A point of consideration when trying to achieve the second characteristic is for instance the amount of hard-coding of variables. This should be prevented as much as possible, since hard-coded variables complicate any future adaptation to new datasets. Regarding the compatibility issue, obvious strengths would be to write the package in the same language as the already existing software, and to use as much as possible the same variable designations as in earlier work.



## 4. Results – computational methodology

After the introduction into phase transformations in carbon steel provided by chapter 2, chapter 3 elaborated on the experimental technique of 3DXRD microscopy. It also dealt with the specifics of the experiment under consideration; 3.1.2 treated the 3DXRD settings of the current experiment, and section 3.2 stated the goal of this project.

The results of this thesis have been divided into two parts. The first part consists of a description of the software written for the analysis of 3DXRD microstructural data; the second part comprises the results of the application of the package to the datasets outlined in the previous chapter. The current chapter will present the first part of the results. Section 4.1 presents the global architecture of the software package. It identifies the different steps required for the microstructure reconstruction, and introduces some of the difficulties one can expect to encounter during such a procedure. After this first introduction into the methodology, the subsequent sections continue to discuss the individual processes. These descriptions do not go into too much detail. For more detailed descriptions of the individual routines, including transcripts of the exact code, the reader is referred to the appendix which is added to this report as a separate supplement.

### 4.1. Global outline

This section introduces the basic outline of the microstructure reconstruction. It briefly introduces the various parts of the methodology, which are then elaborated on in subsequent sections.

First of all, a small word is required on the terminology used in the remainder of this report. The reader should be aware of the distinction made in this thesis between the terms 'reflection', 'spot' and 'peak'. A reflection is defined as the diffraction event from a specific grain within the sample; the locations of these

reflections are determined by the crystallographic orientation of the grain. By definition, for any reflection the entire grain obeys the Bragg criterion and diffracts. However, due to the small beam sizes used in this research, it is quite unlikely that any grain in the sample will be fully illuminated at any time. Therefore, when the Bragg criterion is fulfilled, not the entire grain but instead only parts thereof will diffract. The results of these partial diffraction events are termed spots; they are the actual intensity objects visible within the diffraction images. In other words, a single reflection will often manifest itself as multiple spots in the diffraction images. Furthermore, in the ideal case ('ideal' meaning Lorentzian diffraction spots), each spot is represented by a single peak: the pixel within that spot with the highest intensity. A peak is defined as a single pixel which has an intensity higher than a certain threshold value and which forms a maximum with respect to all its nearest neighbors in  $(x, y, \omega)$ -space.

The programming environment chosen in this project was MATLAB. Figure 4.1 shows a flow chart for the software package created for the three-dimensional microstructure reconstruction. It depicts schematically how the raw data, in the form of a large amount of diffraction patterns, are transformed into a reproduction of the original microstructure. Before analysis of the diffraction images can commence, some pre-analysis needs to be performed. This determines the values of various parameters that are required for the microstructure reconstruction. Subsequently, the diffraction patterns are read in and scanned for peaks. This produces a list of the positions of these peaks in terms of in which image they have been found and on which exact pixel. This list is then carried over to the next step, where for each peak the exact dimensions of the corresponding spot are determined. Now that for each spot its dimensions and hence its total intensity are known, the resultant list can be seen as an enumeration of all the spots in the analyzed diffraction patterns. Subsequently, the spots are grouped, combining those that belong to the same reflection. The result hereof is a list of the reflections coming from the grains in the gauge volume. These reflections all have associated center of gravity locations, total integrated intensities etc.

one peak  
per spot?

The final part consists of moving from individual reflections to real grains. This is done in two steps. Firstly, matching of different reflections that originate from the same grain takes place. On the basis of the crystal symmetry of the phase under consideration (in the case of the data investigated in this thesis: austenite), given a certain reflection, one can predict where (in  $\omega$ -space) the other reflections originating from the same grain should lie. If indeed reflections are found at these  $\omega$ -positions, and these also have their center of mass at approximately the same location as the original reflection, it is inferred that these reflections are real and originate from a

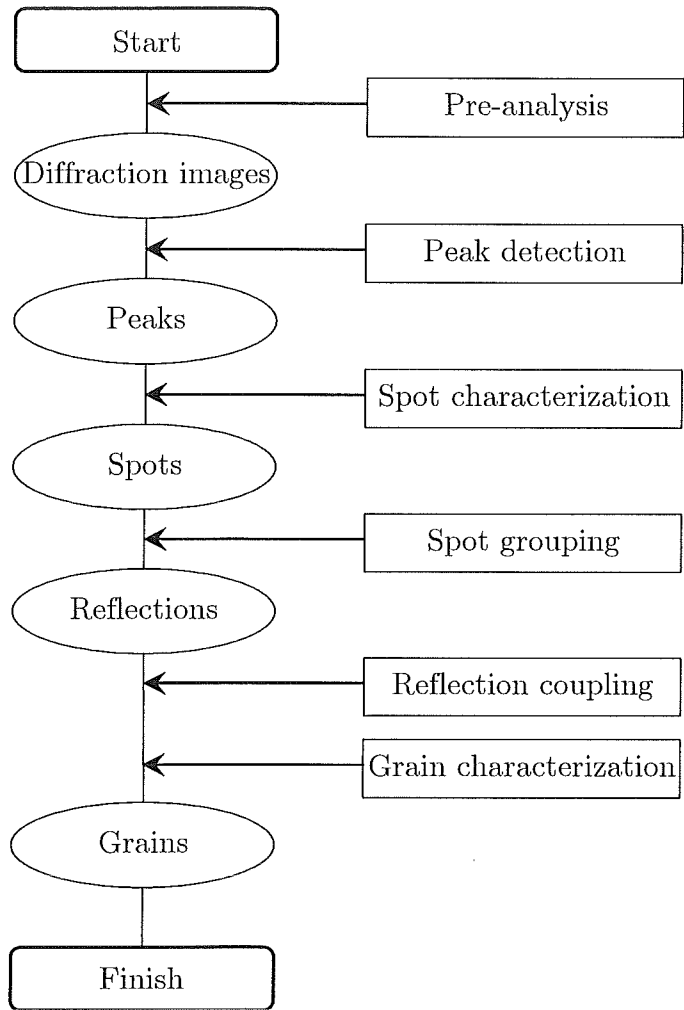


Figure 4.1: Flow chart for the package of MATLAB routines written for the three-dimensional reconstruction of a polycrystalline microstructure from x-ray diffraction data. The diffraction patterns are transformed in a stepwise manner into a reproduction of the original microstructure by the various operations listed on the right.

grain at the associated center of mass position. However, if not all expected reflections are found, the reflections might be rejected and no grain would be assigned (whether this rejection is carried out depends on exactly how many of the expected reflections are missing). Secondly, the identified grains are characterized in terms of for instance location within the sample and orientation using the individual reflections.

wat zijn mogelijke redenen voor missing reflections?

### 4.1.1. General difficulties

Before section 4.2 commences with the detailed treatment of the computational methodology, a short overview of the general difficulties expected during the analysis of these types of 3DXRD datasets might be of use.

A first complexity is the size of the datasets under consideration. With diffraction images being about 8 MB in size, the sizes of typical 3DXRD datasets range in the order of many GB. This feature implies high computational loads. Reducing the amount of data under investigation at an early stage of the analysis therefore appears desired.

Another type of difficulty is the distortions introduced into each diffraction image. In general, these distortions originate from various parts of the experimental setup and can influence the results considerably if not taken into account. Therefore, correction schemes should be designed to reverse these effects.

A diffraction image will always display a certain amount of background intensity. When the amount of background intensity is known, it is possible to correct for this effect. However, characterization of the background pattern can turn out to be a complicated process, due to multiple factors influencing the precise amount of background at any time.

A final difficulty worth mentioning beforehand is the split-up of individual reflections into multiple spots. This phenomenon was already touched upon at the beginning of this chapter. Not only does this require the locating of all spots belonging to one reflection, but it also significantly complicates the computation of a reflection's total integrated intensity. Due to the novel nature of the box scan methodology, procedures to handle these complications needed to be designed from scratch.

After this short overview of the main difficulties related to the design of the methodology created during this project (an overview which is far from exhaustive), the following section provides the reader with more detailed treatments of the various parts of the analysis. First of all, section 4.2 presents the various pre-analysis operations.

## 4.2. Pre-analysis

The pre-analysis part of the reconstruction serves to determine some parameters required for subsequent analysis of the diffraction images. Figure 4.2 depicts a flow chart of the pre-analysis process. The pre-analysis can be seen to consist of five main tasks. All five tasks provide input which is required for the correct interpretation of the diffraction images. Furthermore, the output of some of the tasks is required as

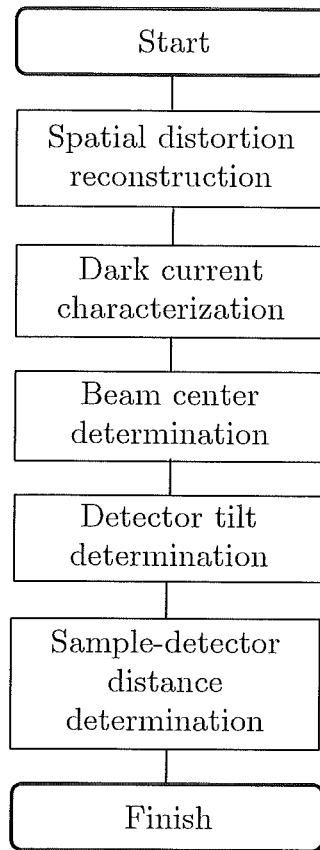


Figure 4.2: Flow chart of the pre-analysis part of the microstructure reconstruction procedure. The results from the various processes listed in the chart are required for the subsequent analysis of the diffraction patterns.

input for some of the other operations; these dependencies are the main determinants of the exact order in which the individual processes are carried out.

Firstly, the functions describing the spatial distortion present in each diffraction image are reconstructed. Subsequently, the characterization of the dark current intensity is performed, both in terms of average values as well as variations. When this background intensity has been characterized, it can be used as input for the determination of the location of the beam center. This beam center location is subsequently employed when determining the exact detector tilt. Finally, the distance between the sample and the detector is computed, requiring the detector tilt to be provided as input. The following subsections will go into more detail on these five separate processes.

#### 4.2.1. Spatial distortion reconstruction

The first, important operation that needs to be performed is the reconstruction of the function describing the spatial distortion of the diffraction images. It should be



understood that the situation of Figure 3.1, in which the diffracted x-rays simply strike the surface of the detector and are recorded, is a somewhat simplified representation. In reality, the x-rays strike a phosphor screen, which in turn generates photons with wavelengths in the visible range of the spectrum so that the CCD camera can record them. These photons are directed towards the camera using a setup of mirrors. Ideally, these mirrors do not introduce any additional errors into the data. In practice, however, they introduce a spatial distortion of the diffracted image, which can be enhanced even further by the detector's software. The general trend of this distortion is to increase with increasing distance from the detector center.

The spatial distortion distribution is a feature that depends only on the detector characteristics, and not on for instance the sample under investigation. This implies that characterizing the spatial distortion does not need to be done immediately prior to or after the experiment at hand; in fact, as long as the distortion has been characterized in the past these results can be used again to apply the necessary correction to the current experimental data. The ESRF provides a piece of software called FIT2D [41], which contains a function to apply this spatial distortion correction to an as-measured diffraction pattern. This is done by determining for each pixel the degree of distortion it has undergone, which for a given experimental setup is a function only of its location on the detector.

As input, FIT2D uses the results of an earlier characterization of the spatial distortion. Such a characterization is performed in the following manner. A mask containing holes of a known diameter at known locations is placed in front of the detector, after which an image is recorded (without any sample present). The resulting image will therefore be a dark grid with spots at the locations of the holes in the mask. Ideally, these spots would be evenly spaced on the detector with their spacing corresponding to the spacing in the mask itself. The spatial distortion, however, will lead to variations in the spacing and in the projected diameters of the holes. Two functions are now determined which produce the horizontal and vertical distortions of each pixel, respectively, as a function of its position on the detector. Instead of using a single least-squares polynomial fitting solution for the entire detector surface, FIT2D uses the more sophisticated solution of a bivariate spline function. A  $k^{\text{th}}$ -degree spline is a function which is defined piece-wise over a number of intervals by a set of polynomials of the  $k^{\text{th}}$  degree at most. The fact that the spline is bivariate in this case refers to the fact that the value of the spline at each point (for instance the amount of distortion in the diffraction image's  $x$  direction (horizontal)) depends not only on its value for  $x$  but also on its value for  $y$  (vertical direction).

For the case at hand, the distortions of the pixels in the middle of some of the holes are evaluated precisely. Any four of such neighboring pixels now define a piece of detector area for which the spatial distortion values of the corners (known in spline terminology as 'knots') are known exactly, but where for the rest of the points these values are still unknown. The spline consists of a  $k^{\text{th}}$ -degree polynomial through the knots, valid on the sub-area defined by those knots, which from then on gives the spatial distortion of all of the points in that specific area. Extra constraints on the polynomial are that the polynomial itself as well as its derivatives (up to the  $(k-1)^{\text{th}}$  one) should be continuous with respect to the polynomials of the neighboring sub-areas. By calculating the polynomials for all sub-areas, the spatial distortion of each point on the detector is derived. The result is a polynomial of degree  $k$  for which the coefficients of the various terms that make up the polynomial depend on the exact pixel under consideration. The spatial distortion is now fully determined by the list of spline coefficients that describe the polynomials at each location on the detector, together with the locations of the splines' knots. FIT2D can read in these lists of coefficients, known as splinefiles, to reconstruct the polynomials and compute the spatial distortion correction required for each detector pixel. For more information on the theory of splines and their numerical approximation, see for instance [42-44].

As explained above, the spatial distortion correction can be carried out by FIT2D. However, this program does not provide the possibility of on-line use; each image needs to be corrected manually. Given the large sizes of typical 3DXRD datasets, this is a problematic feature. The FIT2D code controlling the spatial distortion was therefore translated into MATLAB, making sure all functionalities were preserved. The MATLAB code provided the possibility of on-line use. For more information on this translation and for transcripts of the resulting routines, the reader is referred to the corresponding sections of the appendix.

#### 4.2.2. Dark current characterization

The second step of the pre-analysis part of the microstructure reconstruction is the characterization of the dark current intensities. This dark current is a near-constant electronic background to the diffraction images – present even when no sample is mounted and when the beam's shutters are closed – for which the diffraction images should be corrected. The dark current intensities are determined by averaging 22 dark current measurements. Those 22 specific dark current measurements are used because they were recorded using the same exposure time as the dataset under consideration. The *d* dataset used exposure times of 1 second, whereas the *e*-set only used 0.5 second as its exposure time; for both sets, 22 dark current images with equal exposure times are available. Each one of those 22 images was recorded at a different

$\omega$ -setting; however, since no sample was present the value for  $\omega$  should not have any influence on the intensity.

The averaging of 22 dark current images results in a new  $2048 \times 2048$  matrix, containing for each pixel on the detector the average electronic background of that specific pixel. Diffraction images can now be corrected for the electronic background by subtracting this average dark current matrix pixel for pixel. In this way, each pixel is corrected using its own specific dark current value. By correcting in this element-wise manner, another correction is made simultaneously. This correction relates to the phenomenon known as 'hot pixels': faulty pixels which register a constantly elevated value for the intensity. Since this defect is independent of whether or not a sample has been mounted or the shutters have been closed, the dark current intensity of such a pixel is expected to show the same increase in intensity. Therefore, on element-wise subtraction of the dark current intensity the hot pixels will be neutralized.

### 4.2.3. Beam center determination

When the dark current intensities have been computed, these can be used as input during the determination of the location of the beam center.

The beam center indicates the location where the undiffracted beam would strike the detector surface, had it not been blocked by the beam stop. The beam center roughly corresponds with the centers of the diffraction rings, and its location is used in determining spot characteristics like the azimuthal angle  $\eta$ . As mentioned, normally the beam stop prohibits the undiffracted beam from striking the detector surface. In some cases, however, part of the undiffracted beam is still able to reach the detector and leave a marking. In this case, such a direct beam mark provides a direct visual indication of the location of the beam center.

which?

Figure 4.3 presents the 3DXRD diffraction pattern of lanthanum hexaboride ( $\text{LaB}_6$ ). This substance is used for purposes of calibration at the ESRF. In fact, one of its uses is determination of the tilt of the detector – see subsection 4.2.4. The left-hand side of the figure shows the entire diffraction pattern. On the right-hand side, an enlargement is shown of the middle part of the pattern. This section corresponds to a part of the detector where one does not expect to find any significant intensity, since this part of the detector was shielded from any incoming x-rays by the beam stop. Still, the enhancement shows a clear intensity object located in the vicinity of the center of the detector. Note that the center of the detector can be recognized from small deviations in background intensity visible in the enhancement. The top left and bottom right show slightly higher background intensity than the top right and bottom left parts; the transitions lie exactly down the horizontal and vertical

so why  
not just  
remove the  
beam stop?

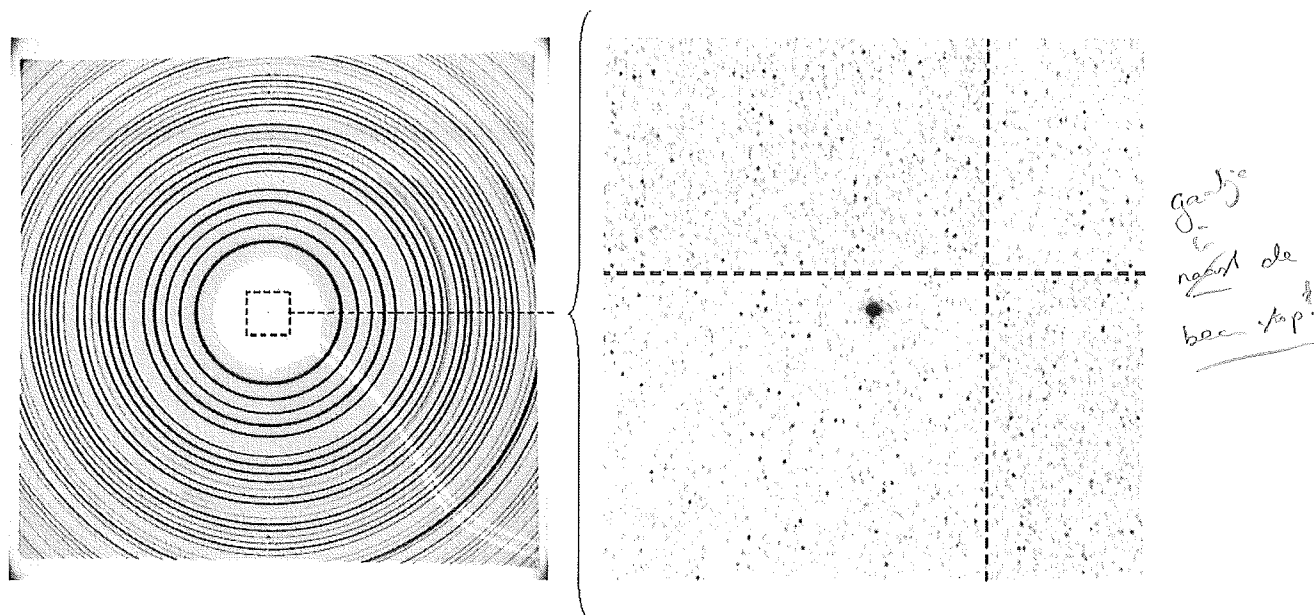


Figure 4.3: Diffraction pattern of lanthanum hexaboride ( $\text{LaB}_6$ ) used by FIT2D for the determination of the detector tilt. The left-hand side depicts the entire diffraction pattern. The right-hand side is an enlargement of the middle of the diffraction pattern, showing the direct beam mark. Note that the top left and bottom right part of the enhancement show slightly more darkening than the top right and bottom left. For reasons of clarity, the detector's middle has also been indicated using dashed lines.

middle of the detector. The effect, however, appears to be only a minor one. In fact, it might be difficult to appreciate the effect on print due to the loss of contrast; therefore, in the enlargement the horizontal and vertical middle of the detector have also been indicated by the dashed lines.

Visual inspection of the  $\text{LaB}_6$  diffraction pattern shows that the mark is located at the center of the diffraction rings, giving confidence to the assumption that we are in fact dealing with a direct beam mark. Apparently, despite the presence of the beam stop some undiffracted rays were still able to reach the detector screen. This is probably due to a small opening in the beam stop at the location where a pin diode was attached to the stop (the wiring of which is visible in the bottom right corner of the diffraction pattern).

! So why is this the centre of the beam?

Normally, instead of using a direct beam mark, the beam center is determined by using FIT2D to perform a fit on the rings of the  $\text{LaB}_6$  diffraction. In this case, however, this was not possible because the  $\{100\}$ -ring of the diffraction pattern was blocked by the beam stop, as a result of which the routine used for determining the beam center could no longer produce reliable results.

The direct beam mark provides a first visual indication of the location of the beam center. For accurate computations, however, these coordinates need to be refined. This was done in the following manner. The location of the beam mark is

taken (the coordinates of the pixel within the mark with the highest intensity), and a rectangular box is drawn around it. The exact location of the beam center is then determined by computing a weighted average of the horizontal and vertical coordinates of the pixels within this box, using the pixels' intensities as weights. Before weighing, each pixel is corrected for its dark current intensity using the correction as outlined in the previous subsection. The result of this procedure is a pair of coordinates describing the weighted average location of the beam center on the detector. These coordinates can from here on be used in determination of for instance the azimuthal angle  $\eta$  of diffraction spots. The beam center location is also used in determining the detector tilt, the following step in the pre-analysis part of the reconstruction.

why not  
calculate  
the centre  
of all rings?

#### 4.2.4. Detector tilt determination

In the experimental setup as depicted in Figure 3.1, the plane of the detector is expected to be perpendicular to the incoming beam. If this is the case, the diffraction spots will form concentric rings on the detector, one for each of the  $\{hkl\}$ -reflections. In practice, however, this ideal situation is hard to realize and a certain degree of misalignment will be introduced, resulting in diffraction ellipses instead of rings. It is possible to correct for this misalignment, but obviously to do this the exact misalignment needs to be known.

The detector tilt can be completely characterized by two angles as depicted in Figure 4.4. The plane  $A$  represents the ideal detector plane, perpendicular to the incoming beam. However, due to the misalignment the actual detector plane becomes  $A'$ . The line  $l$  is known as the rotation axis. It is formed by all points that are common to both  $A$  and  $A'$ , including the beam center (designated in Figure 4.4 as  $b.c.$ ). The line  $k$  is the vertical passing through the beam center. Together,  $k$  and  $l$  define an angle  $\eta_T$ . This angle defines in which direction the detector misalignment is oriented. The extent of the misalignment is given by the tilt angle  $\varphi$ . This is simply the angle between the ideal plane  $A$  and the actual plane  $A'$ .

FIT2D, the piece of software already introduced in subsection 4.2.1, can determine a detector's misalignment in terms of the two angles  $\eta_T$  and  $\varphi$  using its internal function TILT. It uses the diffraction pattern of lanthanum hexaboride introduced before (Figure 4.3), together with the location of the beam center derived in the previous subsection.  $\text{LaB}_6$  has a well-defined crystal structure (having a cubic unit cell with lattice parameter  $a_{\text{LaB}_6} = 4.157 \text{ \AA}$ ), which implies that when the energy of the incoming x-ray is known ( $E = 80 \text{ keV}$ ) the exact diffraction angles  $2\theta_{hkl}$  of the various  $\{hkl\}$ -reflections of  $\text{LaB}_6$  can be computed using the Bragg criterion. FIT2D can fit the experimentally observed shapes and locations of the  $\text{LaB}_6$  diffraction rings

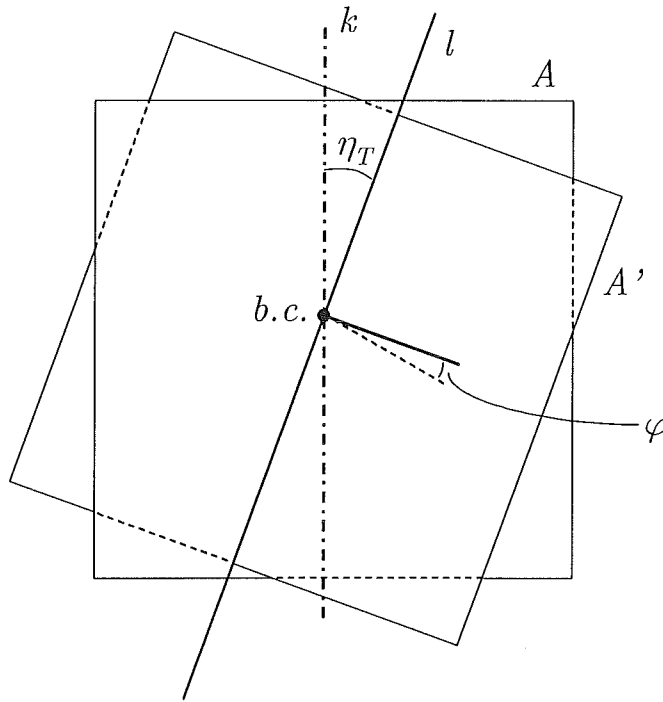


Figure 4.4: Schematic representation of the characterization of the degree of detector misalignment. When the detector screen is not placed perpendicular to the incoming beam (striking the screen at the beam center *b.c.*), the detector plane changes from the ideal plane *A* to *A'*. The degree of misalignment is completely characterized by two angles:  $\eta_T$ , the angle between the vertical *k* and the rotation axis *l*, and  $\varphi$ , the angle between *A* and *A'* (known as the tilt angle).

using  $\eta_T$  and  $\varphi$  as the fitting variables. The output of the FIT2D misalignment analysis is two angles. One of these angles is equal to the  $\varphi$  angle mentioned above. The FIT2D-definition of  $\eta$ , however, differs from that outlined in the previous paragraph. The tilt plane rotation angle of FIT2D,  $\eta_{FIT2D}$ , is defined as the anti-clockwise angle between the horizontal direction and the major axes of the diffraction ellipses. Since the major axis of such an ellipse always lies perpendicular to the rotation axis, the two tilt plane rotation angles are related by:

$$\eta_T = -\eta_{FIT2D} \quad (4.1)$$

In this manner, FIT2D provides a full characterization of the detector misalignment in terms of the two angles  $\eta_T$  and  $\varphi$ . This facilitates correction for the ellipsoidal shapes of the diffraction rings later on in the analysis.

### 4.2.5. Sample-detector distance determination

The final parameter required before analysis of the actual diffraction patterns can commence is the distance between the sample and the detector,  $L_{sd}$ . However, no measurement of this sample-detector distance was conducted during the experiments at the ESRF. So, the value of  $L_{sd}$  needs to be determined in some other manner. This was done using the LaB<sub>6</sub> diffraction image, Figure 4.3, in combination with the angle  $\eta_T$  following from the detector tilt description (Figure 4.4). Since the diffraction angles  $2\theta_{hkl}$  of the rings in the LaB<sub>6</sub> image are known, the only value required to determine the sample-detector distance is the distance  $R_{hkl}$  between the beam center and such a diffraction ring. After all, the tangent of  $2\theta$  is nothing more than the ratio between  $R_{hkl}$  and  $L_{sd}$ :

$$\tan(2\theta_{hkl}) = \frac{R_{hkl}}{L_{sd}} \quad (4.2)$$

However, this relation only holds for circular diffraction rings; when the rings have been deformed into ellipses (as a result of the detector misalignment), equation (4.2) can no longer be applied since no single value for  $R_{hkl}$  can be defined anymore.

This problem can be circumvented, though, using the rotation axis, the direction of which is defined by  $\eta_T$ . The rotation axis is formed by those points that lie both in the ideal and in the true detector plane, and therefore only contains points that have not been distorted by the detector misalignment. It follows that the distance between the beam center and the point of intersection between the  $\{hkl\}$ -ring and the rotation axis in fact equals the radius  $R_{hkl}$  of the undistorted  $\{hkl\}$ -ring. So, construction of the rotation axis  $l$  using the value of  $\eta_T$  and subsequent visual determination of the intersection between  $l$  and the LaB<sub>6</sub>  $\{110\}$ -ring gives the value of  $R_{110}$ . Using  $2\theta_{110} = 3.0^\circ$ , this then produces a value for  $L_{sd}$  in units of pixels. Similar procedures can be carried out for the other diffraction rings in the LaB<sub>6</sub> diffraction image.

In principle, a value of  $L_{sd}$  in units of pixels suffices; all subsequent computations can be performed using units of pixels as well. However, a value of  $L_{sd}$  expressed in for instance millimeters is easier to work with on an intuitive basis. Therefore, a conversion between units of pixels and unit of millimeters is desired. This conversion is not as straightforward as it might seem, though. The pixels do have well-defined physical dimensions (a width and height of 14  $\mu\text{m}$  [30]), but the effective size of a pixel can differ significantly from these. This difference can be attributed to two main factors: a scaling constant, and the pixels' point-spread function.

Regarding the scaling factor, the reader is reminded of the remark made in subsection 4.2.1, stating that the experimental setup given by Figure 3.1 is a somewhat simplified representation. The diffracted rays strike a phosphor screen, which subsequently emits photons that are guided towards the CCD camera by a system of mirrors. However, the sizes of the phosphor screen and the chip of the CCD camera differ. In fact, the combined effect of the mirrors squeezes the diffracted beams so that the dimensions of the diffraction pattern falling onto the CCD camera are actually much smaller than the pattern's real physical dimensions, resulting in a scaling down of the image. Clearly, therefore, the surface area of a CCD pixel ( $14 \times 14 \mu\text{m}^2$ ) represents a much larger area of the phosphor screen. The second reason for the uncertainty in effective pixel size is related to the point-spread function (PSF) of the pixels. The PSF of a pixel is a function describing the amount of blurring of an object registered by the pixel. For a detailed description of point-spread functions, see for instance [45]. Unfortunately, the PSF of the Frelon2K detector is not well characterized, and therefore a proper correction for the PSF (which would require some type of deconvolution scheme to reverse the blurring effect) is not feasible.

Still, a value for the effective pixel size can be retrieved from the aforementioned splinefile (the file containing the coefficients of the splines describing the spatial distortion – see subsection 4.2.1). Since the distortion characterization is performed using a mask with holes at fixed distances from each other in real space (5 mm.), the effective pixel size can be determined by relating this grid spacing to the average number of pixels between two holes on the recorded image. This produces a conversion factor which transforms  $L_{sd}$  from units of pixels to units of millimeters.

### 4.3. Peak detection

The previous section described the various operations performed during the pre-analysis part of the three-dimensional microstructure reconstruction. This pre-analysis characterizes various parameters that are required as input during the actual analysis process. The current section continues by treating the first part of the data analysis: the peak detection. Figure 4.5 depicts a flow chart of the routine carrying out this process. The routine analyzes all 92 diffraction images corresponding to a single slit setting.

The process starts by declaring some parameters. Some of these are hard-coded, others are dependent upon the stripe and layer number, which are required as input variables and define which diffraction images are to be analyzed. When the necessary parameters have been set, masks can be created which will be used to shield parts of the diffraction images. A loop over all images recorded at the slit setting under consideration is started; for each value of  $\omega$ , the corresponding image is



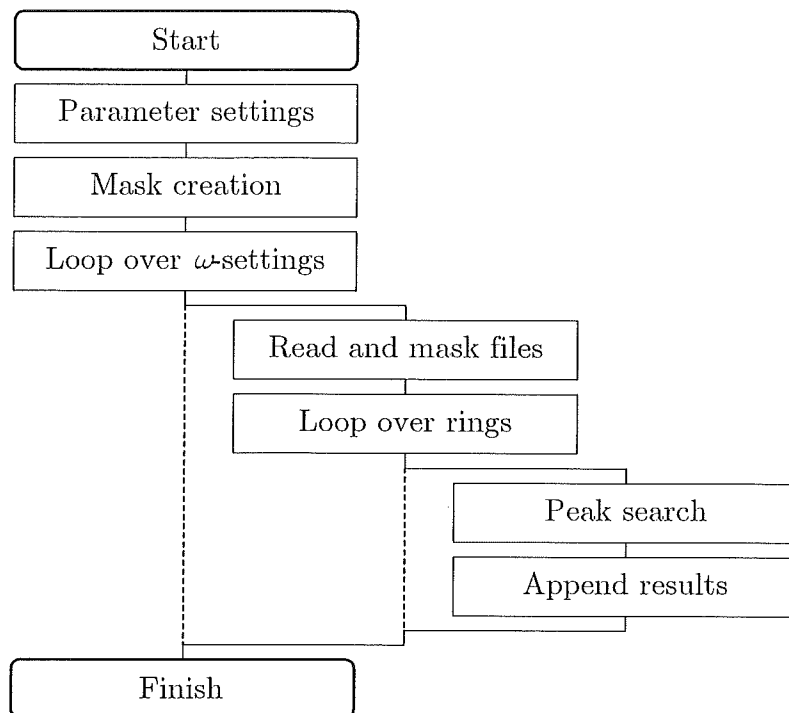


Figure 4.5: Flow chart of the peak detection process. The routine searches for diffraction peaks within the images recorded for a specific slit setting. This is done by looping over  $\omega$  and over the diffraction rings, and then performing a peak search for each iteration.

read and the masks are applied. A second loop is started, this one over the two diffraction rings of interest, after which for each ring the peak search is carried out. Results are put into a large list which is returned as output to the calling program.

Figure 4.6 shows a typical diffraction pattern considered in this project. This pattern was recorded at stripe 0, layer 0,  $\omega = -17^\circ$ , with beam dimensions of  $15 \times 100 \mu\text{m}^2$  (dataset *d*). The grayscale of the picture has been inverted to allow for easier spot identification. Spots now appear as dark marks on a lighter background. The pattern shows some interesting characteristics. First of all, the spots can be seen to lie on circles that center near the middle of the detector, as follows from the application of Bragg's law to the experimental situation at hand. Furthermore, the regions of the diffraction image where no peaks are found obviously display some considerable background intensity. Clearly, this background needs to be taken into account when performing a search for peaks. The background intensity does not appear to be constant over the entire detector; for instance, Figure 4.6 shows a difference between the background intensity on the left-hand side and on the right-hand side of the detector. Though this difference is quite pronounced in the figure due to the intensity scaling, the effect is only in the order of a few counts, i.e. in the order of 0.1 % of the average background intensity. It is probably caused by a

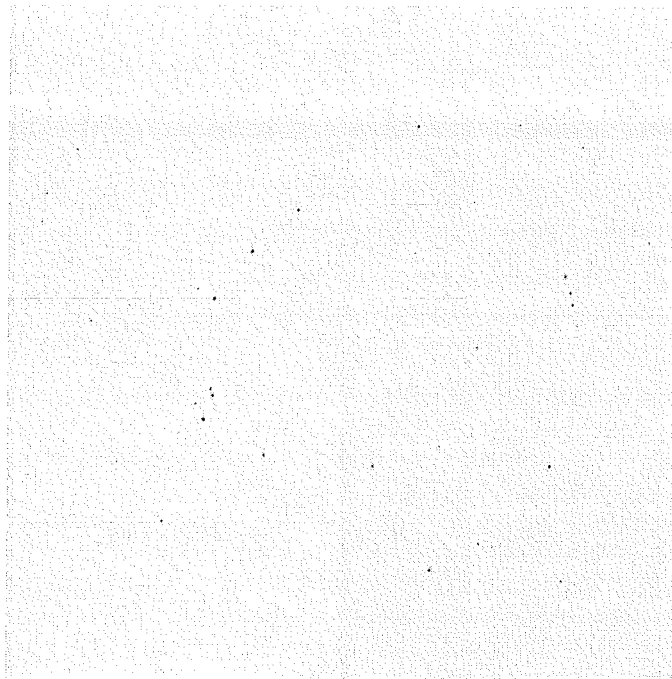


Figure 4.6: Example of a diffraction pattern reconstructed using FIT2D. This pattern corresponds to stripe 0, layer 0,  $\omega = -17^\circ$ . For easier spot recognition, the grayscale has been inverted. Notice the diffraction spots lie on circles approximately around the center of the detector. The difference in color between the left-hand side and right-hand side of the image is indicative of a small difference in background intensity between the two. This is caused by a software anomaly.

software anomaly of the Frelon2K detector. Still, given the presence of this non-constant background, the newly written software was required to be able to correct the diffraction images for this effect.

The following subsections will go into more detail on some of the issues regarding the peak detection procedure. More extensive treatments of all processes of the routine, including transcripts of the original code, can once again be found in the appendix.

#### 4.3.1. Diffraction ring definition

Some of the parameters declared at the start of the peak detection process are the angles at which the diffraction spots of the  $\{200\}$ - and  $\{220\}$ -rings are expected to be located. The Bragg criterion predicts a single, specific value for any  $\{hkl\}$ -ring: values of  $4.9^\circ$  and  $6.9^\circ$  for  $2\theta_{200}$  and  $2\theta_{220}$ , to be precise. In practice, however, a bandwidth in diffraction angle needs to be defined to ensure all peaks are taken into account. This bandwidth was determined on visual inspection of the images, and was in the order of several tenths of a degree on either side of the theoretical diffraction angle.

Various reasons for the presence of this diffraction angle bandwidth can be identified. These include the beam being slightly divergent, the beam not being monochromatic, and the presence of local variations in lattice spacing. The appendix to this report contains calculations indicating the effect of yet another factor: the (implicit) assumption of a point-sized sample. For the sample used in the experiment under consideration, this factor alone produced a contribution to the diffraction angle bandwidth of about  $0.1^\circ$ . This compares quite well to the experimentally observed bandwidths of several tenths of a degree.

### 4.3.2. Masking

Since the expected locations of the diffraction spots lie on well-defined rings (or ellipses, taking the distortion into account), most of the pixels on the detector will never belong to any spot, simply because they do not lie on these diffraction rings. These pixels can therefore be skipped during the peak detection process. This is achieved by the application of so-called masks.

Masks are matrices of the same size as the diffraction images; a separate mask is created for each diffraction ring. A mask contains only 1's and 0's: a 1 for any pixel that is located on the diffraction ring under consideration, and a 0 for any other pixel. By element-wise multiplication of the diffraction image and a mask, all pixels on the diffraction image are set to 0 except those that lie on the ring of interest: everything except the diffraction ring is masked off.

The masks are created using a small MATLAB routine written by dr.ir. Niels van Dijk of the Reactor Institute Delft. The routine takes into account the misalignment between the detector and incoming beam as characterized during the pre-analysis (see subsection 4.2.4). The masks are given an ellipsoidal shape corresponding with the shape of the distorted diffraction rings, so that no relevant data are lost as a result of the masking procedure.

Creating the masks also provides a simple, yet efficient way to reduce the peak search area of a diffraction image. By determining the locations of the outermost pixels of a mask, a rectangle can be constructed which encloses the mask under consideration. Since this rectangle is constructed using the mask's outermost pixels, it follows that the intensity of any pixel outside this rectangle has been set to 0 by the masking operation. Therefore, the peak search can be confined to the limits of the rectangular area. For rings associated with relatively small diffraction angles, using this knowledge can result in reductions in peak search area of well over 50%.

### 4.3.3. Criterion – threshold intensity

For a pixel to be designated as a peak, its intensity is required to fulfill two criteria: it has to be higher than a certain threshold value, and it needs to be a local maximum with respect to its nearest neighbors in  $(x,y,\omega)$ -space. The current subsection details the first criterion; the second criterion is outlined in the subsequent subsection.

All pixels on the detector will register a certain non-zero intensity, even when these pixels do not belong to a spot. This background intensity can be quite a significant factor. In general, the background intensity can be divided into two parts: an electronic and a non-electronic part. The electronic background, or dark current, was already introduced in subsection 4.2.2. It was described as a near-constant effect, present on every pixel on the detector. The second term is a non-electronic background contribution. This term mainly originates from various scattering effects within the sample or the furnace (thermal scattering, slit scattering etc.). The amount of non-electronic background noise is dependent on such factors as beam dimensions, beam current within the synchrotron storage ring, temperature etc. Since some of these effects show a dependence on the diffraction angle [37], this background contribution is not expected to be (near-)constant over the entire detector.

The task of the intensity criterion treated in this subsection is to pick out those pixels of which the intensities cannot reasonably be attributed to the background anymore. In other words, it searches for pixels with an unexpectedly high intensity. The general form for a criterion to fulfill a task like this is

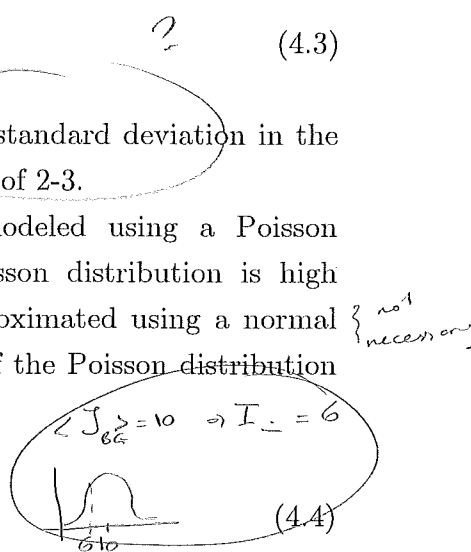
$$I_{Min} = n\sigma_{BG} \quad ? \quad (4.3)$$

in which  $I_{Min}$  represents the value of the threshold,  $\sigma_{BG}$  the standard deviation in the background intensity, and  $n$  often takes a value in the order of 2-3.

Generally, the arrival of background counts is modeled using a Poisson distribution [46]. When the average value of such a Poisson distribution is high enough (say, larger than 10), this distribution can be approximated using a normal distribution with mean and variance equal to the average of the Poisson distribution [47]. This implies that equation (4.3) can be rewritten as

$$I_{Min} = n\sqrt{\langle I_{BG} \rangle} \quad (4.4)$$

with  $\langle I_{BG} \rangle$  representing the average background intensity. A value for  $n$  of 2, for instance, implies that about 2.3% of the pixels will have a background intensity



higher than the threshold value [46]. For a value of 3, this fraction drops to only 0.1%.

The average background intensity is computed by defining two background rings. In this manner, if a dependence of the background intensity on the distance from the beam center exists this should be visible from the data. The first and second background ring are located between the austenite's  $\{200\}$ - and  $\{220\}$ -, and  $\{220\}$ - and  $\{311\}$ -ring, respectively, implying that no diffraction spots are expected within these rings. Therefore, by determining the average intensities of these rings the average background intensity of the dataset can be determined, and hence the threshold criterion of the form of equation (4.4) can be constructed. The value of  $n$  is determined by a trial-and-error type process, in which 2 is taken as the starting value (a value commonly used for these types of criteria) which can subsequently be refined based on the amount of pixels incorrectly identified as peaks.

For numerical results on the background characterization, the reader is referred to chapter 5. For a detailed description of the derivations of the exact threshold criteria for the two datasets, the reader is also referred to the corresponding sections of the appendix.

#### 4.3.4. Criterion – local maximum

Whereas the previous subsection highlighted the criterion of the intensity threshold imposed on each pixel during peak scanning, the current subsection discusses the second criterion employed. This criterion states that the pixel under consideration should form a local intensity maximum with respect to all its nearest neighbors in  $(x, y, \omega)$ -space.

The workings of this criterion are indicated in Figure 4.7. In this figure, the pixel indicated with a cross has been recognized as having an intensity higher than the threshold value. The analysis continues by checking this pixel's intensity against its 8 nearest neighbors within the same diffraction image (recorded at a certain value of  $\omega$ ), as well as against its 9 nearest neighbors in both the preceding and succeeding image in  $\omega$ -space. If the pixel's intensity proves to be a maximum with respect to these 26 other pixels, the pixel is identified as a peak. If this is not the case, then apparently some neighboring pixel displays a higher intensity; these two pixels are most likely part of the same spot. Since each spot should preferably be represented by only a single entry in the list of peaks, the pixel under consideration is not treated as a peak. Instead, it is the nearest neighbor with the higher intensity that is designated as a peak (providing that pixel does constitute a local maximum).

When a pixel has been identified as a peak, several characteristics of that peak can be calculated. These include the distance from the beam center  $R$ , the exact

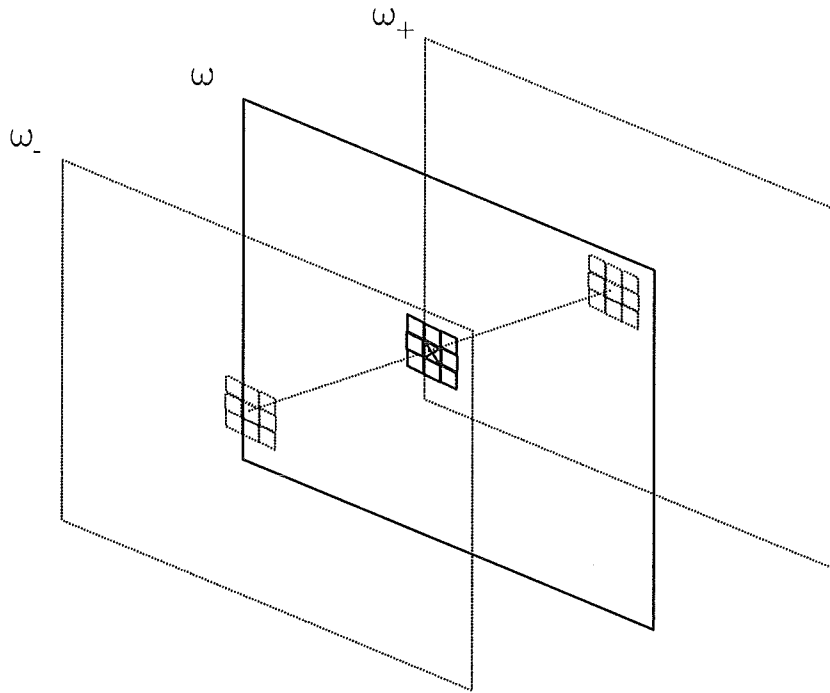


Figure 4.7: Schematic representation of the second criterion used in the peak detection process. The pixel indicated with a cross has an intensity higher than the threshold intensity. It is then checked against the intensities of its 26 neighbors in three-dimensional  $(x,y,\omega)$ -space. When the intensity of the pixel in question is larger than or equal to the intensities of all of those neighbors, it is identified as a peak.

diffraction angle  $2\theta$ , and the azimuthal angle  $\eta$ . Additionally, a first indication of the size of the corresponding diffraction spot is calculated by determining the spot's half-width half-maximum (HWHM) values in all three dimensions. These values indicate at what distance from the peak the intensity has dropped to below half the peak's intensity. In this way, a first estimate of the spot size is obtained.

#### 4.4. Spot characterization

As shown in Figure 4.1, after the peaks have been detected their corresponding spots are characterized. This characterization consists of two main parts: determination of the dimensions of the spot, and subsequent calculation of the spot's characteristics such as  $R$ ,  $2\theta$ ,  $\eta$  and total intensity.

Figure 4.8 shows a flow chart of the routine performing this spot characterization, which requires a single peak as input. The routine starts off by declaring some parameters that mostly depend on the diffraction image in which the peak under consideration is located. When this is done, determination of the spot's dimensions commences. For this, a procedure is used based on three objects: a box

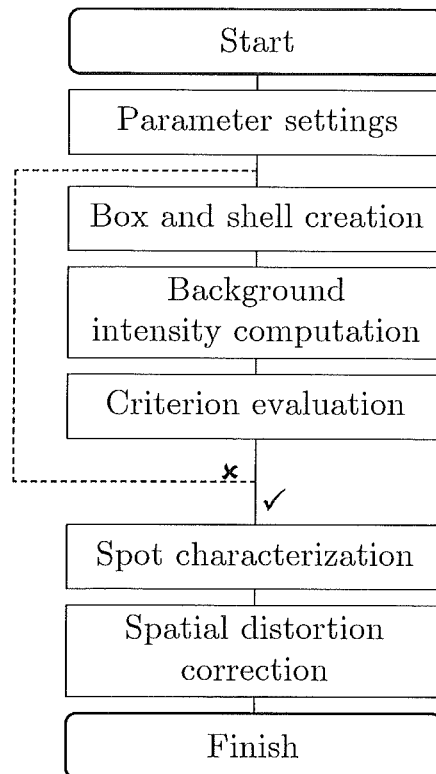


Figure 4.8: Flow chart of the spot characterization process. The routine determines the dimensions of a diffraction spot represented by a previously detected peak, and characterizes it in terms of total corrected intensity and center of gravity detector coordinates. These coordinates are subsequently corrected for the spatial distortion of the image introduced by the setup's optics.

containing the spot under consideration, and two shells that envelop this box. On the basis of these three objects the background intensity can be computed and the two criteria described in the previous section can be evaluated. In case the criteria are fulfilled, the spot's dimensions are accepted. If not, they are refined and the procedure is repeated. For a detailed explanation of this procedure, see the following subsection.

When the routine has arrived at the spot's correct dimensions, it proceeds by characterizing the spot in terms of its center of gravity coordinates on the detector and its total intensity (corrected for the background). Finally, the correction for spatial distortion is applied. For more on this latter subject, see subsection 4.4.2. In case no correct spot dimensions can be determined (for instance because of spot overlap, or because the spot is located too close to the limits of the  $\omega$  scanning range), the routine is ended prematurely and control is passed back to the calling program.

#### 4.4.1. Spot dimension refinement

The first of two main parts of the spot characterization process is concerned with determining the spot's size in all three dimensions  $x$ ,  $y$  and  $\omega$ . As a first estimate of the spot size, the spot's half-width half-maximum (HWHM) values have been determined at the end of the peak detection process. These define a box (the so-called 'peak box') which, in a first approximation, describes the spot's size. Clearly, though, these HWHM values will not always suffice for describing the exact dimensions. Especially the larger spots will usually have considerable tails which need to be taken into account when computing for instance total integrated intensities.

The essence of deciding if the spot dimensions have been set correctly, is determining whether or not the peak box contains all pixels that show an increase in intensity as a result of the diffraction spot. Hence, some criterion is required to determine whether or not the pixels bordering the peak box have an intensity that is higher than expected for pixels that do not belong to a spot, in other words an intensity higher than can reasonably be attributed to the background. As mentioned in subsection 4.3.3, the average background intensity of a pixel will generally vary as a function of location on the detector. More specifically, some radial dependence of the background is expected, complicating matters at hand considerably.

So, the routine needs some way of determining whether the intensity of pixels bordering the peak box could reasonably be attributed to the background or not; however, the average background intensity is not something that can be determined simply by averaging a few pixel readings at some distance from the beam center at which no peaks are expected. Determination of the average background intensity within a diffraction ring is a complicated procedure, as computing this would require knowledge of which pixels within such a ring are part of a peak and which are not, since pixels belonging to a peak should not be included in this averaging procedure. This, in turn, would require prior knowledge of the threshold intensity, which depends on the average background intensity; and this is exactly what we are trying to determine. The only way to directly determine the average background intensity would therefore be some kind of iterative procedure where one would start with a certain value for the average background intensity (for instance the average of all pixels in the diffraction ring, so including those belonging to a peak), determine which pixels belong to peaks and which don't, and use this knowledge to recompute the average background intensity. This new value can then be used for the subsequent iteration. This could be repeated until the computed intensity no longer shows any significant changes. The resulting routine, however, would be complicated and time-consuming.

*why the estimate?*

*why?*



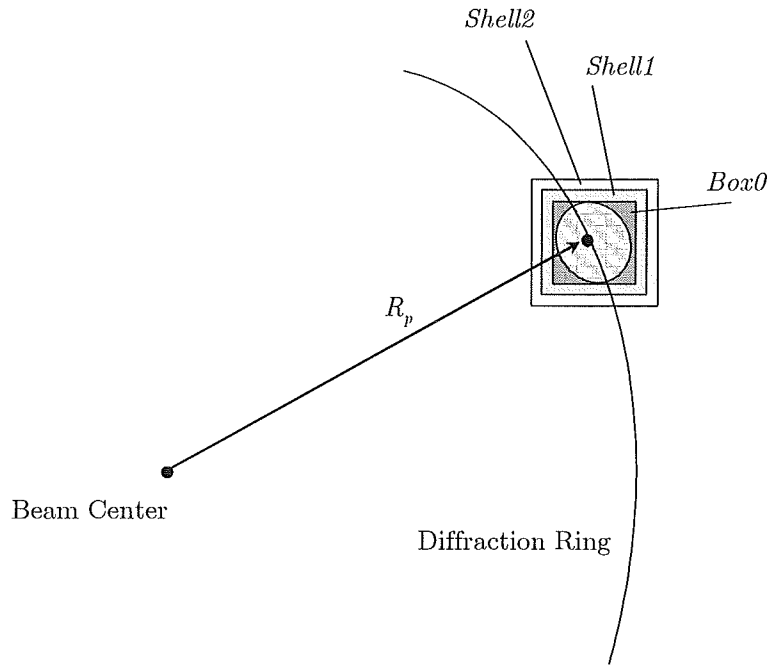


Figure 4.9: Two-dimensional visualization of the definitions of *Shell1* and *Shell2* used in the determination of the correct size of the peak box *Box0* around a peak at a distance  $R_p$  from the beam center. *Shell1* is a shell of a single pixel in width around the peak box *Box0*, whereas *Shell2*, also a single pixel wide, envelops *Shell1*. Note that, although the figure only displays the detector's  $x$  and  $y$  directions, the peak box and the two enveloping shells also extend into  $\omega$ -space.

Instead, a different approach to this problem was designed. This approach was based on work carried out by dr. Enrique Jimenez-Melero of the Reactor Institute Delft. It is built around the definition of two shells: *Shell1*, which strictly envelops the peak box (designated as *Box0*) in all three dimensions, and *Shell2*, which strictly envelops *Shell1*. The situation is visualized in Figure 4.9, albeit only two-dimensionally. The figure depicts a pixel which has been identified as a peak lying at a distance  $R_p$  from the beam center. This peak has HWHM  <sup>$\gamma, \mu, \omega$</sup>  values associated with it. These values are used to construct a box around the peak which serves as a first approximation to the actual peak dimensions. Around this box (*Box0*) two shells are defined. *Shell1* and *Shell2* both have a width of a single pixel, and they strictly envelop the peak box and *Shell1*, respectively. Note that, although the figure only displays a single diffraction pattern and hence only visualizes the procedure in two-dimensional  $(x,y)$ -space, the peak box and surrounding shells also extend into  $\omega$ -space.

1 H11?

As mentioned above, the main difficulty surrounding the determination of the final peak dimensions is the dependence of the non-electronic part of the background intensity on the distance from the beam center  $R$ . Since the pixels within *Box0* do not have a constant distance to the beam center, the non-electronic background

correction they require is not constant either. For each distance to the beam center, a separate average non-electronic background intensity value should be computed, so that each of the peak's pixels can be corrected with the appropriate value.

This is done in the following manner. For all of the pixels in Box0, Shell1 and Shell2, the distance to the beam center (in units of pixels) is computed. These distances are rounded to integer numbers so that a discrete distribution of distances around  $R_p$  is formed. Depending on the dimensions of the peak box (ranging from 2 to 10 pixels HWHM in either direction), Shell2 for instance will typically contain pixels with radial distances varying between  $(R_p-10)$  and  $(R_p+10)$ . Subsequently, for both shells the intensities of pixels that have the same distance to the beam center are averaged. In this way, a list is created for each shell which contains the distances of the pixels within that shell to the beam center and their corresponding average intensities.

The following reasoning is now applied. If Shell1 does not contain any intensity from the spot in Box0, and Shell2 does not contain any intensity from any neighboring spot, then both shells only contain background intensity and therefore the average background intensity of pixels in Shell1 at a certain distance from the beam center should be (approximately) equal to that of pixels in Shell2 at the same distance. So, the average intensity of pixels within Shell1 as a function of distance to beam center,  $\langle I_{sh1}(R) \rangle$ , is compared to the average intensity of pixels within Shell2 at the same distance,  $\langle I_{sh2}(R) \rangle$ . If these are approximately equal for all values of  $R$  that fall within Shell1, then the peak box dimensions are accepted as the final dimensions. Analysis can continue, using the background intensities from Shell1 for the non-electronic background correction of the pixels in Box0. If Shell1 shows significantly higher intensities than Shell2, then Shell1 still contains intensity from the spot in Box0. The peak box dimensions are enlarged by a single pixel in each direction, and the procedure is repeated. If Shell2 contains higher intensities than Shell1, then it appears Shell2 contains intensity from a neighboring spot. The peak box dimensions are reduced by a single pixel in all directions to try and exclude this influence, and the procedure is repeated. In this way, the peak box size is refined until the correct dimensions have been obtained.

The criterion used for determining whether or not  $\langle I_{sh1}(R) \rangle$  and  $\langle I_{sh2}(R) \rangle$  are 'approximately equal' is based on the normal approximation to the Poisson distribution, and follows a reasoning similar to that of the intensity threshold criterion outlined in subsection 4.3.3. Assuming again that the background counts follow a Poisson distribution, the background of a pixel at a certain distance  $R$  from the beam center can be approximated by a normal distribution with mean and variance equal to the background intensity's average. Remember, however, that the

*R*

*or rejected!*

intensities of Shell1 and Shell2 are actually averages of multiple pixels that all lie at distance  $R$ . Averaging  $N$  observations from the same distribution has the effect of reducing the variance in the average by a factor of  $N$  as compared to the variance of a single observation. So, if Shell1 contains  $N_1$  pixels at a distance  $R$  from the beam center, then the variance  $(\sigma_{sh1})^2$  in the average background intensity in Shell1 at  $R$  can be approximated by:

$$(\sigma_{sh1})^2 \simeq \frac{\langle I_{sh1}(R) \rangle}{N_1} \quad (4.5)$$

A similar expression can be written for the variance in the background intensity in Shell2 at a distance  $R$  from the beam center. By comparing the actual difference between the average intensities in the two shells,  $\langle I_{sh1}(R) \rangle - \langle I_{sh2}(R) \rangle$ , to the sum of their standard deviations, one can now determine whether or not the two differ significantly. The criterion for determining whether the peak box dimensions have been set correctly then becomes of the form:

$$|\langle I_{sh1}(R) \rangle - \langle I_{sh2}(R) \rangle| < \sqrt{\frac{\langle I_{sh1}(R) \rangle}{N_1}} + \sqrt{\frac{\langle I_{sh2}(R) \rangle}{N_2}} \quad (4.6)$$

1  $\sigma$

in which the left-hand side of the criterion represents the absolute difference between the two experimentally observed average intensities, and the right-hand side represents the sum of the standard deviations of the distributions of the average intensities in the two shells at distance  $R$ . Shell1 and Shell2 contain  $N_1$  and  $N_2$  pixels with this specific distance to the beam center, respectively. If the criterion is not met, and  $\langle I_{sh1}(R) \rangle$  is larger than  $\langle I_{sh2}(R) \rangle$ , then Shell1 contains intensity from the spot in Box0. If the criterion is not satisfied but  $\langle I_{sh2}(R) \rangle$  is larger than  $\langle I_{sh1}(R) \rangle$ , then Shell2 contains intensity from a neighboring spot. In both cases, the dimensions are refined, and the procedure is repeated.

In case the criterion is fulfilled for all values of  $R$  that lie within the peak box, then the peak box dimensions are adequate and analysis continues. Firstly, the spot's total intensity is calculated. This calculation includes correcting for the background intensity. As mentioned above, this is done by subtracting from each pixel in the spot the average background intensity of the spots in Shell1 lying at the same distance to the beam center. In this way, the radial dependence of the background intensity is taken into account. The corrected intensities of the individual pixels are subsequently used as weighing factors during the determination of the center of gravity coordinates of the spot on the detector. Finally, these coordinates are corrected for their spatial distortion.

#### 4.4.2. Spatial distortion correction

The spatial distortion introduced into the diffraction images can lead to significant deviations of the observed coordinates of the diffraction spots. This, in turn, will lead to errors in for instance  $\eta$ , which eventually manifest themselves as errors in the computed crystallographic orientation of the diffracting grain. To prevent this, a correction for the spatial distortion is required. This correction can be applied using the MATLAB routines written to perform the FIT2D spatial distortion correction as described in subsection 4.2.1. A word on the timing of this distortion correction is required here, though.

As mentioned in subsection 4.2.1, the spatial distortion is modeled using two bivariate splines of the third degree in both dimensions. This implies that the function describing the spatial distortion as a function of a pixel's location on the detector is not linear, and the corrected average location of a specific spot will not be the same as the average corrected location of that spot:

$$\begin{aligned} f_m(\langle m \rangle, \langle n \rangle) &\neq \langle f_m(m, n) \rangle \\ f_n(\langle m \rangle, \langle n \rangle) &\neq \langle f_n(m, n) \rangle \end{aligned} \tag{4.7}$$

Here,  $f_m(m, n)$  and  $f_n(m, n)$  represent the spline function for the distortion of a pixel  $(m, n)$  in FIT2D's y and x direction, respectively. The angle brackets represent weighted averages over all pixels within a specific diffraction spot.

Because of this non-linearity of the spatial distortion spline functions, strictly speaking the spatial distortion correction should be applied to all pixels before the start of the analysis. In this way, the peak search commences on the corrected images, and the distortion effects have been cancelled before they can even play a role in the process. However, this procedure increases the computational load. Furthermore, it complicates the subsequent analysis because the grid points are no longer evenly spaced in the  $(x, y)$ -plane of the detector. Therefore, it would be beneficial if it were acceptable to apply the spatial distortion correction at a later stage of the analysis. To analyze the error introduced by such a delayed application of the spatial distortion, a single spot was chosen and analyzed using three separate scenarios:

- A| First correct all pixels for their spatial distortion. Then start the analysis: search for peaks, determine the correct peak box size, and compute the location of the spot's center of gravity.

- B| Perform the peak search, and determine the correct peak box dimensions. Correct all pixels within the box for their spatial distortion, and then compute the spot's center of gravity.
- C| Perform the peak search, determine the peak box dimensions, and compute the center of gravity. Correct this center of gravity location using the spatial distortion splines.

Strictly speaking, scenario A is the correct way of applying the spatial distortion. Scenario B locates the peaks using the uncorrected pixel locations, and refines the peak box sizes using distorted HWHM values. This could influence the final peak box dimensions determined by the routine. Scenario C first reduces the spot to a single pair of center of gravity-coordinates, and applies the correction only to these two coordinates. Clearly this reduces computational load, but the accuracy of the resulting center of gravity coordinates of the peak might suffer considerably.

The spot chosen to be analyzed using these three separate scenarios was required to have two important characteristics. Firstly, it was required to be a large spot. This will generally enlarge the differences between the outcomes of the three scenarios. Secondly, the spot was required to be located in the outer ring under consideration in this project, the  $\{220\}$ -ring. As mentioned earlier, the general trend of the spatial distortion is to increase with increasing distance from the detector's center. Therefore, by picking a peak in the outer ring the influence of the distortion is likely to be largest, highlighting the differences between the three scenarios even more.

The specific diffraction image in which the pixel was to be found was chosen at random. However, a choice was made *a priori* for a peak in the *e*-series, since the illuminated volume during these measurements was three times as high as during the *d*-series, and therefore larger spots are expected. In this case, the image chosen was file number 4e1711, corresponding to the settings stripe 0, layer 18, and  $\omega = -27^\circ$ . Within this image, a visual search for a suitable spot was conducted. Eventually, a spot around pixel (868,383) was chosen. This spot was located in the outer ring, and was one of the larger spots with estimated HWHM values of 10 pixels in both detector dimensions. The spot was subsequently analyzed using the three scenarios as listed above. The results are listed in Table 4.1.

The table shows that the differences between the results of the peak analysis following the three scenarios are only minor. A minute deviation in the horizontal location of the spot's center of gravity is recorded, as well as a small increase in total integrated spot intensity (about 3.5%). Since these results have been obtained for a large spot in the outermost diffraction ring that is considered in this project, the

difference between the results of scenarios A and C can be regarded as a type of upper limit. It is not likely that the effect of postponing the spatial distortion correction will be much larger for any of the other spots. Therefore, it was deemed acceptable to apply the spatial distortion correction after computation of the spot's center of gravity coordinates.

Table 4.1: Results of the analysis of the spot around pixel (868,383) of file 4e1711 using the three different scenarios as listed on page 52. It can be seen that the influence of postponing the spatial distortion correction only has a minor effect on the spot's computed center of gravity coordinates on the detector,  $(m_{CoG}, n_{CoG})$ , and in  $\omega$ -space ( $\omega_{CoG}$ ), as well as on the spot's total integrated intensity.

	$\omega_{CoG}$ ( $^{\circ}$ )	$m_{CoG}$	$n_{CoG}$	Total intensity (# counts)
Scenario A	-27.01	862.91	369.61	$141 \times 10^3$
Scenario B	-27.03	863.00	369.61	$146 \times 10^3$
Scenario C	-27.03	863.00	369.61	$146 \times 10^3$

## 4.5. Spot grouping

The result of the spot characterization procedure is a list of all spots found within the diffraction images in the dataset of interest. These spots have associated characteristics such as their center of gravity coordinates and their total intensity corrected for background contributions. However, these individual spots do not necessarily constitute complete reflections. After all, due to the overlap between subsequent slit positions a single reflecting grain is likely to produce intensity at multiple, neighboring slit settings. For an accurate determination of the scattering vector as well as of the total diffracted intensity of such a reflection, those spots have to be grouped together.

Figure 4.10 presents a flow chart of the spot grouping process. The settings declared at the start of the routine are mainly related to defining the list of spots to be used in the rest of the analysis. When this list has been defined, the first spot is taken. A search is conducted for other spots in the list that might belong to the same reflection as the spot under consideration. Those spots are subsequently grouped and numbered as individual reflections. For each reflection, the center of mass

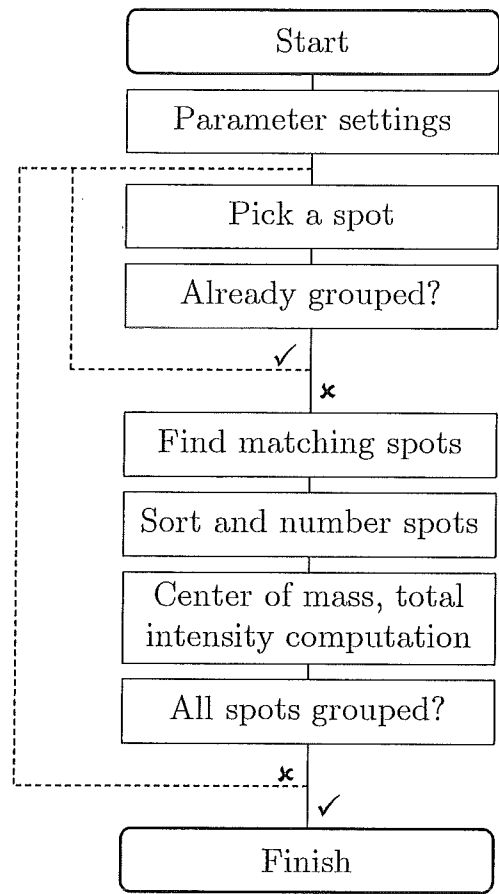


Figure 4.10: Flow chart of the spot grouping process. The routine finds spots that are likely to be part of a single specific reflection, and groups and numbers these spots. Subsequently, the center of mass and total intensity profile of the resulting reflection are computed.

coordinates<sup>2</sup> and the total integrated intensity are computed. Furthermore, the profile of reflected intensity versus illuminated volume can be reconstructed, providing a first indication of the grain's shape. When all spots in the list have been analyzed, the process is finished and provides a list of complete, individual reflections as its output.

4.5.1. Matching of spots

Reconstructing the complete reflections from the individual spots starts by matching those spots that originate from one and the same reflection. Those spots that are indeed fragments of one single reflection should be located at the same  $\omega$ -value and on approximately the same location on the detector. The latter is tested by

?  
2/c p.18  
D/F

<sup>2</sup> When referring to reflections, use is made of the term 'center of mass'. For spots, however, the term 'center of gravity' is employed. Though the two are often used interchangeably, in this case they are used separately to avoid confusion between the variables they represent.

} vrea

demanding that the center of gravity coordinates of the two spots are within a certain distance from each other (typically around 5 pixels in the horizontal and vertical direction). In case such a group of spots is found, however, they should also have been recorded under successive slit settings. After all, when a grain fulfilling the diffraction criterion is translated into and out of the beam, for each slit setting a different part of the grain will be illuminated and produce a diffraction spot. Since subsequent slit settings border on each other (and even overlap), spots from different parts of the same grain will show up in succeeding diffraction images. The current subsection explains how this criterion is imposed.

Figure 4.11 displays the use of the 'connectivity' properties of a group of spots in determining whether the spots originated from a single reflection or not. Connectivity refers to whether or not the spots form a connected group in  $(\text{stripe}, \text{layer})$ -space. The values of *stripe* and *layer* refer to the slit settings used for recording the image containing the spots, and therefore to the illuminated sample volume. In case multiple spots all originated from one and the same reflection, then the illuminated volumes producing those diffraction spots must have formed a single connected volume: the reflecting grain. It follows that the spots must also form a single connected region – in  $(\text{stripe}, \text{layer})$ -space.

Figure 4.11 displays scenarios for various types of spot group composition. Black circles denote recorded spots, whereas white ones denote the absence of a spot. A| depicts the most straightforward case. As a grain is translated into the beam, subsequent subvolumes of the grain produce diffraction spots at subsequent slit

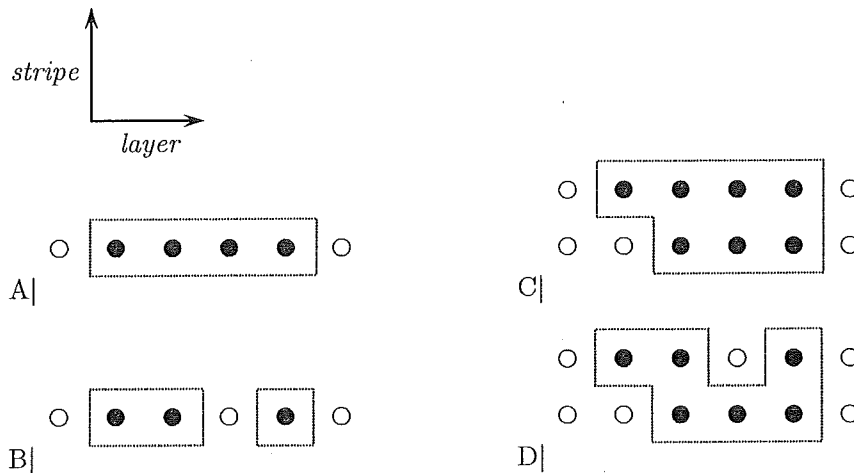


Figure 4.11: Schematic illustration of the connectivity properties of a group of spots, showing the presence (black) or absence (white) of spots at a specific location on the detector for a specific  $\omega$ -value as a function of the illuminated part of the sample in terms of *stripe* and *layer*. Connected spots are treated as belonging to the same reflection (A, C). Absent spots can result in the identification of two reflections (B). However, spots in neighboring stripes can also provide connectivity (D).



settings. When the grain has been translated out of the beam again, no more spots appear. The spots are recognized as belonging to a single reflection. C| shows a comparable scenario, however in this case the spots are located in more than one stripe.

B| displays a scenario where one of the expected spots has not been detected. In this case, the spots no longer form a connected group. Instead, they are divided into two groups, and from there on each group is treated as an individual reflection. For large grains in a randomly oriented microstructure, however, the probability of several spots being located at the same value of  $\omega$  and on the same location on the detector but not coming from the same reflection is quite small. In such cases, it might be more likely that the spot is missing because of an unexpectedly high background intensity in that image, or because of some other anomaly. To allow for this possibility, the two individual reflections identified in scenario B| are flagged so that at a later stage the two can still be combined in case other indications are found that the two should in fact form a single group.

Scenario D|, finally, depicts how when spots are found in multiple stripes connectivity can be obtained in different ways. The spots found in the upper stripe appear to come from two individual reflections. However, the spots in the lower stripe 'bridge' the missing spot, and so the spots are still treated as coming from one and the same reflection. A possible explanation for the missing spot, apart from anomalous background perturbations, is that the reflecting grain had an irregular shape, implying that for the slit setting corresponding to the missing spot no part of the grain happened to be illuminated.

By inspecting the connectivity properties of individual spots, the spots are grouped into reflections. The next step consists of taking such a reflection and reconstructing its profile of intensity versus illuminated volume. Furthermore, the reflection's center of mass coordinates are computed.

#### 4.5.2. Intensity profile and center of mass computation

One of the main characteristics to be computed for each individual reflection is the reflection's total integrated intensity. After all, a reflection's intensity scales directly with the volume of the grain producing the reflection; see equation (3.10). However, since considerable overlap exists between any two neighboring slit settings, the calculation of this total intensity is somewhat more complicated than a simple summing of the intensities of the individual spots. The experimentally recorded intensities should be corrected for the overlap in slit position to arrive at a reliable number for the reflection's total integrated intensity.

The slit position overlap leads to an increase in the resolution with which the profile of intensity versus illuminated volume can be constructed. Without slit overlap, the resolution would simply be the beam width:  $15\text{ }\mu\text{m}$ . Due to the overlap, however, this value drops to as low as  $2.5\text{ }\mu\text{m}$ . This concept is illustrated in Figure 4.12. It depicts how the slit overlap results in an increased resolution and how the intensity profile can be deconvoluted using this overlap. The figure shows multiple layers ( $n$  through  $n+5$ ). As highlighted in subsection 3.1.2.1, the shift between two successive layers is less than the layer width ( $b_{beam}$ ). So, the intensity recorded for layer  $n+1$ , for instance, will contain a lot of intensity that was also recorded in layer  $n$ . To correct for this double counting of intensities, the volume from where the reflection originated is divided into smaller parts. This division is dictated by the layer overlap. Since the layer overlap is not constant but is either  $10$  or  $7.5\text{ }\mu\text{m}$  (see subsection 3.1.2.1), the subvolumes are of differing length as well. The figure indicates the typical periodicity of the sizes of the subvolumes (A-F); most of them are  $2.5\text{ }\mu\text{m}$  in width, but every fifth volume has a width of  $5\text{ }\mu\text{m}$ . The intensity originating from a specific subvolume can now be calculated as a weighted average of fractions of the spot intensities that originate (partly) from the subvolume in question. For instance, the intensity coming from volume A,  $I_A$ , can be computed as an average of parts of the intensities  $I_n$ ,  $I_{n+1}$  and  $I_{n+2}$ :

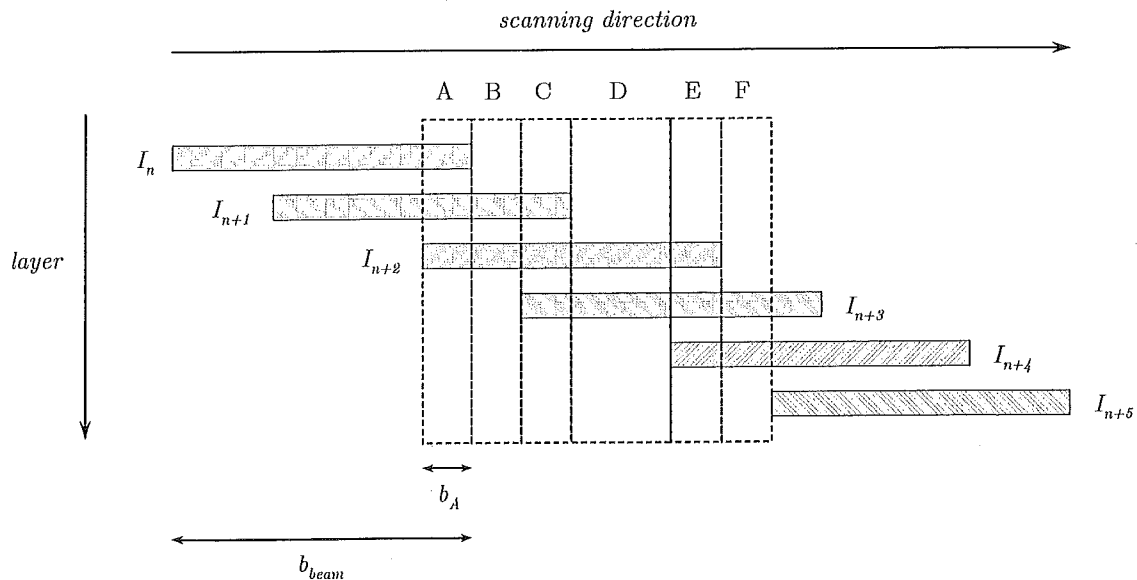


Figure 4.12: Schematic illustration of the reconstruction of an intensity profile from its component intensities using the layer overlap. The image shows subsequent layers overlapping in the scanning direction; for reasons of clarity they have been separated from each other vertically in the figure. The overlap creates an increased resolution in the scanning direction, allowing the intensity coming from for instance subvolume A to be computed as a weighted average of fractions of  $I_n$ ,  $I_{n+1}$  and  $I_{n+2}$ .

$$I_A = \frac{1}{3} \frac{b_A}{b_{beam}} (I_n + I_{n+1} + I_{n+2}) \quad (4.8)$$

Each intensity is weighed using the fraction of the corresponding layer located within A, after which the average is computed. Layers  $n$ ,  $n+1$  and  $n+2$  all cover volume A, so the averaging is carried out over the three corresponding intensities. Expressions similar to (4.8) can be constructed for the intensities of the other subvolumes. The result is a profile of intensity versus illuminated sample volume with a resolution of  $2.5 \mu\text{m}$  (except for every fifth point, which has a resolution of only  $5 \mu\text{m}$ ).

When this intensity profile has been reconstructed, the reflection can be characterized in terms of total intensity as well as center of mass coordinates. Summing of all components of the intensity profile produces the reflection's total intensity and therefore a measure of the reflecting grain's volume. Furthermore, the intensity profile can be used to compute with improved accuracy the center of mass coordinate of the reflecting grain within the sample. From the coordinates of the individual spots making up the reflection, an average spot location on the detector can be determined. These coordinates describe the reflection's scattering vector, and hence eventually the grain's crystallographic orientation. The link between scattering vector and crystallographic orientation is established in the next part of the analysis.

## 4.6. Reflection coupling

Each illuminated grain will produce reflections at multiple values of  $\omega$ . The positions of these reflections in terms of location on the detector and  $\omega$ -value are determined by the crystallographic characteristics of the grain in question. Therefore, by scanning for groups of reflections that match the crystallographic criteria imposed by the material, reflections originating from the same grain can be grouped together. Furthermore, from as little as two independent reflections the grain's crystallographic orientation can be derived (in case the lattice parameters are unknown: three reflections) [48]. The linking of individual reflections coming from the same grain, known as 'indexing', is therefore a crucial step in the microstructure reconstruction.

Theoretically, there are three different criteria based on which one could index the individual reflections: the calculated coordinates of the diffracting volume, the crystallographic characteristics of the material, and the total integrated intensities of the reflections [32]. Of these three, the latter is the least reliable. An important reason for this is the complications that arise with grains lying near the boundaries of the illuminated volume. When the sample is rotated about  $\omega$ , such grains will oscillate in and out of the illuminated area. This can lead to these grains being only partly illuminated during diffraction, resulting in significantly lower intensities as compared to diffraction when these grains are fully illuminated. Indexing based on

total intensity would not be able to deal with such complications. The criterion based on the calculated coordinates of the diffraction origin, on the other hand, is only applicable when the uncertainty with which these coordinates are determined is much smaller than the grain dimensions. The criterion most generally applicable is that of the crystallography of the material. This is the indexing criterion used in this project.

Indexing is carried out by means of an alpha version of a program called GrainSpotter [49]. GrainSpotter, developed by dr. Søren Schmidt of Risø National Laboratory in Denmark, is based on earlier software called GRAINDEX [32]. GRAINDEX is a program designed for the image processing and indexing of 3DXRD data; GrainSpotter is a stand-alone program performing only the latter of the two. It indexes the reflections by a stepwise scanning of Euler space. GrainSpotter calculates expected diffraction vectors as a function of the simulated crystallographic orientation of a diffracting grain, and checks whether or not these vectors have been recorded. Grains are identified on the basis of two criteria: completeness and uniqueness. The completeness criterion states that the number of reflections found for a certain assumed crystallographic orientation,  $M_{exp}$ , should not be much smaller than the theoretically expected number of reflections for that orientation,  $M_0$ . This is quantified through the following expression:

$$M_{exp} \geq (1 - \alpha_c) M_0 \quad (4.9)$$

*what are reasons for  $\alpha_c > 0$ ?*

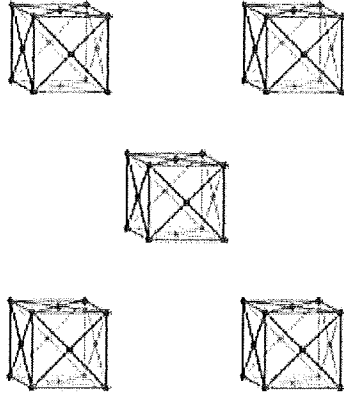
in which  $\alpha_c$  is a dimensionless parameter determining the stringency of the criterion. The uniqueness criterion dictates that the set of matching reflections is not allowed to be a subset of the set of matching reflections for another simulated orientation.

When both criteria are met, the group of reflections is assigned to a grain with a crystallographic orientation as simulated. If no group of reflections can be constructed that fulfills the completeness and uniqueness criteria, it is inferred that no grain is present with the orientation under consideration. For a more detailed description of the indexing procedure, the reader is referred to [29, 32] or to the appendix to this report.

## 4.7. Grain characterization

The output from GrainSpotter is a list of groups of reflections which originate from the same grain. The final step in the microstructure reconstruction is to use these reflection groups to calculate the characteristics of interest of the corresponding grains. These characteristics include the crystallographic orientation of the grain and the location of its center of mass within the sample.

Although GrainSpotter is quite useful for the process of matching the individual reflections, the output it provides is limited. For instance, although it does compute the grains' orientation matrices, it does not provide the possibility of determining the center of mass locations of the reflecting grains. The appendix to this report contains a routine which uses GrainSpotter's output file and relinks it to the list of reflections already used as GrainSpotter's input. This allows for the retrieval of more of the grains' characteristics. The routines for the actual characterization itself have not yet been created. This is related to the fact that with the current datasets and alpha version of GrainSpotter, no accurate results could be obtained to implement this type of software. These issues are treated further in the next chapter.



## 5. Results – microstructure reconstruction

The previous chapter has presented the software package created during this project. This package was subsequently tested on datasets *d* and *e* of the experiment described in subsection 3.1.2. The current chapter contains the results of these tests.

### 5.1. General characteristics

This section lists some of the general characteristics of datasets *d* and *e*. Apart from providing the reader with information on the accuracy with which the experiment was performed, this also creates a picture of the size of the datasets and hence of the complexities associated with the computational analysis of the data.

Figure 5.1 displays the location of the volume that was analyzed during this project in relation to the dimensions of the entire sample. The middle of the gauge volume is indicated by the black dot. In the setup's *y*-direction, the center of the gauge volume coincided with the rotation axis; so, in this direction the gauge volume was located in the exact middle of the sample. In the *z*-direction, the gauge volume was displaced slightly with respect to the sample's middle. With a total sample height of 4 mm., the middle of the gauge volume was located 1.5 mm. below the top surface of the sample. Given the gauge volume dimensions of  $309 \times 300 \mu\text{m}^2$  and  $300 \times 309 \mu\text{m}^2$  (width  $\times$  height) for the *d*- and *e*-series, respectively, edge effects from the top or bottom surface are not expected to have had any significant influence on the results of the analysis.

Table 5.1 contains various characteristics of the *4d* and *4e* datasets. The large difference in total recording time for the two sets of data has two main causes. First of all, the amount of files in the *e*-dataset is only a third of that in the *d*-set. The reason for this is the difference in experimental setup: the *d*-dataset was recorded using three horizontal stripes, whereas the *e*-measurement only required a single,

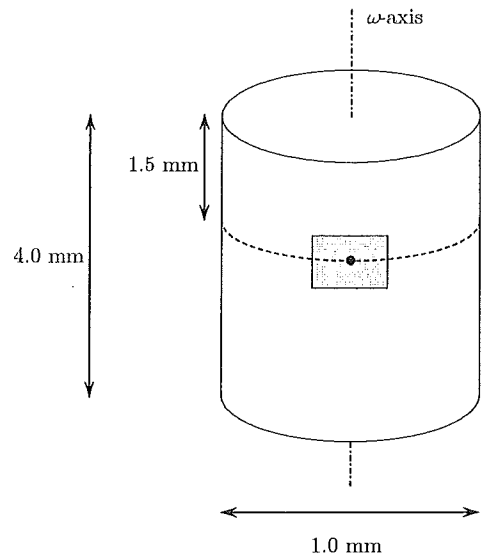


Figure 5.1: Location of the center of volume analyzed in this project, indicated by the black dot, in relation to the sample dimensions. In the y-direction, the middle of the gauge volume coincided with the  $\omega$  rotation axis. In the z-direction, the volume was translated slightly with respect to the middle of the sample, but given the gauge volume dimensions of about  $300 \times 300 \mu\text{m}^2$  no edge effects from the top or bottom surface were expected. For definitions of directions, see Figure 3.1.

vertical stripe. The second reason for the difference in recording time stems from the different exposure times used for the two datasets. Set  $d$  was recorded using an exposure time of 1 second, whereas  $e$  used an exposure time of only 0.5 second.

The table also contains the values of the averages and standard deviations of the temperatures during the two experiments,  $\mu_T$  and  $\sigma_T$  respectively. As illustrated earlier (see Figure 3.4), the desired temperature during both experiments was 1000 °C. This temperature was achieved in both cases, with only minor deviations occurring over the course of the measurements. In fact, the largest recorded temperature deviation from the ideal temperature during these experiments was only 0.22 °C.

Table 5.1: Some general characteristics of datasets  $4d$  and  $4e$  analyzed during this project. The large difference in total recording time is caused by the amount of  $d$ -files being three times as large as well as by the smaller exposure time of the  $e$ -measurement. The temperatures lay at the desired level of 1000 °C for both datasets ( $\mu_T$ ), with very small standard deviations over the entire experiment ( $\sigma_T$ ).

	Recording time (hh:mm:ss)	# files	$\mu_T$ (°C)	$\sigma_T$ (°C)
$4d$	10:27:55	13799	1000.00	0.07
$4e$	02:14:01	4600	1000.00	0.08

## 5.2. Pre-analysis

This section presents the reader with the results of the various calculations carried out before start of the actual analysis. This includes the reconstruction of the spatial distortion of the diffraction images, characterization of the dark current intensities, determination of the location of the beam center, determination of the amount and direction of the detector tilt, and determination of the sample-detector distance.

### 5.2.1. Spatial distortion reconstruction

The first operation carried out during the pre-analysis phase was the characterization of the spatial distortion of the diffraction images introduced by the experimental setup. As set out in section 4.2.1, the routines based on the FIT2D algorithm describe the spatial distortion using two third-degree bivariate splines, one for the  $x$ - and one for the  $y$ -direction of the FIT2D coordinate system. The results of the distortion characterization are given in Figure 5.2.

Images A| and B| depict the uncorrected and corrected distortion characterization images, respectively. In image A|, the spatial distortion manifests itself through the deviation from the horizontal (vertical) of the rows (columns) of images of the holes in the mask. After application of the correction using the spline functions, the holes lie in (near-)perfect rows and columns again, indicating that the distortion has been neutralized. Images C| and D| depict contour plots of the required corrections of the pixel locations in the vertical and horizontal direction, respectively. The required vertical corrections vary from about +6 pixels (in the center of the lower left quadrant) to -34 pixels (in the bottom right corner). The plot providing the horizontal corrections displays values ranging from +2 pixels (upper right quadrant) to -34 pixels (bottom right corner). The dashed lines in C| and D| indicate the middle of the detector in both dimensions. Furthermore, the black dots indicate the location of the beam center. This location was determined by means of the procedure outlined in subsection 4.2.3; for the results of this determination, see later on in this chapter (subsection 5.2.3). It can be seen that the corrected beam center location varied about 0.5 pixels in either dimension with respect to the distorted coordinates. To be precise, where the coordinates representing the distorted beam center were (1038,981), the corrected values were (1038.52,981.37).

### 5.2.2. Dark current characterization

After the spatial distortion reconstruction, the characterization of the dark current intensities was performed. Insight into these intensities was required so as to be able



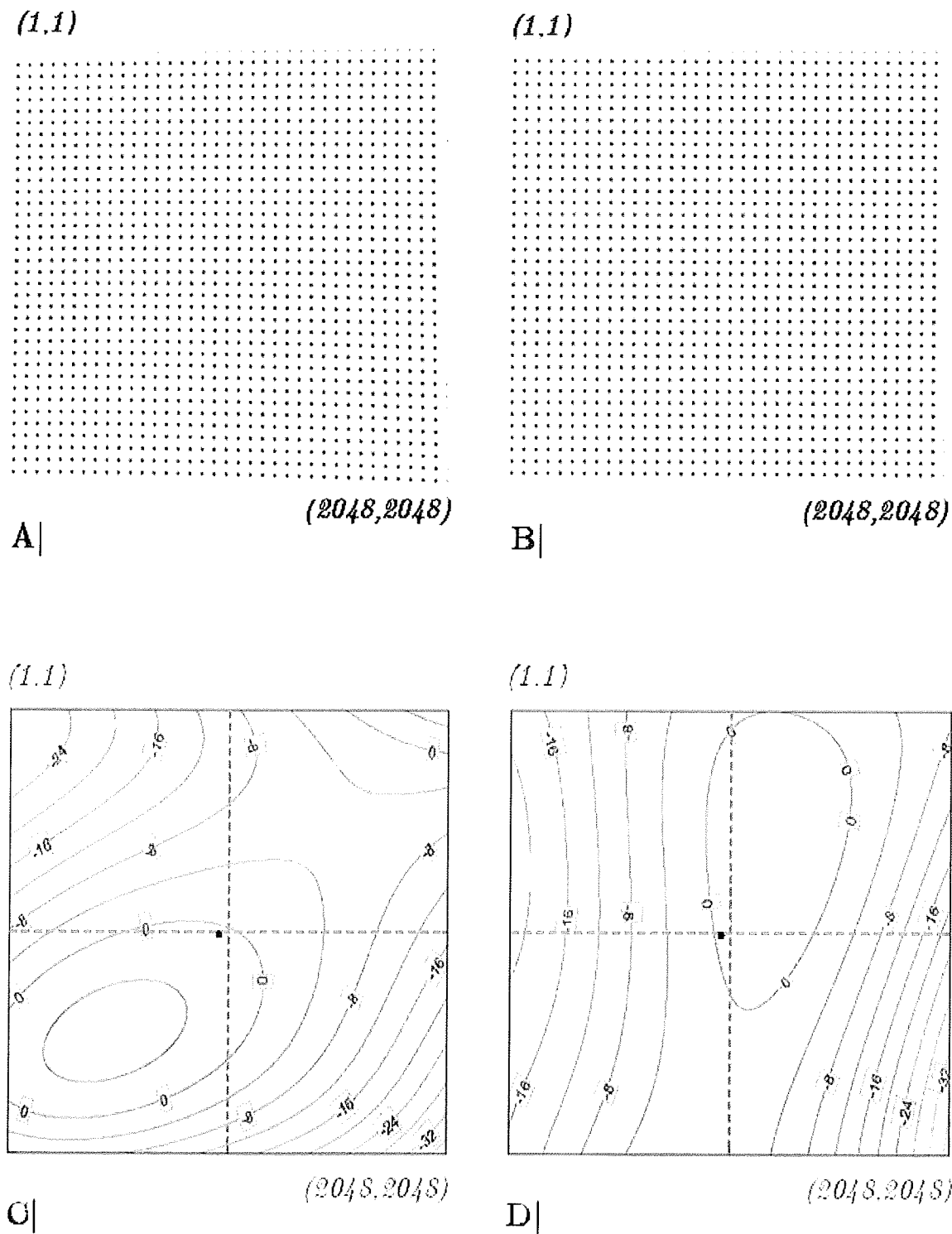


Figure 5.2: Visualization of the spatial distortion introduced by the experimental setup. A| shows the characterization image as described in subsection 4.2.1; B| displays the corrected version of this image using the two bivariate splines. C| and D| show contour plots of the required corrections in the vertical and horizontal direction, respectively. The dashed lines indicate the middle of the detector; the dot represents the beam center location (see subsection 5.2.3).

to carry out an accurate beam center determination procedure (see subsequent subsection). Figure 5.3 presents the results hereof.

The figure shows the average dark current intensities  $\langle I_{DC} \rangle$  of a pixel in a specific row or column, both for the dark current images used for set  $d$  (part A|) and for set  $e$  (part B|). The values are nearly constant at a level of 1000 counts. Small discontinuities can be witnessed at the horizontal and vertical middles of the detector; this effect was already observed visually in the  $\text{LaB}_6$  diffraction pattern (see Figure 4.3). However, the vertical scale clearly shows that these discontinuities are only in the order of a few counts, and therefore play a minor role. The plots of

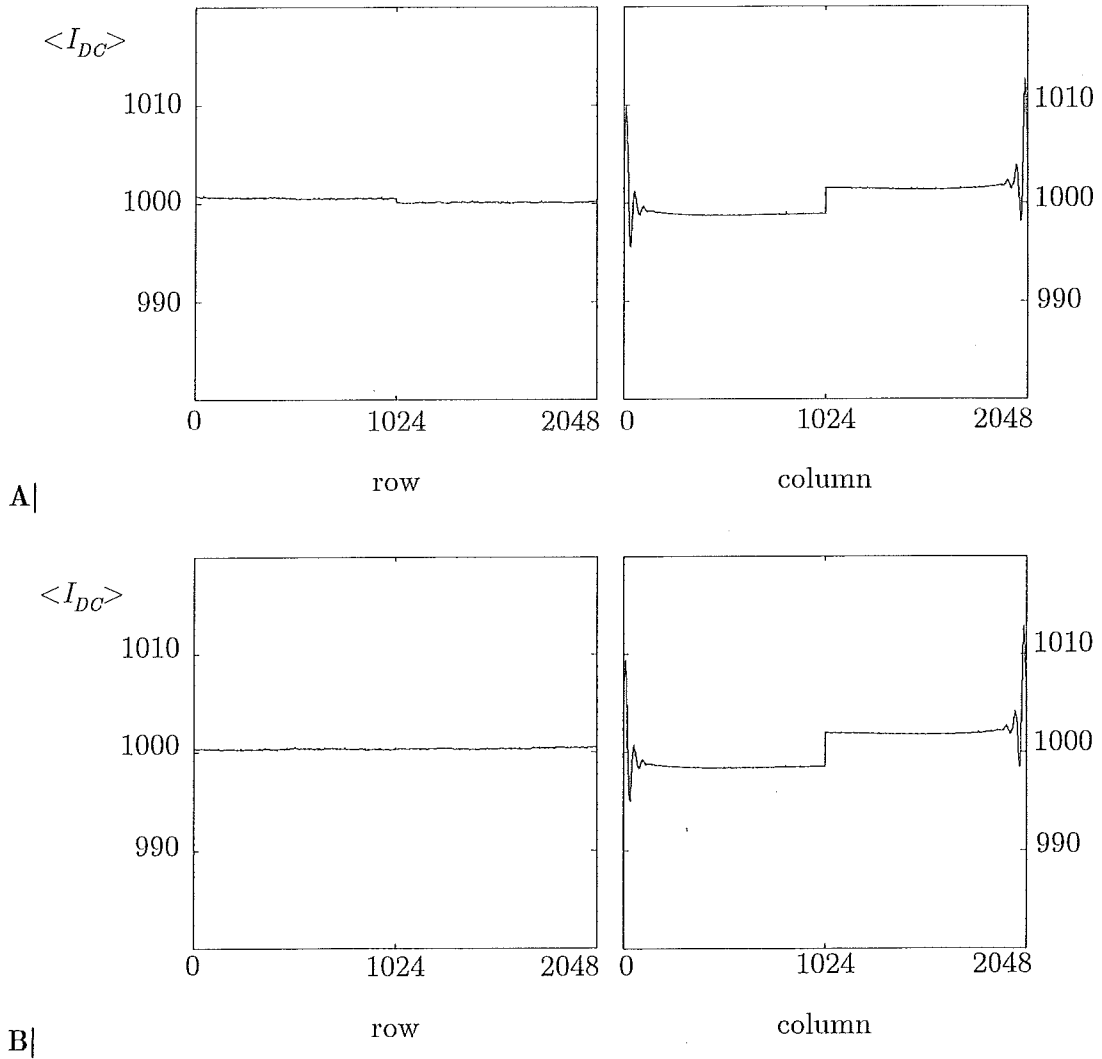


Figure 5.3: Average dark current intensity per pixel  $\langle I_{DC} \rangle$  as a function of its row and column coordinate for sets  $d$  (A) and  $e$  (B). The values are an average of all 2048 pixels in each row/column and of all 22 diffraction patterns with the appropriate exposure time. Note the changes in average intensity on crossing the middle of the detector. The irregularities in the intensities of the outer columns on either side are edge effects that are of no importance to the analysis in this project.

average intensity versus column coordinate display more sizeable discontinuities near the edges of the detector. Though these fluctuations are more significant than the small discontinuity in the detector middle, in this project they can be neglected since these columns do not lie within the area of interest of the detector.

### 5.2.3. Beam center determination

The procedure used for locating the beam center on the detector was described in subsection 4.2.3. Using the direct beam mark found in the  $\text{LaB}_6$  diffraction image as a first indication, the exact coordinates are determined using a weighing of the pixel coordinates in and around the beam mark with the corresponding intensities as weights. Figure 5.4 shows plots of the average intensity per pixel around the direct beam mark as a function of row and column coordinate. The graphs show a clear increase in intensity in the vicinity of the direct beam mark. The direct beam mark appeared to be no larger than about 8 by 8 pixels, agreeing with the visual indications from Figure 4.3. The errors in the values are indicated using error bars. Note that the errors in the average intensity per row are smaller than those in the intensity per column. This is caused by the fact that the latter was averaged over a smaller number of pixels (this is directly related to the dimensions of the peak box; for detailed treatments hereof, the reader is referred to the corresponding section in

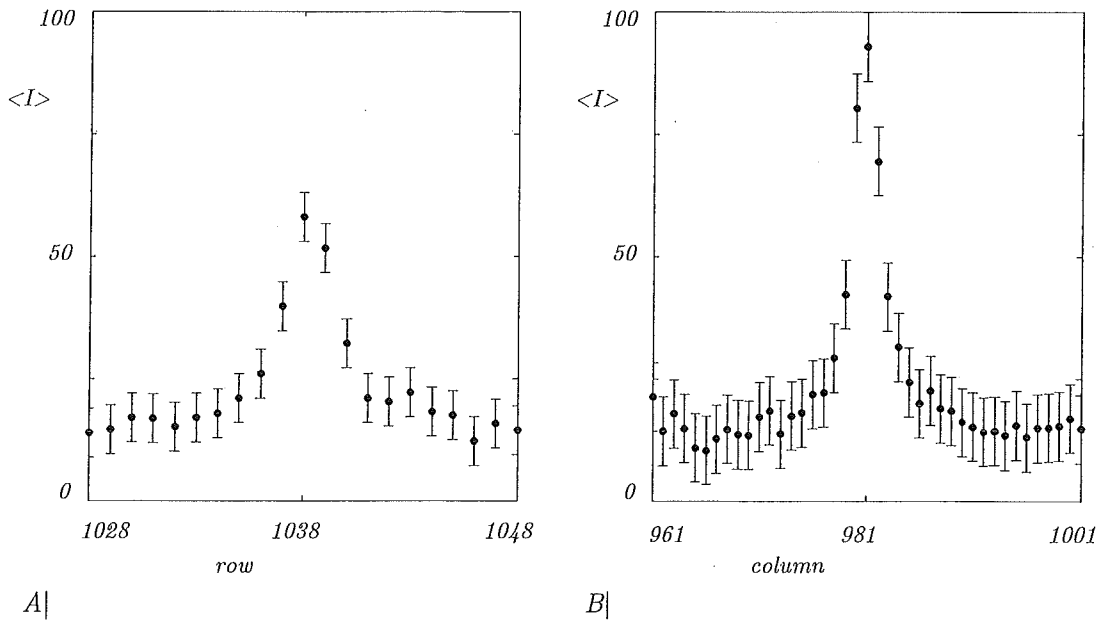


Figure 5.4: Plots of the average intensities  $\langle I \rangle$  per pixel, corrected for dark current intensity, as a function of row coordinate (A) and column coordinate (B) in and around the direct beam mark located at pixel (1038,981). Both show clear increases in intensity in the direct vicinity of the beam mark.

the appendix to this report).

Figure 5.4 indicates that the mark detected on visual inspection did indeed correspond to a significant increase in intensity. This first indication of the beam center was refined using the afore-mentioned routine. The results are listed in Table 5.2.

As mentioned in section 4.2.3, the coordinates of the pixel with the highest intensity within the direct beam mark were used as the first estimate of the beam center location. This pixel was located at (981,1011), expressed in FIT2D-coordinates. This corresponds to entry (1038,981) when the diffraction image is read in as a matrix. Table 5.2 shows that refining the beam center coordinates using the weighing procedure did not change location of the beam center significantly; the center of the beam mark still coincided with the pixel with the highest intensity. Therefore, from here on this pixel was used as the location of the beam center.

Table 5.2: Results of the refinement of the first estimate of the beam center location. The weighted average location of the beam center is shown to lie on the pixel in the direct beam mark with the highest intensity, (1038,981).

coordinate	$m_{BG}$	$n_{BG}$
pixel number	1038.1	981.0

#### 5.2.4. Detector tilt determination

When the surface of the detector is not placed perpendicularly to the incoming beam, the expected locations of the diffraction spots on the detector form ellipses instead of circles. Since the masking operation discards any pixels that do not lie within the area in which the spots are expected to be located, it was imperative that the shape of these ellipses was known. Therefore, the detector misalignment needed to be characterized.

Subsection 4.2.4 has presented the way in which the detector tilt can be described. Two angles are required: one for defining the direction of the tilt ( $\eta_T$ ), and one representing the amount of tilt ( $\varphi$ ). The ESRF software FIT2D computed the detector misalignment using the diffraction image of lanthanum hexaboride,  $\text{LaB}_6$ ; its diffraction pattern was presented in Figure 4.3. The beam center computed as described in the previous section was used for the FIT2D tilt characterization routine. The results of the routine are presented in Table 5.3.

The TILT routine within FIT2D produced the angles  $\varphi$  and  $\eta_{\text{FIT2D}}$ , which together define the exact detector misalignment. Using equation (4.1),  $\eta_{\text{FIT2D}}$  could be

transformed into  $\eta_T$ . This angle is also listed in Table 5.3. To obtain an idea of the amount of distortion of the circular diffraction rings into ellipses, the value of the long axis of one of the ellipses can be compared to the radius of the corresponding undistorted ring. Take for instance the outer perimeter of the  $\{220\}$  diffraction ring. The value for  $2\theta$  associated with the undistorted ring is  $7.3^\circ$ . Using this value as the input parameter to the routine creating the masks, the length of the long axis of the  $\{220\}$  diffraction 'ring',  $R_{l,max}$ , can be expressed in terms of its length in the undistorted case,  $R_{0,max}$ . The value obtained in this case is  $R_{l,max} = 1.010 R_{0,max}$ . So, the detector misalignment increased the radius of the diffraction ring with about 1% in the direction perpendicular to the rotation axis. Note that the ellipse's short axis did not differ significantly from the original radius,  $R_{s,max} = 1.000 R_{0,max}$ .

Table 5.3: Results of the detector misalignment characterization using the FIT2D TILT function. For definitions of angles, see subsection 4.2.4.

parameter	$\varphi$ ( $^\circ$ )	$\eta_{FIT2D}$ ( $^\circ$ )	$\eta_T$ ( $^\circ$ )
angle	8.1	-11.9	11.9

### 5.2.5. Sample-detector distance determination

As outlined in subsection 4.2.5, no measurement of the distance between the sample and the detector was conducted during the experiments under consideration in this project. The sample-detector distance had to be derived on the basis of visual inspection of the  $\text{LaB}_6$  diffraction pattern.

Using the value of  $\eta = 11.9^\circ$  for the direction of the rotation axis, the intercept of the rotation axis with the  $\{110\}$ -ring of the  $\text{LaB}_6$  pattern could be determined. This, in turn, yielded a value of  $R_{110} = 268$  pixels for the distance between the intercept and the beam center. Since the points on the rotation axis are unaffected by the detector misalignment, this value represented the radius of the undistorted  $\{110\}$ -ring. With  $2\theta_{110} = 3.0^\circ$ , this resulted in a sample-detector distance of just over 5000 pixels.

For the conversion from units of pixels to millimeters, the pixel sizes contained in the FIT2D splinefile were used. This file provided values of 46.8 and 48.1  $\mu\text{m}$  for the width and height of the Frelon2K pixels; averaging these, an effective pixel size of 47.4  $\mu\text{m}$  was obtained. Note that this is over three times as large as the pixels' physical dimension of 14  $\mu\text{m}$ . Taking this value to transform the sample-detector distance from units of pixels to millimeters resulted in a value of 241 millimeter.

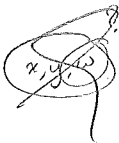
5.3. Peak detection

After obtaining the results from the pre-analysis operations, the peak scanning process was carried out. This section contains the results of this part of the analysis. Firstly, it discusses some of the general characteristics of the peak list generated as output. This is followed by more detailed discussions on some of the results of the peak detection process.

5.3.1. Output characteristics

The final output of the peak detection procedure was a list of pixels within the diffraction images with intensities higher than a certain threshold value and also higher than the intensities of their 26 neighbors in  $(x,y,\omega)$ -space. Figure 5.5 displays part of this output list for dataset 4d.

In the list, each row corresponds to a single peak. For some peaks, the entries are shifted slightly as a result of the tab-delimitation. First of all, the details of the image in which the peak was found are recorded. Each image is defined by its values for *stripe*, *layer* and  $\omega$ . The part depicted in Figure 5.5 is taken from near the top of the list; this follows from the fact that all peaks listed here have the smallest possible values for *stripe* and *layer*. The fourth column contains an integer representing the diffraction ring in which the peak was located; 1 for  $\{200\}$ , 2 for  $\{220\}$ . V and VI contain the pixel's coordinates. The subsequent columns contain more of the peak characteristics: the distance to the beam center  $R$  (in units of pixels), the angle  $2\theta$  between the incoming beam and the diffraction vector, and the azimuthal angle  $\eta$ . Column X contains the pixel's intensity (in number of counts). Note that this



I			V		R	2 $\theta$	$\eta$	X	Y	HWHM	XV			IXX		
0	0	-28	1	1091 1429	451.12	5.0704	96.947	679.18		2	1	1	1089 1092 1428	1430	-29	-27
0	0	-28	1	1273 613	436.63	4.9084	237.44	4134.4		1	1	1	1272 1274 612	614	-29	-27
0	0	-28	1	1430 794	434.32	4.8825	205.5	99.227		2	2	1	1428 1431 792	795	-29	-27
0	0	-28	2	443 842	511.02	6.8527	346.85	737.18		2	2	1	442 445 841	844	-29	-27
0	0	-28	2	475 1231	516.01	6.9081	23.944	155.27		2	2	1	473 476 1230	1233	-29	-27
0	0	-28	2	634 1461	527.39	7.0345	49.914	70.955		2	2	1	632 635 1459	1462	-29	-27
0	0	-28	2	880 382	519.49	6.9467	284.78	152.27		1	2	1	879 881 380	383	-29	-27
0	0	-28	2	1536 618	516.26	6.9109	216.09	519.77		2	2	1	1535 1538 616	619	-29	-27
0	0	-27	1	1007 542	440.09	4.9471	274.04	2051.1		2	1	1006	1008 541 544	-28	-26	
0	0	-27	1	1159 560	438.04	4.9241	253.96	77.636		2	2	1	1158 1161 558	561	-28	-26
0	0	-27	1	1205 1401	451.98	5.08	111.68	3800.5	1	2	1	1204	1206 1399 1402	-28	-26	
0	0	-27	2	616 1440	623.51	6.9914	47.405	75.909		1	2	1	615 617 1439	1442	-28	-26
0	0	-27	2	1172 374	621.61	6.9704	257.55	387.27		2	2	1	1170 1173 372	375	-28	-26
0	0	-27	2	1181 1611	646.03	7.2412	102.79	674.86		1	2	1	1180 1182 1610	1613	-28	-26
0	0	-27	2	1244 1593	645.74	7.2381	108.6	948.05		2	1	1	1242 1245 1592	1594	-28	-26

Figure 5.5: Part of the output file of the  $d$ -series peak detection procedure. Each row in this list corresponds to a single peak. Columns I-III describe the image in which the peak was located (*stripe*, *layer*,  $\omega$ ). IV contains an integer representing the peak's diffraction ring: 1 for  $\{200\}$ , 2 for  $\{220\}$ . Columns V and VI contain the pixel's detector coordinates. The rest of the columns contain  $R$ ,  $2\theta$ ,  $\eta$ ,  $I$ , and HWHM details for all three dimensions.

intensity does not have to be an integer, since the dark current value that is subtracted from each pixel is an average over 22 images and therefore in general will also not be an integer. The last nine columns, finally, give the corresponding spot's HWHM details in all three dimensions. (?)

The output lists contain the information of all the peaks detected in the diffraction images of the corresponding datasets. Table 5.4 displays some of the characteristics of these sets of peaks. The first three entries ( $N_0$ ,  $N_1$  and  $N_2$ ) represent the number of peaks found in the first, second and third stripe, respectively. For dataset *4e*, clearly  $N_1$  and  $N_2$  have no significance since these data were recorded using only a single stripe.

Table 5.4: Some important characteristics of the lists of peaks found in the diffraction images belonging to the *4d* and *4e* datasets. Listed are the numbers of peaks found in each stripe ( $N_0$ ,  $N_1$ ,  $N_2$ ) and in each ring ( $N_{200}$ ,  $N_{220}$ ). Furthermore, the average diffraction angles  $2\theta$  are listed, as well as the average azimuthal angle  $\eta$ .

	$N_0$	$N_1$	$N_2$	$N_{200}$	$N_{220}$	$\langle 2\theta_{200} \rangle$	$\langle 2\theta_{220} \rangle$	$\langle \eta \rangle$
<i>4d</i>	32702	17236	11523	28444	33017	4.95°	7.03°	176.3°
<i>4e</i>	60899	-	-	27921	32978	4.95°	6.99°	177.5°

*useful?*  
*significant?*

5.3.2. Background intensity

A detailed characterization of the amount of background intensity in either dataset was of prime importance for determination of the correct value for the intensity threshold described in subsection 4.3.3. Table 5.5 presents the results of this background characterization.

As mentioned in subsection 4.3.3, the background consisted of two components. The first is the electronic background intensity, which was characterized as being nearly constant at a value of 1000 counts (see subsection 5.2.2). The second component is the non-electronic background, which will generally vary with position from the beam center. Both contributions can be identified from Table 5.5. For the *d*-series, the average intensity per pixel in both background rings can be seen to be approximately equal to the average dark current intensity of the corresponding images. This implies that the non-electronic contribution to the total average background intensity was negligible, and the threshold criterion as derived from equation (4.4) could be based solely on the dark current intensities. The initial assumption of  $n=2$  proved to be adequate for dataset *d*, and therefore the intensity threshold for this dataset became

*how?*  
*7*

$$I_{Min,d} = 2\sqrt{\langle I_{DC} \rangle} \quad (5.1)$$

For dataset *e*, however, the difference between the dark current intensity and the total average background intensity is substantial. An equation similar to equation (5.1) would therefore not suffice in describing an appropriate criterion for dataset *e*. Instead of just  $I_{DC}$ , the criterion for the *e* dataset also needed to take into account the non-electronic background. This manifested itself not only in the square root term, but also as an additional offset term. Since the average intensities in the two background rings of the *e*-series varied by only about a single count, averaging of the two so as to arrive at a single average background intensity for both diffraction rings seemed acceptable. This averaging produced an average total background intensity of 1020 counts. The difference between this value of 1020 and the average dark current intensity then needed to be included in the threshold criterion as the offset term.

Furthermore, on visual inspection of the results of the first run of the peak detection within dataset *e*, the list appeared to contain an unusually large amount of incorrectly identified peaks. These were mainly pixels near the outer perimeters of diffraction spots. Due to statistical variations in the background intensities of such pixels, they often formed a local maximum and were therefore included in the peak list. This was undesirable since these spots were already represented in the peak list by the pixel within the spot with the absolute highest intensity. The effect was witnessed to a much lesser extent in dataset *d*. To reduce the amount of pixels incorrectly identified in this manner, the value of  $n$  was increased from 2 to 3. All in all, the intensity threshold criterion for dataset *e* became

$$I_{Min,e} = 3\sqrt{1020} + (1020 - \langle I_{DC} \rangle) \quad (5.2)$$

Table 5.5: Average intensities for the background rings in the two datasets,  $\langle I_{BG1} \rangle$  and  $\langle I_{BG2} \rangle$ , compared to the average intensity of the dark current images used for correction of the respective dataset,  $\langle I_{DC} \rangle$ . Whereas these values are nearly equal for the *d*-series, the *e*-series appears to contain a significant contribution from the non-electronic background.

	$\{200\}$ $\langle I_{BG1} \rangle$ (# counts)	$\{220\}$ $\langle I_{BG2} \rangle$ (# counts)	$\langle I_{DC} \rangle$ (# counts)
<i>d</i>	1001.0	1001.1	1000.3
<i>e</i>	1019.3	1020.7	1000.4



### 5.3.3. Peak count dependence on stripe

Table 5.4 shows a decrease in the number of peaks recorded with increasing stripe number in the  $d$ -set. Since the illuminated volume was located relatively far away from the sample's top and bottom surfaces, and since no irregularities in the grain shape distribution are expected, this decrease does not appear to be attributable to a real dependence of the average grain size on location. However, since the peaks were recorded stripe by stripe, the decrease in peak count with stripe number is equivalent to a decrease in the number of diffraction peaks with time. It is conceivable that the austenitic microstructure had not yet reached its equilibrium grain size distribution when the measurements were started. This would imply that the period of 1 hour during which the sample was held at 1000 °C to allow for stabilization of the microstructure (part  $c$  of the overall experiment; see Figure 3.4) did not suffice. Grain growth would then continue during the data recording, which would lead to a decreasing number of grains during the experiment and therefore to a decreasing number of reflections.

*at a reasonable rate?*

If the microstructure had not yet reached its equilibrium state at the onset of the experiment, then the total number of reflections per layer as a function of layer

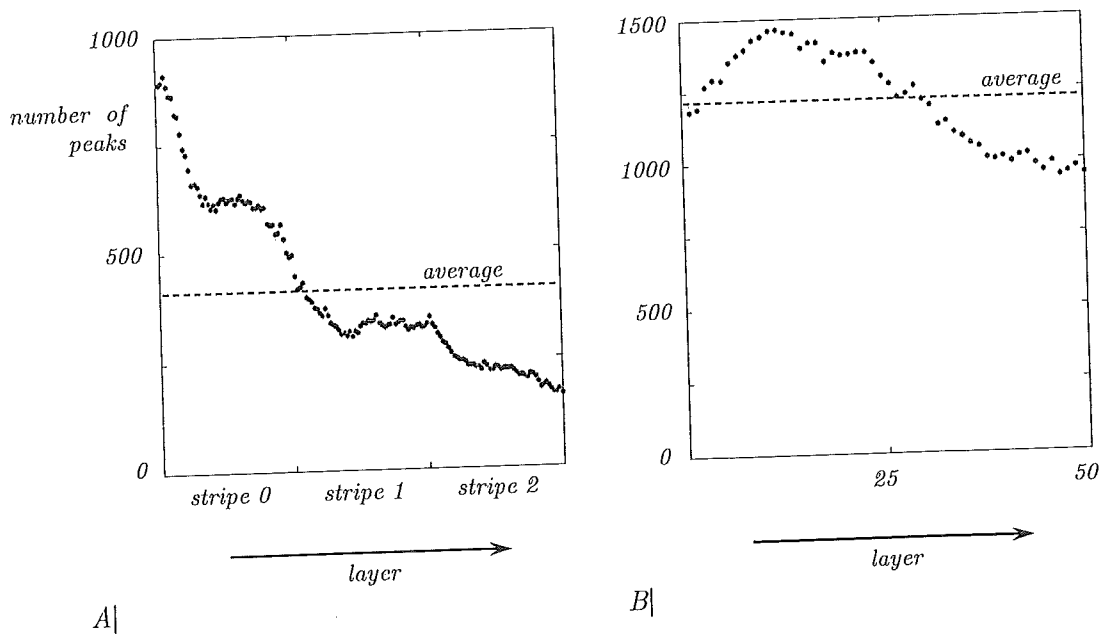


Figure 5.6: Plots of the number of peaks detected per layer as a function of stripe and layer number for datasets  $d$  and  $e$  (A and B, respectively). The horizontal axis defines increasing stripe and layer number, and therefore corresponds to increasing time. The number of peaks per layer in the  $d$ -set shows a general decreasing trend with time; the trend in  $e$  is less clear, but also appears to be decreasing. The dashed lines depict the average levels of 410 and 1218 peaks per layer, respectively.

number should also show a general trend of decrease with increasing layer number. Figure 5.6 presents the corresponding graphs. Indeed, the numbers of peaks found per layer decrease with increasing stripe and layer number, or in other words with time. For the  $4d$  series, the numbers decrease from a maximum of about 900 at the start of the experiment to about 165 for the last few layers. The number of peaks per layer in the  $4e$  dataset varies between almost 1500 and just under 1000 peaks; a general trend is more difficult to distinguish in this case. The horizontal dashed lines in the two plots indicate the averages for the two datasets: 410 peak per layer for  $4d$ , and 1218 peaks per layer for  $4e$ .

Figure 5.6 suggests that the austenitic microstructure had not yet stabilized at the time the experiment was started. If this was the case, then this should be visible in the dataset corresponding to part *c* of the entire experiment. During part *c*, the sample was held at a temperature of 1000 °C for a period of 1 hour to allow the microstructure to stabilize (see Figure 3.4). Diffraction patterns were collected during this period to obtain an idea of the progress of the stabilization process. Unfortunately, however, these data were lost at a later stage. Therefore, no direct information is available on the evolution of the sample's microstructure during the hour before start of the  $4d$  measurement. However, before the experiment at the ESRF, a limited number of measurements of grain size development during austenitizing in the material under investigation in this project had already been

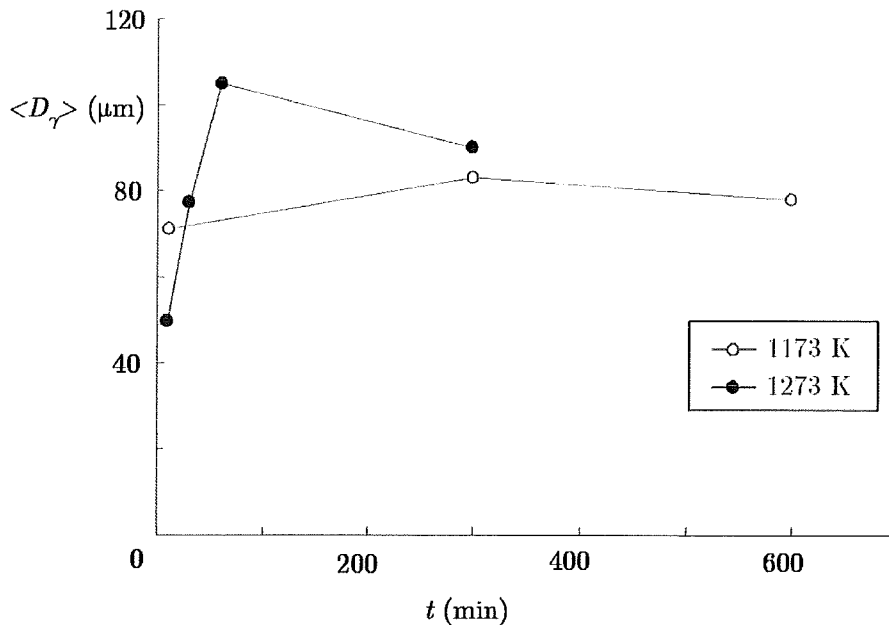


Figure 5.7: Average austenite grain diameter  $\langle D_\gamma \rangle$  in the material under consideration in this project as a function of austenitizing time  $t$  for two different austenitizing temperatures. The uncertainties are of the sizes of the symbols used. One of the temperatures equaled the one used during the experiment conducted at the ESRF; the other was 100 K lower.

performed. The results of these measurements are shown in Figure 5.7.

Although the data presented in Figure 5.7 are limited, some cautious remarks can be made in relation to the decrease in the number of peaks per layer as witnessed in Figure 5.6. One of the temperatures at which the austenitizing treatments represented by the data of Figure 5.7 were carried out equaled the temperature employed during the austenitizing treatment (part c) of the overall experiment considered in this project; the other was 100 K lower. For both temperatures, the data do not show any clear indication that the microstructure was already fully stabilized after an hour of austenitizing. For the highest temperature, stabilization might just have been reached after an hour, but it could also be that grain growth was still occurring (this is difficult to determine since either the data point at 1 hour or at 5 hours is probably an outlier). For the data corresponding to a temperature of 1173 K, it is not possible to define a point at which microstructural stabilization appeared to be attained. All in all, the figure does not provide any clear indication that the austenite microstructure at the start of measurement 4d was already fully stabilized. So, the decrease in the number of peaks found per layer could be representative of grain growth still occurring while experiments 4d and 4e had already been started.

Since no accuracy is given.

It should be noted, though, that there are other possible explanations for this decrease in number of peaks. For instance, the amount of background pixels incorrectly identified as peaks in the upper stripe could for some reason be larger than in the other stripes. This effect is examined further in section 5.4, in which the sizes of the spots corresponding to the detected peaks are taken into account.

### 5.3.4. Peak count dependence on diffraction ring

Returning to Table 5.4, two other characteristics of the lists of peaks are the number of peaks found in either ring,  $N_{200}$  and  $N_{220}$  (for the  $\{200\}$ - and  $\{220\}$ -ring, respectively). The real values of interest here are not the numbers of peaks themselves, but more their relative sizes. Diffraction theory predicts that, for a powder sample, the number of peaks found in a specific diffraction ring should be proportional to the multiplicity of the corresponding group of reflections [37]. Although for a single diffraction pattern the assumption of a powder sample is violated due to the small dimensions of the beam size, on summing the peaks from all individual diffraction images the reasoning should be valid again. The multiplicities of the  $\{200\}$ - and  $\{220\}$ -ring are 6 and 12, respectively, leading to an expected value for  $N_{220}$  of two times  $N_{200}$ . However, Table 5.4 shows that the observed relation between the two is more in the order of  $N_{220} = 1.17 \times N_{200}$ .

This discrepancy could be explained by realizing that not all of the pixels listed in the two peak lists will represent real peaks. Each pixel that is evaluated using the peak detection criteria has a certain probability of incorrectly being identified as a peak due to an unexpected fluctuation in that pixel's background intensity. Clearly, this probability is (nearly) independent of the ring in which the pixel is located. In this manner, a 'background' of incorrectly identified pixels is added to the groups of peaks in each ring. Since this background is expected to consist of an approximately equal amount of pixels for both rings (correcting for the difference in size of the rings), the 2:1 relation between  $N_{220}$  and  $N_{200}$  will tend to be diluted towards unity.

$$\left( \frac{N_{220}}{N_{200}} + N_0 \right) = 1.17 \left( \frac{N_{200}}{N_{220}} + N_0 \right)$$

### 5.3.5. Peak count dependence on azimuthal angle

$$\begin{aligned} N_{220} &= 2 N_{200} \\ \Rightarrow 0.83 N_{200} &= 0.17 N_0 \Rightarrow \frac{N_0}{N_{200}} \approx 5 \end{aligned}$$

(832 is correct 1.17)

The last few entries in Table 5.4 relate to the average diffraction angles  $\langle 2\theta_{200} \rangle$  and  $\langle 2\theta_{220} \rangle$  and the average azimuthal angle  $\langle \eta \rangle$  (though these are only a first estimate, since for a real determination of  $2\theta$  and  $\eta$  the center of mass of the reflection should be used). It can be seen that the average diffraction angles as listed in the table are nicely located near the center of the angular ranges of the diffraction rings as prescribed by the masks ([4.75;5.2] and [6.8;7.3] for the  $\{200\}$ - and  $\{220\}$ -ring, respectively), and are close to the theoretical diffraction values as computed in subsection 4.3.1 ( $4.9^\circ$  and  $6.9^\circ$ ). The average azimuthal angle is also close to the

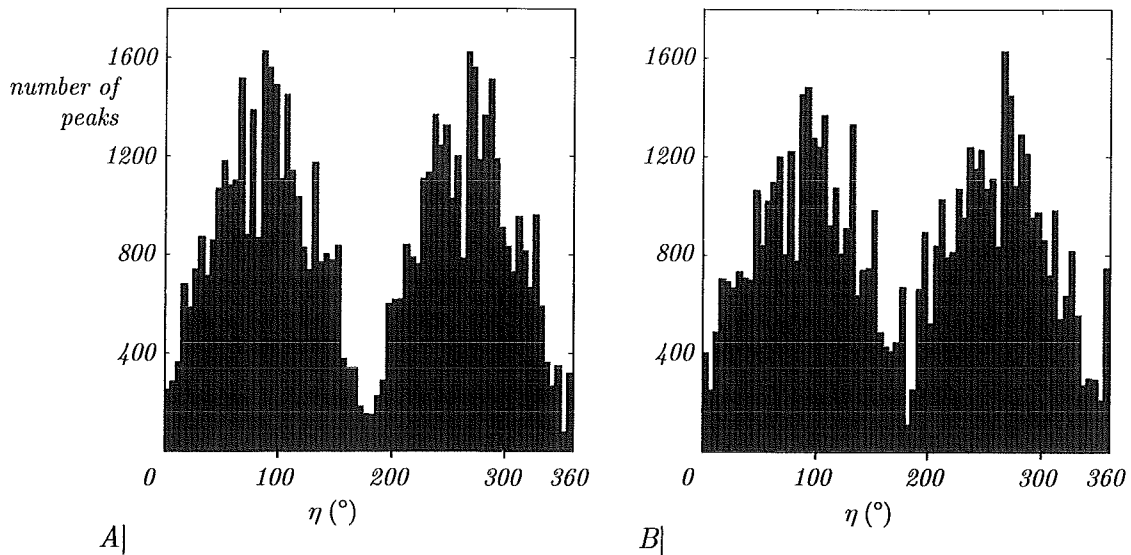


Figure 5.8: Histograms of the number of peaks as a function of the scattering vector's azimuthal angle  $\eta$  for datasets  $d$  (A) and  $e$  (B). A general trend of a decreasing number of peaks with  $\eta$  moving towards the poles is clearly visible in both figures. This effect is a direct consequence of the fact that a rotation of  $\Delta\omega$  about the rotation axis produces a change of only  $|\sin(\eta)|\Delta\omega$  in scattering vector.

expected value of  $180^\circ$ . It should be noted that  $\eta$  does not follow a uniform probability distribution over the interval  $[0, 360]$ . This is evidenced by Figure 5.8. This figure displays histograms of the number of peaks in each of the two datasets as a function of the azimuthal angle of the scattering vector associated with that peak. Both datasets show maxima in the number of peaks around values of  $90^\circ$  and  $270^\circ$ . This phenomenon can be understood by understanding the interplay between rotation about the  $\omega$ -axis and translation along the  $\eta$ -direction. As explained in subsection 3.1.3, a rotation about the  $\omega$ -axis of  $\Delta\omega$  results in a change in scattering vector of only  $|\sin(\eta)|\Delta\omega$ . This implies that the absolute change in scattering vector away from the poles is significantly larger than for vectors near the  $0^\circ$ - and  $180^\circ$ -points. This results in new grains coming into reflection quicker and therefore in maxima in the peak counts around angles of  $90^\circ$  and  $270^\circ$ . *⇒ divide fig. 5.8 by  $|\sin \eta|$*

In conclusion, the characteristics of the data in the peak lists are within the expected ranges, or can well be explained by taking some specific factors into account. The number of peaks found is relatively high, but this should be seen in the light of the presence of a 'background' of incorrectly identified pixels, as well as the fact that a single reflection can easily show up in multiple diffraction images as the corresponding grain is translated into and out of the line beam. The data do suggest that the microstructure had not yet stabilized when the measurements were conducted, a feature detrimental to the accuracy of the analysis.

## 5.4. Spot characterization

When peak detection has finished, the analysis moves on to the characterization of the spots associated with the individual peaks. The output from this part of the reconstruction consists again of a large list, this time containing the individual spots and their associated characteristics.

### 5.4.1. Output characteristics

Figure 5.9 displays part of the output of the spot characterization process for dataset *d*. Each row corresponds to a single spot. The first three entries in each row describe the diffraction image in which the original peak associated with the spot in question was detected. The fourth column again contains the value of  $\omega$  for the spot in question, only this time the spot's weighted average has been computed. Only a small fraction of all spots in either set extended into more than one diffraction image, meaning that for most of the spots the value of  $\omega$  as taken from the original peak's diffraction image equaled the value computed using a weighted average. In fact, the average absolute difference between  $\omega$  (the amount of rotation of the original image,

I			V			X			XV					
0	0	-28	-28	1	1434.1	791.03	439.02	4.7964	205.69	429.38	3	3	1	9
0	0	-28	-28	2	468.95	1233.8	622.98	6.7902	23.903	565.76	3	3	1	9
0	0	-28	-28	2	629.33	1462.1	631.3	6.8801	49.599	260.05	3	3	1	9
0	0	-28	-28	2	874.78	368.78	634.09	6.9102	284.96	303.28	1	3	1	3
0	0	-27	-27	1	1161.9	551.78	446.96	4.8828	253.97	336.19	3	3	1	9
0	0	-27	-27	1	1201.6	1399.5	448.85	4.9032	111.31	19912.5	7	3	105	
0	0	-27	-27	2	611.42	1442	628.15	6.846	47.164	158.37	1	3	1	3
0	0	-27	-27.009	2	1173.2	360.85	634.97	6.9197	257.75	2659.3	5	5	3	75
0	0	-27	-27.001	2	1173.9	1605.2	638.37	6.9563	102.25	2760.7	3	5	3	45
0	0	-27	-26.994	2	1236.7	1586.7	636.97	6.9413	108.12	5000.7	5	3	3	105
0	0	-27	-27	2	1278.9	1569.9	635.73	6.9279	112.22	203.85	3	1	1	3
0	0	-27	-26.99	2	1443.4	499.89	629.11	6.8564	229.94	6230.8	5	5	3	75
0	0	-26	-25.999	1	645.44	1178.8	439.84	4.8053	26.664	1.1468e+005	11	11	3	363
0	0	-26	-26.009	1	671.82	737.93	440.14	4.8086	326.42	13269.7	7	3	3	147
0	0	-26	-26.006	1	877.74	1400	448.47	4.8992	68.995	3119.7	5	3	3	45
0	0	-26	-26.004	1	1082.5	525.58	448.05	4.8947	264.24	22648.41	9	3	3	207

Figure 5.9: Part of the output file of the  $d$ -series spot characterization procedure. Each row in this list corresponds to a single spot. Columns I-III describe the image in which the original peak was located (*stripe*, *layer*,  $\omega$ ). IV contains the weighted average value for  $\omega$ ; V describes the diffraction ring. Columns VI-X describe the spot's weighted average location on the detector. XI contains the total intensity, and XII through XV describe the size of the spot (in amounts of pixels).

contained in the third column) and  $\omega_{\text{avg}}$  (the weighted average amount of rotation, contained in the fourth column) was only about  $0.011^\circ$  for the  $d$ -series and  $0.037^\circ$  degrees for the  $e$ -series. The difference between these two average values arises from the difference in beam dimensions between the two sets. Since set  $e$  was recorded using larger beam sizes, diffracting volumes will on average have been larger, increasing the effects of for instance mosaicity or local variations in lattice parameters. This manifested itself as a larger spread in  $\omega$  within a single diffraction spot. Still, for both sets the average absolute differences are quite small, indicating that the likelihood of a single diffraction spot extending into two images is small, let alone the likelihood of it extending into more than two images.

Returning to Figure 5.9, column V indicates in which ring the spot is located, in the same manner as the fourth column of Figure 5.5. VI through XI contain the spot's weighted average location on the detector and values of  $R$ ,  $2\theta$ ,  $\eta$  and total intensity  $I$ . The coordinates have been corrected for spatial distortions, and the total intensity has been corrected for background contributions. The last four columns of the file denote the amount of pixels attributed to the peak in question. Columns XII through XIV list the spot's full width in each of the three dimensions (row coordinate, column coordinate and  $\omega$ , respectively), and the last column contains the total amount of attributed pixels.

The list contains all necessary information on the spots located in the images of the dataset in question. As mentioned, the spot characterization is performed based on the list of peaks produced by the peak detection process. However, not every peak will produce an entry in the spot list. As mentioned in section 4.4, spots can be rejected as a consequence of overlap with other spots. Furthermore, spots are deemed unfit for analysis in case they are located too near to the limits of the  $\omega$

regime or in case the routine is unable to define adequate peak box dimensions. The number of entries in the spot list is therefore expected to be lower than the number of peaks registered during the detection process and written to the peak list. Table 5.6 lists some general characteristics of the spots detected and characterized in both sets. These characteristics can be compared to those of the list of peaks as summarized in Table 5.4. In this way, a possible bias in the translation from peaks to spots can be traced.

Table 5.6: Some important characteristics of the lists of spots in the diffraction images belonging to the  $4d$  and  $4e$  datasets. Listed are the numbers of spots located in each stripe ( $N_0$ ,  $N_1$ ,  $N_2$ ) and in each ring ( $N_{200}$ ,  $N_{220}$ ). Furthermore, the average diffraction angles  $2\theta$  are listed, as well as the average azimuthal angle  $\eta$ .

	$N_0$	$N_1$	$N_2$	$N_{200}$	$N_{220}$	$\langle 2\theta_{200} \rangle$	$\langle 2\theta_{220} \rangle$	$\langle \eta \rangle$
$4d$	29431	15274	10514	25200	30019	$4.86^\circ$	$6.88^\circ$	$175.4^\circ$
$4e$	38693	-	-	17526	21167	$4.86^\circ$	$6.89^\circ$	$176.2^\circ$

The characteristic to be analyzed is the total number of spots in relation to the number of peaks in the input peak list. For set  $d$ , the total number of spots equals 55219 against an original 61461 peaks, giving a reduction of about 10.2%. Set  $e$  contained 60899 peaks, but only 38693 spots, giving a reduction of 36.5%. The difference between these two percentages is quite significant. In dataset  $e$ , much more peaks were rejected. This can partly be explained in light of the larger beam dimensions of dataset  $e$ . As a result, the chance of spot overlap was also higher, resulting in more spots having been rejected. Furthermore, most of dataset  $e$ 's additional background pixels as mentioned in subsection 5.3.2 will also have been discarded at this point, resulting in a higher reduction percentage for this dataset.

Note that dataset  $d$  still shows the difference in number of spots per stripe already seen in the peak list (see subsection 5.3.3). However, now that the dimensions of the spots corresponding to the individual peaks are known, another possible explanation for the decrease in peak count can be examined. The difference in number of peaks could be explained by an unusually high number of incorrectly identified peaks in the upper stripe. These incorrectly identified peaks are simply background pixels, and therefore the 'spots' they represent will generally be quite small (most likely only one or a few pixels). So, plotting the number of spots as a function of time, but excluding all spots smaller than a certain size would give an indication of the amount of these smaller spots in each dataset. Figure 5.10 depicts this plot. It shows the number of spots as a function of layer number for both datasets; however, spots smaller than or equal to 5 pixels in any of the two detector

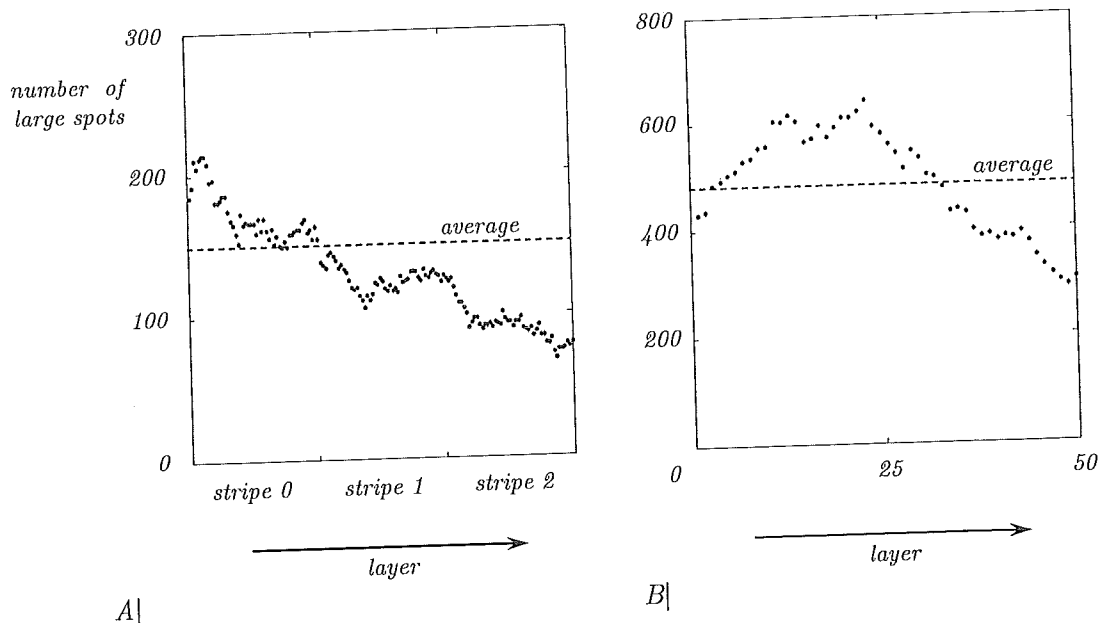


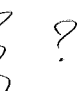
Figure 5.10: Plots of the number of large spots per layer as a function of stripe and layer number for datasets *d* and *e* (A and B, respectively). Spots smaller than or equal to 5 pixels in either of the two detector dimensions have been omitted from these figures. The number of spots per layer in the *d*-set still shows a decrease with time as in Figure 5.6; however, the decrease is less drastic. The trend in *e* appears unaltered. The dashed lines depict the average levels of 130 and 488 spots per layer.

dimensions have been omitted from the figures. The plots can be compared to those of Figure 5.6. It can be seen that the general trends of the two correspond quite well. However, the decrease in number of spots of the *d*-series with time is smaller than the decrease in peaks of Figure 5.6. So, it appears that a significant amount of the extra peaks registered in the earlier parts of the scan correspond to very small spots – most likely simply background perturbations. This effect explains, at least partly, the shape of the plot in part A| of Figure 5.6.

The ratio between the number of peaks found in each diffraction ring is slightly higher than the ratios found for the peaks:  $N_{220} = 1.20 \times N_{200}$ , whereas for the peak list the ratio was about 1.17. This agrees with the explanation for this ratio provided in subsection 5.3.4: the spot characterization process filters out some of these background pixels, bringing the ratio between the two back up closer towards the theoretical value.

The average diffraction angles of the spots in the two datasets are somewhat lower than the average angles of the locations of the peaks. This could imply several things. It could be that the diffraction spots are not Lorentzian-shaped, but instead have their maximums located more towards the higher angles with longer tails nearer to the beam center. In that case, a spot's center of gravity would be located at a



smaller diffraction angle than the spot's maximum. However, the author cannot conceive any reason for this significant deviation from Lorentzian shape. The effect could also simply be a result of the application of the spatial distortion correction to the spots' center of gravity coordinates. ? 

The average azimuthal angle of the spots in the two sets is approximately equal to the value obtained in the lists of peaks. The small decrease of about a single degree for either set could also be the result of the application of the spatial distortion correction.

## 5.5. Spot grouping

The third main part of the actual dataset analysis was the grouping of spots belonging to the same reflection. The spot list of which Figure 5.9 shows an excerpt was used as input for this process. The results consisted of two lists: one with all the individual spots grouped together into complete reflections, and one with every reflection's total intensity, center of mass coordinates etc. Furthermore, the profile of intensity versus illuminated volume of each reflection was also reconstructed and saved.

### 5.5.1. Output characteristics

Figure 5.11 contains parts of the lists produced as output during the spot grouping process of dataset 4e. A| displays part of the list in which the individual spots have been grouped together into separate reflections, whereas B| contains the characteristics of those reflections.

Each row within the first list corresponds to a single spot. The various columns in A| contain exactly the same values as the spot list shown in Figure 5.9; however, an extra column has been added to the left side of the list. This column contains the number of the reflection to which the spot has been assigned. Note the use of both integer and non-integer numbering<sup>3</sup>. This feature was already touched upon in subsection 4.5.1 (regarding the numbering of the spots in scenario B| of Figure 4.11). Integer numbering indicates that the spots found at the same value of  $\omega$  and on the same location on the detector formed an incrementing sequence. For instance, examine the spots assigned to reflection 5. This reflection consists of five spots, the layer numbers of which (included in column III) form an incrementing sequence without missing entries: 39 through 43. Now examine spot groups 6.01 and

---

<sup>3</sup> As a result of the way in which the list was saved, the integer reflection numbers have also been given two decimal zeros. The distinction between the two types of numbers can still be made, though.

A|

I				V				X				XV			
4.01	0.00	38.00	-28.00	-28.00	1.00	735.43	1304.50	443.05	4.84	46.84	659.19	3.00	5.00	1.00	15.00
4.02	0.00	40.00	-28.00	-28.00	1.00	735.55	1305.20	443.46	4.84	46.91	599.60	3.00	3.00	1.00	9.00
4.02	0.00	41.00	-28.00	-28.00	1.00	735.99	1304.40	442.56	4.84	46.88	1057.50	3.00	5.00	1.00	15.00
4.02	0.00	42.00	-28.00	-28.00	1.00	736.08	1304.50	442.55	4.83	46.89	934.58	3.00	3.00	1.00	9.00
4.02	0.00	43.00	-28.00	-28.00	1.00	736.17	1304.50	442.48	4.83	46.90	1142.30	3.00	3.00	1.00	9.00
5.00	0.00	39.00	-28.00	-28.00	1.00	808.55	1362.80	445.39	4.87	58.92	1515.60	3.00	5.00	1.00	15.00
5.00	0.00	40.00	-28.00	-28.00	1.00	808.64	1362.80	445.39	4.86	58.92	1261.10	3.00	5.00	1.00	15.00
5.00	0.00	41.00	-28.00	-28.00	1.00	808.69	1362.80	445.30	4.87	58.94	1021.70	3.00	5.00	1.00	15.00
5.00	0.00	42.00	-28.00	-28.00	1.00	808.74	1362.80	445.31	4.86	58.94	973.84	3.00	5.00	1.00	15.00
5.00	0.00	43.00	-28.00	-28.00	1.00	808.74	1362.80	445.11	4.86	59.01	932.68	3.00	5.00	1.00	15.00
6.01	0.00	12.00	-28.00	-28.00	1.00	924.72	1413.80	447.15	4.88	75.26	2400.70	3.00	5.00	1.00	15.00
6.01	0.00	13.00	-28.00	-28.00	1.00	924.84	1413.70	447.07	4.88	75.27	1890.80	3.00	5.00	1.00	15.00
6.02	0.00	15.00	-28.00	-28.00	1.00	925.44	1413.90	447.02	4.88	75.35	1518.20	3.00	5.00	1.00	15.00
6.02	0.00	16.00	-28.00	-28.00	1.00	925.48	1413.90	447.04	4.88	75.36	1323.90	3.00	5.00	1.00	15.00
6.02	0.00	17.00	-28.00	-28.00	1.00	925.59	1413.90	447.05	4.88	75.37	949.19	3.00	5.00	1.00	15.00
6.02	0.00	18.00	-28.00	-28.00	1.00	925.68	1413.90	446.98	4.88	75.38	869.69	3.00	5.00	1.00	15.00
6.02	0.00	19.00	-28.00	-28.00	1.00	925.71	1414.50	447.57	4.89	75.40	872.22	3.00	5.00	1.00	15.00

B|

I				V				X				XII			
3.00	0.00	31.27	-28.00	1.00	678.95	1236.18	440.70	4.95	35.32	18.00	1201.49				
4.01	0.00	38.00	-28.00	1.00	735.43	1304.50	443.03	4.98	46.83	15.00	659.19				
4.02	0.00	41.36	-28.00	1.00	736.00	1304.58	442.70	4.98	46.89	42.00	1998.25				
5.00	0.00	40.29	-28.00	1.00	808.75	1362.83	445.32	5.01	58.94	75.00	2877.68				
6.01	0.00	12.14	-28.00	1.00	924.77	1413.76	447.10	5.03	75.26	30.00	2861.00				
6.02	0.00	16.33	-28.00	1.00	925.56	1413.99	447.13	5.03	75.37	75.00	2970.32				
7.01	0.00	8.47	-28.00	1.00	949.50	543.95	446.39	5.02	281.50		45.00	1675.29			
7.02	0.00	39.40	-28.00	1.00	946.00	542.66	448.36	5.04	281.91		75.00	4339.93			
8.00	0.00	25.00	-28.00	1.00	961.59	542.69	445.37	5.01	279.95		1.00	379.44			
9.00	0.00	17.17	-28.00	1.00	1088.63	1426.75	448.19	5.04	96.42	115.00		4716.13			

Figure 5.11: Part of the output files of the *e*-series spot grouping procedure. List A| displays the individual spots grouped as reflections; B| contains the specifics of those reflections. The first column in either list contains the reflection numbers. The use of decimal numbering indicates the identification of multiple reflections which might in reality all belong to one single reflection. Other characteristics include the reflections' center of mass coordinates and their total integrated intensities.

6.02. The spots of both these groups nearly form a sequence similar to that of reflection 5; however, the entry corresponding to layer 14 is missing. As a result, the spots are divided into two groups, each given an individual reflection number. Still, visual inspection of these two groups suggests that they form one single reflection, but that for some reason one entry is missing. To be able to keep track of these kinds of occurrences, the two groups have been given non-integer numbering. In that way, the two can easily be added together at a later stage in case this seems justified.

B| displays part of the list that contains the center of mass characteristics of the reflections defined by the spot groups of list A|. Each row now corresponds to a single reflection. For each entry, the spots making up that specific reflection are taken to calculate the reflection's weighted average center of mass on the detector and associated characteristics ( $R$ ,  $2\theta$ ,  $\eta$ ). Using the intensities of the individual spots and the overlap between their corresponding slit positions, the reflection's total intensity corrected for the overlap and the profile of intensity versus illuminated volume are reconstructed. The total intensity is listed in the rightmost column. Notice that the total intensities given in B| are considerably less than the sum of the

intensities of the individual spots listed in A|. This difference corresponds to the effect of the slit overlap, resulting in double counting of significant portions of the reflection's intensity when simply summing the spots' individual contributions.

The intensity profile can be used to compute the weighted average layer number of the center of mass of the grain producing the reflections. These values are given in column III. Columns II and IV contain the weighted average stripe number and value of  $\omega$ . The former only has any significance in dataset *d*; for *e*, this column contains only zeros.

### 5.5.2. Intensity profiles

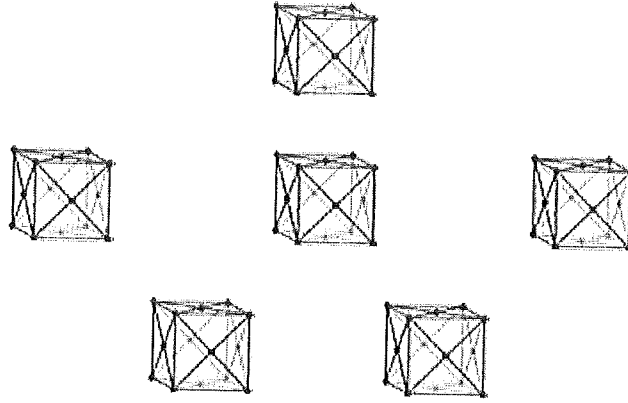
Apart from the two lists shown in Figure 5.11, the spot grouping routine also generates a collection of files containing the profiles of intensity versus illuminated volume of the individual reflections. These profiles can be seen as a first, rough indication of grain shape, since the reflected intensity scales linearly with the reflecting volume. It should be noted, though, that these are only two-dimensional representations of intensities originating from three-dimensional volumes. Furthermore, the amount of rotation about the  $\omega$ -axis determines the angle under which the grain was illuminated and therefore the shape of the projection.

Figure 5.12 displays profiles for various different types of identified reflections. The graphs display the intensity produced by part of the illuminated sample volume as a function of the relative position of the illuminating beam. This position is defined as zero at the leftmost side of the first slit setting for which the reflection in question was witnessed. Plot A| shows the most straightforward case. It depicts the intensity profile of reflection 5 of the *e*-series, which could already be inspected from Figure 5.11. B| depicts the profile of reflections 6.01 and 6.02, also listed in Figure 5.11. The plot shows that, even though in the list of spots one entry is missing, the intensity profile can still be reconstructed from the two individual groups of spots. Plot C|, finally, depicts reflection 60 from dataset *d*. This reflection consisted of spots located in two different stripes. The profiles for the intensities from the two stripes are plotted individually, with one profile on the positive and one on the negative vertical axis. } to be added?

## 5.6. Reflection matching

When the individual reflections have been reconstructed, the next task is to enter these reflections into GrainSpotter, which matches reflections originating from the same grain on the basis of the crystallographic characteristics of the material under investigation.





## 6. Conclusions and recommendations

After the theoretical treatise of chapter 2 and the introduction into the experimental procedure given in chapter 3, chapters 4 and 5 presented the results of this project. The current chapter draws some conclusions on the basis of these results and presents recommendations on how the findings of this thesis might be of use to future work.

### 6.1. Conclusions

The conclusions drawn on the basis of the results of this project as presented in the previous two chapters should be seen in light of the overall objective of this thesis. This objective was described in section 3.2 in the following manner:

*Develop a software package for the three-dimensional reconstruction of a polycrystalline microstructure from three-dimensional x-ray diffraction microscopy data, and apply this package to an available dataset.*

Section 3.2 also listed some desired characteristics for the software package: efficiency, generality, compatibility, and user-friendliness.

Based on the above objective together with the results as presented in chapters 4 and 5, the author believes it is justified to draw the following conclusions.

#### 6.1.1. On the computational methodology

Efficiency is acceptable for application to typical 3DXRD microscopy datasets

Running under a Windows XP operating system with a 1.5 GHz Intel Pentium processor, the software package required about a month for the analysis of both

datasets up to the point of the use of GrainSpotter. This is an acceptable number, considering the fact that the combined size of the datasets equaled almost 150 GB.

High generality allows straightforward adoption on different datasets

The limited amount of hard-coding of variables offers the possibility for quick adaptation of the software package for the use on different 3DXRD microscopy datasets. The instances where hard-coding was unavoidable are easily located, after which the required changes can be applied. The routines account for various effects which play only a limited role in the data analyzed in the current project, but which might have a significant influence in other sets of data to be analyzed with this software.

Compatibility with previously existing software is high

The use of MATLAB as the main programming environment ensured compatibility with previous software, which had also mainly been written in MATLAB. The use of the newly developed GrainSpotter software for the matching of the individual reflections is in line with current practice at the Risø National Laboratory in Denmark, a major partner of Delft University of Technology in the research on 3DXRD microscopy.

User-friendliness is achieved by this report and by comments contained by the code

The extensive treatments of the individual routines contained in chapter 4 and in the appendix, together with the comments included within the routines themselves, allow the reader to obtain a thorough comprehension of the workings of the software package.

### **6.1.2. On the microstructure reconstruction**

The datasets show an anomalous dependence of peak count on stripe number

The number of peaks registered within a specific stripe decreases with increasing stripe number. Two possible explanations were presented. First of all, the microstructure might still be in the process of stabilizing when measurements commenced. Secondly, the higher number of peaks in the upper stripes could represent a higher number of background pixels. This is supported by the spot count.

The results of the reconstruction are not at a satisfactory level yet

Clearly, the fact that the reflection matching process carried out using GrainSpotter could not be performed successfully leads to a lack of useful results.

## 6.2. Recommendations

As highlighted in subsection 3.1.2, the overall objective of the project carried out at the ESRF was to obtain a better understanding of nucleation behavior by deriving a relation between the parent phase in terms of its grain boundary structure and the formation of the new phase. The following recommendations provide some indications on how the results of this project could be of use in achieving this overall objective. Some more general recommendations are presented as well.

Focus speed-up attempts on spot characterization process

Most of the time required for the microstructure reconstruction from datasets  $d$  and  $e$  was spent on the spot characterization process. If one wishes to speed up the entire reconstruction process, one should focus on this spot characterization part. One could also consider developing versions of the spot characterization routine adapted specifically to the dataset at hand. For instance, for data where peak overlap is expected to play only a minor role it might be acceptable to adopt a simplified version of the peak box refinement part.

Improve and expand the final parts of the software package

At the moment, the bottleneck in actually applying this software to 3DXRD datasets is the reflection coupling process. Attempts should be made to improve this step, mainly by communicating with Risø National Laboratory on possible advances in the GrainSpotter software. Furthermore, the package could be expanded by including routines to calculate the grains' center of mass locations.

Correlate 3D microstructures with new phase formation

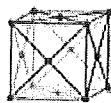
An interesting possibility for future research, fitting within the overall goal of the ESRF experiment, would be to try and correlate the microstructure before and after transformation with the locations of the ferrite nuclei and grains. Software suitable for tracking the newly formed grains had already been developed prior to the start of this experiment. By combining this software with the package developed

during this project, a relation might be established between the parent microstructure, the locations of the nuclei of the new phase, and the resulting structure.

Refine the reconstruction procedure to retrieve grain shape information

Theoretically, the resolution obtained by combining the datasets of the horizontal and vertical scans allows the retrieval of grain shape information from the diffraction images (as long as the grains are large compared to the smallest beam dimension). Currently, the retrieval and analysis of this information is not included in the reconstruction procedure. However, including this feature could produce useful results on grain shape statistics and on possible preferred nucleation sites.





## Bibliography

1. Offerman, S.E., *Evolving Microstructures in Carbon Steel: A Neutron and Synchrotron Radiation Study*. 2003, Delft University of Technology: Delft.
2. Kazaryan, A., et al., *Generalized Phase-Field Model for Computer Simulations of Grain Growth in Anisotropic Systems*. Physical Review B, 2000. **61**(21): p. 14275-14278.
3. Heritier, D., *Grain Nucleation and Growth in Steel Studied with Synchrotron Radiation*. Internship report, Delft University of Technology, 2006.
4. *Steel Statistical Yearbook 2006*. International Iron and Steel Institute, 2007. Available from <http://www.worldsteel.org>.
5. Poulsen, H.F., et al., *Applications of High-Energy Synchrotron Radiation for Structural Studies of Polycrystalline Materials*. Journal of Synchrotron Radiation, 1997. **4**: p. 147-154.
6. Hall, E.O., *The Deformation and Ageing of Mild Steels 3: Discussion of Results*. Proceedings of the Physical Society of London B, 1951. **64**(381): p. 747-753.
7. Petch, N.J., *The Cleavage Strength of Polycrystals*. Journal of the Iron and Steel Institute, 1953. **174**(1): p. 25-28.
8. Aaronson, H.I. and J.K. Lee, *The Kinetic Equations of Solid-Solid Nucleation Theory and Comparisons with Experimental Observations*, in *Lectures on the*

- Theory of Phase Transformations*, H.I. Aaronson, Editor. 2000, TMS: Warrendale.
9. Becker, R. and W. Döring, *Kinetische Behandlung der Keimbildung in übersättigten Dämpfen*. Annalen der Physik, 1935. **416**(8): p. 719-752.
  10. Volmer, M. and A. Weber, *Keimbildung in übersättigten Gebilden*. Zeitschrift für physikalische Chemie, 1925. **119**: p. 277-301.
  11. Christian, J.W., *The Theory of Transformation in Metals and Alloys*. 2002, Amsterdam: Pergamon.
  12. Zener, C., *Theory of Growth of Spherical Precipitates from Solid Solution*. Journal of Applied Physics, 1949. **20**: p. 950-953.
  13. Porter, D.A. and K.E. Easterling, *Phase Transformation in Metals and Alloys*. Second ed. 1992: Stanley Thornes Ltd.
  14. Hillert, M., *Applications of Gibbs Energy - Composition Diagrams*, in *Lectures on the Theory of Phase Transformations*, H.I. Aaronson, Editor. 2000, TMS: Warrendale.
  15. Lange, W., M. Enomoto, and H.I. Aaronson, *The Kinetics of Ferrite Nucleation at Austenite Grain Boundaries in Fe-C Alloys*. Metallurgical Transactions A, 1988. **19A**(3): p. 427-440.
  16. Lee, J.K., D.M. Barnett, and H.I. Aaronson, *Elastic Strain Energy of Coherent Ellipsoidal Precipitates in Anisotropic Crystalline Solids*. Metallurgical Transactions A, 1977. **8A**(6): p. 963-970.
  17. Read, W.T. and W. Shockley, *Dislocation Models of Crystal Grain Boundaries*. Physical Review, 1950. **78**(1): p. 275-289.
  18. Hull, D. and D.J. Bacon, *Introduction to Dislocations*. 2001, Oxford: Butterworth-Heinemann.

19. Te Veldhuis, S.G.E., et al., *A Three-Dimensional Model for the Development of the Microstructure in Steel During Slow Cooling*. Materials Science and Engineering A, 2000. **277**: p. 218-228.
20. Ågren, J., *Computers Simulations of the Austenite/Ferrite Diffusional Transformations in Low Alloyed Steel*. Acta Metallurgica, 1982. **30**: p. 841-851.
21. Ågren, J., *Numerical Treatment of Diffusional Reactions in Multicomponent Alloys*. Journal of Physics and Chemistry of Solids, 1982. **43**(4): p. 385-391.
22. Ågren, J., *A Revised Expression for the Diffusivity of Carbon in Binary Fe-C Austenite*. Scripta Metallurgica, 1986. **20**: p. 1507-1510.
23. Ham, F.S., *Diffusion-Limited Growth of Precipitate Particles*. Journal of Applied Physics, 1959. **30**(10): p. 1518-1525.
24. Horvay, G. and J.W. Cahn, *Dendritic and Spheroidal Growth*. Acta Metallurgica, 1961. **9**(7): p. 695-705.
25. Lauridsen, E.M., et al., *Kinetics of Individual Grains During Recrystallization*. Scripta Materialia, 2000. **43**: p. 561-566.
26. Margulies, L., G. Winther, and H.F. Poulsen, *In Situ Measurement of Grain Rotation During Deformation of Polycrystals*. Science, 2001. **291**(2392-2394).
27. Offerman, S.E., et al., *Evolving Microstructures in Carbon Steel Studied by X-Ray Diffraction Microscopy*. Science, 2002. **298**: p. 1003-1005.
28. Offerman, S.E., et al., *Solid-State Phase Transformations Involving Solute Partitioning: Modeling and Measuring on the Level of Individual Grains*. Acta Materialia, 2004. **52**: p. 4757-4766.
29. Poulsen, H.F., *Three-Dimensional X-Ray Diffraction Microscopy*. Springer Tracts in Modern Physics. Vol. 205. 2004, Berlin: Springer.
30. <http://www.esrf.eu/computing/bliss/guides/detection/ccd/frelon2K/>  
(February 8<sup>th</sup>, 2007).

31. Bragg, W.L., *The Diffraction of Short Electrmagnetic Waves by a Crystal*. Proceedings of the Cambridge Philosophical Society, 1912. **17**: p. 43-57.
32. Lauridsen, E.M., et al., *Tracking: A Method for Structural Characterization of Grains in Powders or Polycrystals*. Journal of Applied Crystallography, 2001. **34**: p. 744-750.
33. Poulsen, H.F., *A Six-Dimensional Approach to Microtexture Analysis*. Philosophical Magazine, 2003. **83**(24): p. 2761-2778.
34. Poulsen, H.F., et al., *Three-Dimensional Maps of Grain Boundaries and the Stress State of Individual Grains in Polycrystals and Powders*. Journal of Applied Crystallography, 2001. **34**: p. 751-756.
35. Als-Nielsen, J. and D. McMorrow, *Elements of Modern X-ray Physics*. 2001, Chichester, West-Sussex: Wiley.
36. Warren, B.E., *X-Ray Diffraction*. 1969, Reading, Massachusetts: Addison-Wesley Publishing.
37. Cullity, B.D. and S.R. Stock, *Elements of X-Ray Diffraction*. 2001, Upper Saddle River, New Jersey: Prentice-Hall.
38. Onink, M., et al., *The Lattice Parameters of Austenite and Ferrite in Fe-C Alloys as Functions of Carbon Concentrations and Temperature*. Scripta Metallurgica et Materialia, 1993. **29**: p. 1011-1016.
39. Fu, X. and H.F. Poulsen, *Generation of Grain Maps by an Algebraic Reconstruction Technique*. Journal of Applied Crystallography, 2003. **36**: p. 1062-1068.
40. Markussen, T., et al., *An Algebraic Algorithm for Generation of Three-Dimensional Grain Maps Based on Diffraction with a Wide Beam of Hard X-Rays*. Journal of Applied Crystallography, 2004. **37**: p. 96-102.
41. <http://www.esrf.eu/computing/scientific/FIT2D/> (February 8<sup>th</sup>, 2007).

42. Cox, M.G., *The Numerical Evaluation of B-Splines*. Journal of Applied Mathematics, 1972. **10**: p. 134-149.
43. De Boor, C., *On Calculating with B-Splines*. Journal of Approximation Theory, 1972. **6**: p. 50-62.
44. Dierckx, P., *Curve and Surface Fitting with Splines*. Monographs on Numerical Analysis. 1993, Oxford: Oxford University Press.
45. Gu, M., *Advanced Optical Imaging Theory*. Optical Sciences. 2000, Berlin: Springer.
46. Dekking, F.M., et al., *KANSTAT: Probability and Statistics for the 21st Century*. 2003, Delft: DUP.
47. Rees, D.G., *Foundations of Statistics*. 1987, London: Chapman and Hall.
48. Busing, W.R. and H.A. Levy, *Angle Calculations for 3- and 4-Circle X-Ray and Neutron Diffractometers*. Acta Crystallographica, 1967. **22**: p. 457-464.
49. <http://fable.sourceforge.net/index.php/Grainspotter> (February 8<sup>th</sup>, 2007).